Dual-field-of-view Raman lidar measurements of cloud microphysical properties

Investigation of aerosol-cloud interactions

Der Fakultät für Physik und Geowissenschaften
der Universität Leipzig
eingereichte

Dissertation

zur Erlangung des akademischen Grades

Doctor rerum naturalium
Dr. rer. nat.

vorgelegt

von Diplom–Physiker Jörg Schmidt
geboren am 16. August 1982 in Dresden

Leipzig, 5. Februar 2014

Bibliographische Beschreibung:

Schmidt, Jörg
Dual-field-of-view Raman lidar measurements of cloud microphysical properties: Investigation of aerosol-cloud interactions
Universität Leipzig, Dissertation
135 S., 171 Lit., 53 Abb., 13 Tab.

Referat:
Im Rahmen der vorliegenden Arbeit wurde eine neuartige Lidartechnik in ein leistungsstarkes Lidar-System implementiert. Mit Hilfe des realisierten Aufbaus wurden Aerosol-Wolken-Wechselwirkungen in Flüssigwasserwolken über Leipzig untersucht.

Die angewandte Messmethode beruht auf der Detektion von Licht, das an Wolkentröpfchen mehrfach in Vorwärtsrichtung gestreut und an Stickstoffmolekülen inelastisch zurückgestreut wurde. Dabei werden zwei Gesichtsfelder unterschiedlicher Größe verwendet. Ein Vorwärtsiterations-Algorithmus nutzt die gewonnenen Informationen zur Ermittlung von Profilen wolkenmikrophysikalischer Eigenschaften. Es können der Extinktionskoeffizient, der effektive Tröpfchenradius, der Flüssigwassergehalt sowie die Tröpfchenanzahlkonzentration bestimmt werden. Weiterhin wird die exakte Erfassung der Wolkenunterkantenhöhe durch die eingesetzte Messtechnik ermöglicht. Darüber hinaus ist die Bestimmung von Aerosoleigenschaften mit dem eingesetzten Lidargerät möglich.

Die Qualität des realisierten Messaufbaus wurde geprüft und eine Fehleranalyse durchgeführt. Unter anderem wurde der aus einer Wolkenmessung bestimmte Flüssigwassergehalt mit einem Mikrowellen-Radiometer bestätigt.

Anhand von Fallbeispielen konnte das Potential dieser Messtechnik demonstriert werden. Die Bedeutung von Profilinformationen von Wolkeneigenschaften für die Untersuchung von Aerosol-Wolken-Wechselwirkungen wurde gezeigt. Weiterhin wurde mit Hilfe eines Doppler-Windlidars der Einfluss der Vertikalwindgeschwindigkeit auf Wolkeneigenschaften und damit Aerosol-Wolken-Wechselwirkungen verdeutlicht.

Neunundzwanzig Wolkenmessungen wurden für eine statistische Auswertung bezüglich Aerosol-Wolken-Wechselwirkungen genutzt. Dabei konnte erstmalig die Abhängigkeit von Aerosol-Wolken-Wechselwirkungen von der Wolkeneindringtiefe untersucht werden. Es wurde festgestellt, dass diese auf die untersten 70 m von Wolken beschränkt sind. Weiterhin wurden deutlich stärkere Aerosol-Wolken-Wechselwirkungen in Wolkengebieten festgestellt, die von Aufwinden dominiert werden.

Für der Quantifizierung der Stärke von Aerosol-Wolken-Wechselwirkungen wurden ACI_{N}-Werte genutzt, welche den Zusammenhang zwischen der Tröpfchenanzahlkonzentration und dem Aerosol-Extinktionskoeffizienten beschreiben. Dabei wurde zwischen der Untersuchung der entsprechenden mikrophysikalischen Prozesse und deren Bedeutung für die Wolkenalbedo und damit dem Strahlungsantrieb der Wolken unterschieden. Für die erstgenannte Zielstellung wurde ein ACI_{N}-Wert von 0.80 ± 0.40 ermittelt, für Letztere 0.13 ± 0.07.

Table of Contents

Chapter 1

Introduction

Global warming is one of the key issues of this century. The increase of the global mean temperature due to human activities is proven [*Hegerl et al.*, 2007]. The resulting consequences pose serious threats to all societies all over the world [*IPCC*, 2007]. The occurrence of floods, either due to heavy precipitation events or the rise of the sea level, is to increase. Floods and droughts will affect agriculture negatively, especially in low latitudes. In some African countries the yields from rain-fed agriculture are projected to shrink to 50% by 2020 [*IPCC*, 2007]. Not only the mentioned threats constitute the high relevance of global warming but especially its inevitable link with fundamental issues of modern societies like the critique of economic growth and global (climate) justice.

A further point which demands a profound understanding of the earth's climate system is summarized under the term 'geoengineering', denoting specific interventions in the climate system to compensate for the increased radiative forcing caused by the anthropogenic emissions of greenhouse gases. As the severe consequences of climate change become more obvious these methods are discussed with increased frequency not only in science [*Partanen et al.*, 2012; *Latham et al.*, 2012; *Storelvmo et al.*, 2013; *Katz*, 2010] but also politics [*Vidal*, 2011]. Employing such methods poses great risks as various side effects and unexpected consequences may result in an earth's climate which is far less suitable for human life as without these measures [*Betz et al.*, 2011]. Thus, a sound understanding of the processes in earth's climate system is inevitable.

One major component in the earth's climate system are aerosols. These particles scatter and absorb incoming solar and outgoing terrestrial radiation and thus influence the radiative budget of the earth [*Forster et al.*, 2007]. This so-called direct aerosol effect is rather straightforward to assess by direct measurements [*Holben et al.*, 2001]. Beyond that, aerosol particles affect the radiative budget of earth through the interaction with clouds. There are manifold aerosol-cloud interactions. Some of them lead to a net cooling effect on global climate, others have a net warming effect [*Twomey*, 1977; *Albrecht*, 1989; *Pincus and Baker*, 1994; *Han et al.*, 2002; *Guo et al.*, 2007; *Ackerman et al.*, 2000, 2004]. One important example for aerosol-cloud interactions is the Twomey effect, where aerosols, acting as cloud condensation nuclei (CCN), increase the cloud droplet number concentration (CDNC), which

leads to a brightening of the cloud and a cooling of earth [*Twomey*, 1974, 1977]. Further aerosol-cloud interactions are introduced in Chapter 2.

Aerosol-cloud interactions in general and the Twomey effect in particular have a high share in the change of radiative forcing from the start of the industrial era (about 1750) to the present [*Forster et al.*, 2007]. Furthermore, besides other aerosol-cloud interactions, the Twomey effect is discussed intensively to be used for geoengineering methods [*Partanen et al.*, 2012; *Latham et al.*, 2012]. This constitutes the high need for a deeper understanding of the Twomey effect. The object of the present work is to contribute significantly to this aim.

This mission is challenging as aerosol-cloud interactions are highly complex. It is demanding to isolate the relevant effects from the multitude of feedbacks and interactions for a profound investigation. The coupling of aerosol-cloud interactions with meteorological conditions and cloud dynamics constitutes a further enormous challenge [*Brenguier et al.*, 2003; *Ackerman et al.*, 2004; *Lu and Seinfeld*, 2005; *Mauger and Norris*, 2007; *Guo et al.*, 2007].

Thus, it is extremely difficult to quantify the magnitude of aerosol-cloud interactions. Regarding the change of the radiative forcing due to human activity, the radiative forcing attributed to the Twomey effect has the largest uncertainty of all relevant effects, considered in the fourth assessment report of the Intergovernmental Panel on Climate Change (IPCC) [*Forster et al.*, 2007]. The published values for the magnitude of the Twomey effect differ by more than one order of magnitude, which results in a high uncertainty of the corresponding radiative forcing [*McComiskey and Feingold*, 2008, 2012].

These overwhelming differences can be partially attributed to the usage of different measurement techniques [*McComiskey and Feingold*, 2008, 2012], each having its own shortcomings for the highly demanding task to quantify the Twomey effect. Airborne in-situ measurements, which provide detailed information about aerosol and cloud properties, are very costly and thus cannot be run on a long-term basis. Long-term studies on a global scale can be performed with satellite observations. These approaches in turn suffer from the problem that aerosol and cloud properties cannot be derived at the same location and thus information of neighboring, coarse analysis pixels have to be correlated. Ground-based measurements allow long-term measurements of cloud and aerosol properties, but are limited to point measurements without global validity. The advantages and problems of the different measurement approaches are explained in more detail in Chapter 2.

These challenges illustrate the need not only for the enhancement of existing measurement techniques, but for the development of new, profound measurement techniques for the investigation of aerosol-cloud interactions in general and the Twomey effect in particular. Thus, a keystone of the present work is the implementation and characterization of the new and unique dual-field-of-view (dual-FOV) Raman lidar technique. This ground-based remote-sensing technique permits the investigation of the Twomey effect with a single-instrument approach and is distinguished through the simultaneous, height-resolved measurement of aerosol and cloud properties and a high accuracy at cloud base.

A further keystone of this work is the application of the dual-FOV Raman lidar technique for the examination of aerosol-cloud interactions. This was done by means of several case studies as well as a statistical approach. The dual-FOV Raman lidar measurements were performed at the Leibniz Institute for Tropospheric Research (TROPOS), which is a facility for excellent aerosol and cloud research. Besides laboratory and modelling studies as well as ground-based and airborne in-situ measurements, the institute runs a supersite for ground-based remote sensing of aerosol and cloud properties. Hence, combined measurements of the dual-FOV Raman lidar with further remote-sensing instruments were facilitated. Thereby, the TROPOS Doppler wind lidar for the measurement of the vertical wind speed is of particular importance because the vertical wind speed is one of the major influences for aerosol-cloud relationships [*Feingold et al.*, 2003; *Kim et al.*, 2008; *McComiskey et al.*, 2009].

After this introduction, Chapter 2 gives an overview about the most important aerosol-cloud interaction processes. Furthermore, several approaches to examine these interactions are explained with regard to their advantages and shortcomings. In Chapter 3 the instruments employed for this research are described. In this work, aerosol properties are derived with Raman lidar measurements. The applied methods are introduced in Chapter 4. The new dual-FOV Raman lidar technique was employed for the first time to derive cloud microphysical properties. Chapter 5 introduces this technique. Its basic principles are explained, the implementation of the technique and the measurement setup are described, and quality checks of the lidar setup and the methods for the analysis of the dual-FOV Raman lidar measurements are presented. A measurement example is given in Chapter 6. Furthermore, this chapter includes a comprehensive error analysis of the implemented dual-FOV Raman lidar technique. The following two chapters present the performed studies of aerosol-cloud interactions. Chapter 7 explains case studies. These studies cover aerosol-cloud interactions related to the Twomey effect, a comparison of the CDNC at cloud base and CCN number concentration below cloud, as well as the influence of the vertical wind speed on cloud microphysical properties. A statistical approach to quantify aerosol-cloud relationships related to the Twomey effect is presented in Chapter 8. The work is completed with Chapter 9, which contains a summary.

Chapter 2

Aerosol-cloud interactions

In the previous chapter, the need for a profound understanding of aerosol-cloud interactions was motivated. As these interactions are a major topic of this work, they are explained in more detail in the first section of this chapter. Afterwards, a survey of state-of-the-art methods for the investigation of aerosol-cloud interactions is given. Here, as well as throughout the entire present work, exclusively pure water clouds are considered with the intention to pursue a clearly defined objective. However, it should be mentioned that ice-containing clouds and the corresponging aerosol-cloud interactions, e.g., heterogenous ice nucleation, are also important for the earth's radiative budget and require further investigation [*Seifert et al.*, 2007; *Fridlind et al.*, 2007; *DeMott et al.*, 2010; *Eidhammer et al.*, 2010; *Kanitz et al.*, 2011; *Field et al.*, 2011].

2.1 Aerosol-cloud interactions: Fundamentals

Besides the direct effect of aerosol on the earth's radiation budget by the scattering and absorption of radiation [*Forster et al.*, 2007], aerosols affect climate through aerosol-cloud interactions. An example for the possible impact of aerosol particles on clouds is illustrated in Fig. 2.1, presenting the effect of the exhaust of large ships on cloud properties. These so-called ship tracks were already investigated by *Radke et al.* [1989]. The most important aerosol-cloud interactions are explained in the following paragraphs.

Indirect aerosol effects describe modifications of cloud microphysical and radiative properties through the interaction with aerosol particles which are carried into clouds with updrafts [*Forster et al.*, 2007; *Heintzenberg and Charlson*, 2009]. These modifications are achieved through the fraction of aerosol particles that act as CCN and thus increase CDNC. One important example for indirect aerosol effects is the Twomey effect, also named first aerosol indirect effect or cloud albedo effect, which is depicted in Fig. 2.2 [*Twomey*, 1974, 1977]. This effect describes the increase of CDNC at a constant liquid-water content (LWC), which leads to smaller cloud droplets. This implies a higher cloud albedo, generating a net cooling effect on earth.

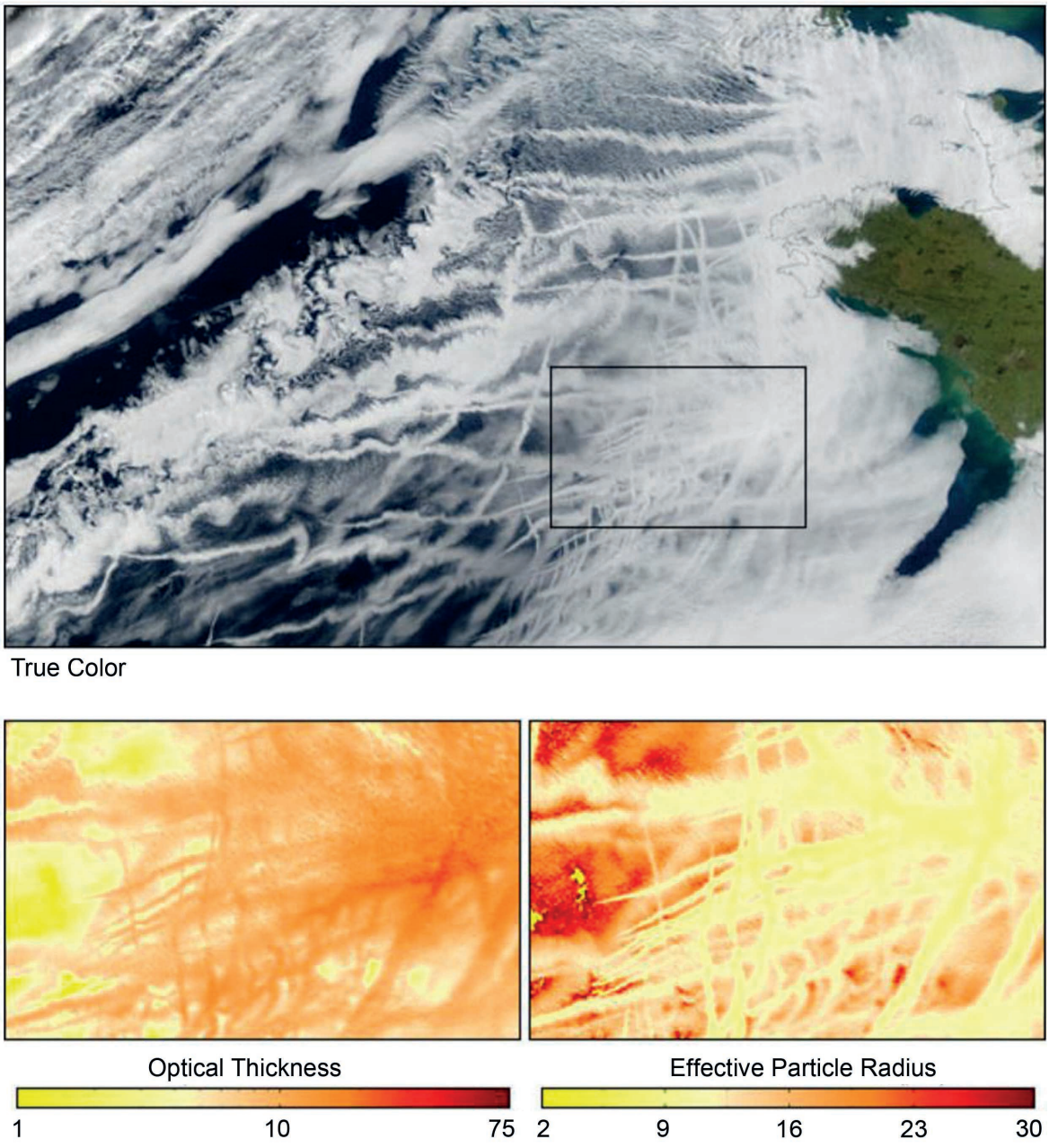

Figure 2.1: Ship tracks recorded with the Moderate Resolution Imaging Spectroradiometer (MODIS) on the Aqua satellite west of Spain and France on 27 January 2003. Top: the aerosol particles from the exhausts along ship routes act as CCN and thus increase cloud albedo. Bottom: the aerosols do affect the cloud radiative (optical thickness) and microphysical (effective droplet radius) properties. The images are a courtesy of NASA's Earth Observatory.

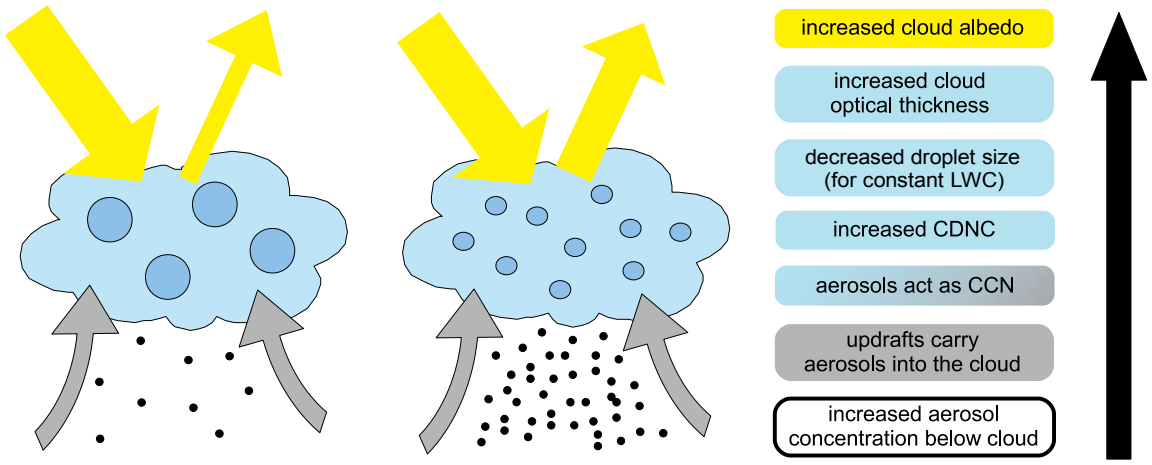

Figure 2.2: Illustration of the Twomey effect. An increased aerosol load is carried with updrafts into the cloud. The increase of CCN leads to an increased CDNC, decreased cloud droplet size, and thus to an increased optical thickness, which results in an increase of the cloud albedo.

The magnitude of the involved aerosol-cloud interactions, i.e., the magnitude of the change of cloud droplet size and CDNC for a given change of the aerosol load, depends on several factors. First of all, the speed of the updraft, carrying the aerosol particles into the cloud, is very important because it determines the fraction of aerosol particles getting activated and becoming cloud droplets [*Leaitch et al.*, 1996; *Feingold et al.*, 2003; *McComiskey et al.*, 2009]. Stronger updrafts lead to higher supersaturations at cloud base and thus to a higher fraction of activated aerosol particles. Another determining factor of the activation process and thus the Twomey effect is the aerosol size distribution [*Dusek et al.*, 2006]. In general, for a given updraft velocity, aerosol particles exceeding a certain size become activated. A minor factor for the efficiency of the aerosol particles to act as CCN is the chemical composition [*Ervens et al.*, 2005].

A further indirect aerosol effect was described by *Albrecht* [1989]. The Albrecht effect, also named second indirect aerosol effect or cloud lifetime effect, is predicted especially for marine clouds. It describes the reduction of drizzle through the decrease of cloud droplet size due to a higher CCN load. As drizzle is an important process for the regulation of LWC of marine clouds, the suppression of drizzle may increase the LWC. Thereby, the cloud lifetime is increased which leads to a higher fractional cloudiness and thus to an increase of the global albedo, which has a cooling effect on earth. Furthermore, the reduction of drizzle may increase cloud thickness, leading to an even higher cloud albedo [*Pincus and Baker*, 1994].

The second aerosol indirect effect may also lead to a decrease of LWC at a higher aerosol particle number concentration (APNC) and thus to an increased global warming. *Han et al.* [2002] investigated the dependence of LWC on CDNC. One third of the investigated clouds showed an LWC increase for higher CDNC as constituted above. However, another third of

the observations showed a decreasing LWC for increasing CDNC. This behavior was investigated and reproduced by model simulations [*Stevens et al.*, 1998; *Ackerman et al.*, 2004; *Lu and Seinfeld*, 2005; *Xue and Feingold*, 2006; *Guo et al.*, 2007]. Depending on cloud type, meteorological conditions, cloud dynamics and feedback mechanisms, evaporation of liquid water due to the smaller droplet size becomes a primary effect. The evaporation may induce further feedbacks regarding cloud dynamics, which amplify this effect [*Stevens et al.*, 1998; *Han et al.*, 2002; *Ackerman et al.*, 2004; *Lu and Seinfeld*, 2005; *Xue and Feingold*, 2006; *Guo et al.*, 2007].

Liu and Daum [2002] described an indirect aerosol effect that diminishes the magnitude of the Twomey effect and thus leads to a warming effect on earth. Field studies of marine clouds showed an increase of the relative dispersion of the cloud droplet size distribution in polluted air masses (see *Liu and Daum* [2002] and references therein). This increase leads to a larger effective cloud droplet radius for a constant LWC and CDNC, which is in contrast to the dependence of the effective cloud droplet radius in the Twomey effect.

Aerosol particles affect cloud properties not only by acting as CCN but also through the absorption of solar radiation. *Ackerman et al.* [2000] investigated the effect of absorbing aerosol particles (e.g., soot) on tropical, marine stratocumuli. The heating due to the absorption of solar radiation leads to a reduction of relative humidity and a stabilization of the boundary layer. Both effects reduce the cloud cover and thus decrease the global albedo, which has a net warming effect on global climate.

2.2 Aerosol-cloud interactions: Investigation

There are a number of measurement approaches to investigate aerosol-cloud interactions in general and the interactions related to the Twomey effect in particular. To facilitate the understanding of the basic ideas of these approaches, Subsection 2.2.1 clarifies the major obstacles for these investigations. The measurement approaches are so manifold that they differ even in their principal objective, which is explained in Subsection 2.2.2. A common way to quantify the magnitude of aerosol-cloud interactions is introduced in Subsection 2.2.3. This quantification is applied to the Twomey effect in Subsection 2.2.4. Afterwards, several state-of-the-art measurement approaches to assess this effect are briefly introduced and evaluated.

2.2.1 Challenges for investigations of aerosol-cloud interactions

For the identification and quantification of single aerosol-cloud interactions the joint and entangled occurrence of aerosol-cloud interactions is a major obstacle. An example is given in the following. For satellite-based investigations of the Twomey effect the cloud albedo is measured from above the cloud. Furthermore, it is necessary to derive the cloud's liquid-water path (LWP). Only with this information it is possible to distinguish between albedo changes that are due to the Twomey effect and those that are induced by LWP changes, which may be caused by other aerosol-cloud interactions as well (cf. Section 2.1).

Cloud processes are manifold and complex. Thus, cloud properties are not merely influenced by aerosol-cloud interactions but from a number of further cloud processes as well, which complicates the identification and quantification of aerosol-cloud relationships. For instance coagulation affects cloud droplet size. As this cloud microphysical property is an important quantity for observations of aerosol-cloud interactions, these interactions become more disguised. The significance of coagulation increases during the lifetime of the corresponding air parcel. Hence, coagulation becomes more important with increasing cloud penetration depth, because droplets are formed at the cloud base during updraft periods when new aerosol particles are transported into the cloud, become activated, and are subsequently transported upwards. Furthermore, turbulence amplifies coagulation.

This leads to another major challenge for investigations of aerosol-cloud interactions, which is the large influence of dynamics on cloud microphysical properties. Entrainment and the subsequent deviations from an adiabatic LWC profile reduce the cloud's optical thickness as well as droplet size. Furthermore, various mixing processes may take place in clouds. For example, cloud parcels containing larger droplets may be mixed into the lower cloud part via downdrafts.

In addition, the vertical wind speed has an effect on aerosol-cloud interactions itself [*Feingold et al.*, 2003; *Kim et al.*, 2008; *McComiskey et al.*, 2009]. Hence, a profound understanding of the aerosol-cloud interactions underlying the various aerosol indirect effects requires knowledge about the vertical wind speed. In case of the Twomey effect the updraft velocity determines the supersaturation at cloud base and thus the fraction of activated aerosol particles and thereby the magnitude of the resulting effect. The LWP response to an increased aerosol load depends on the vertical air motion as well [*Stevens et al.*, 1998; *Han et al.*, 2002; *Ackerman et al.*, 2004; *Lu and Seinfeld*, 2005; *Xue and Feingold*, 2006; *Guo et al.*, 2007].

As aerosol-cloud interactions may affect the cloud dynamics in turn [*Stevens et al.*, 1998; *Han et al.*, 2002; *Ackerman et al.*, 2004; *Lu and Seinfeld*, 2005; *Xue and Feingold*, 2006; *Guo et al.*, 2007], the involved processes become even more entangled, which further complicates the situation. An example is the effect of drizzle on dynamics. As mentioned in Section 2.1, an increased aerosol load may reduce drizzle [*Albrecht*, 1989]. The resulting decreased evaporation below cloud base leads to a net warming effect, which enhances vertical mixing [*Albrecht*, 1989; *Stevens et al.*, 1998; *Lu and Seinfeld*, 2005].

2.2.2 Objectives of investigations of aerosol-cloud interactions

In the Subsections 2.2.5 to 2.2.7 measurement approaches to examine the Twomey effect and the related aerosol-cloud interactions are introduced. These approaches differ strongly in spatial and temporal resolution as well as in the observed quantities. Due to the different contents of information, the principal objectives of investigations differ. To keep track of a clear scientific question, it is reasonable to distinguish the objectives of the various approaches as described in the following.

A) Focus on microphysical processes of aerosol-cloud interactions

One major objective regarding the understanding of aerosol-cloud interactions is the investigation of the microphysical processes involved in these interactions [*Twohy et al.*, 2005; *Lu et al.*, 2007, 2008; *Painemal and Zuidema*, 2013]. This objective demands the knowledge of the direct response of cloud microphysical properties such as cloud droplet effective radius and CDNC to changes in CCN number concentration without interference from other cloud processes. On the one hand, the motivation for research related this objective constitutes its significance for the Twomey effect. On the other hand, this objective is meaningful due to its potential for geoengineering techniques.

This objective requires measurements with a very high spatial resolution. Besides aerosol load and cloud properties, further important observables are the vertical wind velocity and the aerosol size distribution. If these measurement requirements can be met with a high temporal resolution, the detailed analyses should be confined to updraft periods because aerosol-cloud interactions occur when aerosol particles are mixed into the cloud, become activated, and induce aerosol-cloud interactions. Furthermore, the investigations should be confined to the cloud base, where the aerosol is mixed in and leads to aerosol-cloud interactions. Aerosol-cloud correlations observed in greater cloud penetration depths originate mainly from the upward transport of cloud parcels which were affected by aerosol-cloud interactions at the cloud base. During the transport the cloud parcels are exposed to a number of other cloud processes which diminish the influence of aerosol particles on cloud properties.

For a successful pursuit of this objective the choice of the observed clouds is of importance as well. It is convenient to probe thin, layered clouds, because their properties are less influenced by cloud dynamics and thus allow the examination of the aerosol influence on cloud microphysical properties with relatively small secondary effects. On the contrary, for convective clouds, which exhibit much stronger vertical air motions, influences of up- and downdrafts as well as various triggered cloud processes play a much larger role regarding the effect on cloud microphysical properties.

B) Focus on Twomey effect and its radiative effects

Another major objective is the assessment of the Twomey effect itself, i.e., the change of cloud albedo as a response to an altered aerosol load below the cloud, and the resulting radiative forcing [*Lebsock et al.*, 2008; *Quaas et al.*, 2008; *Bellouin et al.*, 2013]. Hence, the effect of the aerosol intake on cloud properties, integrated over the complete cloud vertical extent, as observed from above the cloud is of interest. This knowledge is important for the evaluation of the role of the Twomey effect in the earth's radiative budget as well as the significance of the anthropogenic share in the Twomey effect for climate change.

For this aim, a global, long-term dataset is extraordinarily important to account for regional, seasonal, and interannual variations of the various aerosol-cloud interactions [*Lohmann et al.*, 2007]. The measurement resolution loses its significance, because global climate models work with horizontal resolutions of $200 \times 200\,\mathrm{km}^2$ and timesteps of about

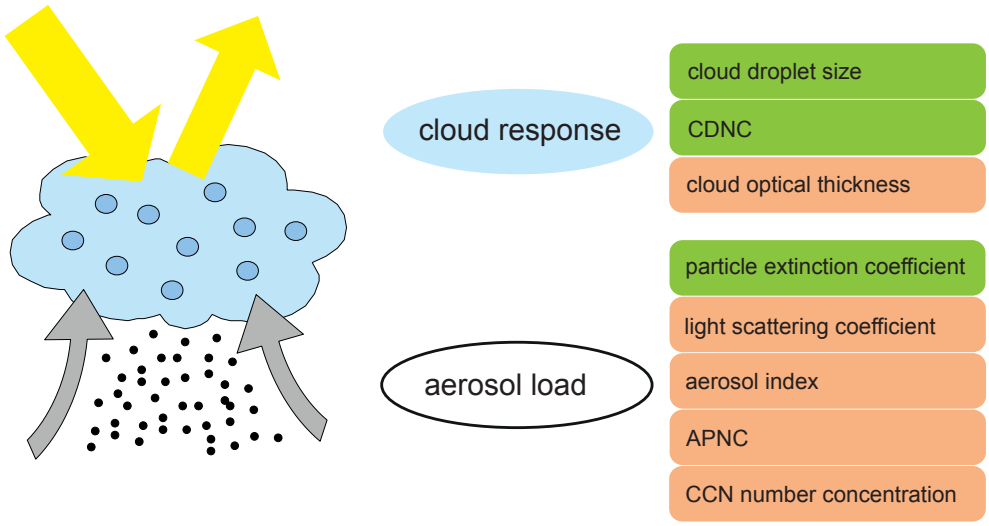

Figure 2.3: Possible observables for the examination of aerosol-cloud interactions related to the Twomey effect. Observables used in the *ACI* approach of *McComiskey et al.* [2009] (cf. Eq. (2.2) and (2.3)) are highlighted in green in contrast to the other observables shown in reddish color.

20 minutes [*Lohmann et al.*, 2007]. Processes that act on smaller spatial scales or shorter temporal scales have to be parameterized. For investigations targeting at this objective a detailed microphysical understanding and the isolation of the Twomey effect from other mechanisms is not important as the sole correlation of aerosol load with cloud properties and thus radiative effects will be of major significance for climate models. The distinction between the Twomey effect and other mechanims which also influence the radiative budget loses its relevance.

2.2.3 Quantification of aerosol-cloud interactions

For the investigation of aerosol-cloud interactions proxies have to be used to describe aerosol as well as cloud properties. Fig. 2.3 illustrates a number of possible observables. The aerosol load below the cloud can be characterized with the aerosol extinction coefficient [*Feingold et al.*, 2003], its height-integrated value, the aerosol optical depth [*Kaufman and Fraser*, 1997], the light scattering coefficient [*Kim et al.*, 2008], the aerosol index [*McComiskey et al.*, 2009], the APNC [*Lu et al.*, 2007, 2008; *Painemal and Zuidema*, 2013], and the CCN number concentration [*McComiskey et al.*, 2009]. The aerosol index is the product of the aerosol optical thickness and the Ångström exponent, which is explained in Subsection 4.2.4. Compared to the optical thickness as a proxy for the aerosol load, smaller particles, which can still act as CCN, have a stronger influence on this quantity.

The response of the cloud to the aerosol properties can be investigated in regard to the cloud optical thickness, cloud droplet size, or CDNC. Regarding droplet size, a quantity representing a meaningful average has to be found as the numerous droplets in a cloud

volume are of different size. For research related to the Twomey effect the utilization of the effective radius

$$r_{\mathrm{e}} = \frac{\langle r^3 \rangle}{\langle r^2 \rangle} = \frac{\int r^3 n(r) \mathrm{d}r}{\int r^2 n(r) \mathrm{d}r} \tag{2.1}$$

is common, because it constitutes the surface-area-weighted mean radius, and the particle surface is relevant for the scattering cross section and thus radiative effects. In Eq. (2.1) r is the radius of the corresponding droplet and $n(r)$ describes the droplet spectrum with respect to r in the considered cloud volume.

For investigations of aerosol-cloud interactions related to the Twomey effect, only aerosol and cloud properties derived at a constant LWC should be correlated (cf. Section 2.1). For example, the cloud droplet effective radius is not only affected by aerosol-cloud interactions but by changes of the LWC as well. An exception to this requirement are analyses where the CDNC is employed as the proxy for the cloud response to a change of the aerosol load below the cloud, because there is no direct microphysical link between the LWC and the CDNC. Hence, derived datasets for investigations of aerosol-cloud relationships do not have to be split into subdatasets according to the LWC and thus are more comprehensive. Furthermore, biases of derived aerosol-cloud relationships, due to the finite LWC ranges, are avoided.

For a quantitative description of aerosol-cloud interactions on the basis of observations of the aerosol particle extinction coefficient as well as cloud droplet effective radius and CDNC *McComiskey et al.* [2009] introduced the ACI parameters

$$ACI_{\mathrm{r}} = -\frac{\mathrm{d} \ln r_{\mathrm{e}}}{\mathrm{d} \ln \alpha} \tag{2.2}$$

and

$$ACI_{\mathrm{N}} = \frac{\mathrm{d} \ln N}{\mathrm{d} \ln \alpha}, \tag{2.3}$$

respectively, on the basis of the work of *Feingold et al.* [2001]. The aerosol particle extinction coefficient is denoted as α and N stands for the CDNC. The observables used for this approach to investigate aerosol-cloud interactions related to the Twomey effect are shown in green color in Fig. 2.3 in contrast to the other observables displayed in reddish color.

The authors named the parameter ACI (derived from aerosol-cloud interactions) to indicate that the observed variables describe microphysical responses rather than radiative forcings, which might be deduced from a nomenclature on the basis of the Twomey effect. The calculation of the derivatives of the logarithms of the considered quantities was proposed by *Feingold et al.* [2001]. Thus, the relative changes of the observed aerosol and cloud properties, i.e.,

$$ACI_{\mathrm{r}} = -\frac{\mathrm{d} \ln r_{\mathrm{e}}}{\mathrm{d} \ln \alpha} = -\frac{\alpha}{r_{\mathrm{e}}} \frac{\Delta r_{\mathrm{e}}}{\Delta \alpha} \tag{2.4}$$

and

$$ACI_{\mathrm{N}} = -\frac{\mathrm{d} \ln N}{\mathrm{d} \ln \alpha} = -\frac{\alpha}{N} \frac{\Delta N}{\Delta \alpha}, \tag{2.5}$$

are considered which makes the ACI values less susceptible to measurement errors.

As ACI_{r} and ACI_{N} are two parameters describing the identical physical effect, there has to be a relationship between these parameters which is the following:

$$ACI_{\mathrm{r}} = -\frac{1}{3} ACI_{\mathrm{N}} \tag{2.6}$$

[*Feingold et al.*, 2001; *McComiskey et al.*, 2009]. The ACI values are within the boundaries

$$0 < ACI_{\mathrm{r}} < 0.33 \tag{2.7}$$

and

$$0 < ACI_{\mathrm{N}} < 1 \tag{2.8}$$

and reach the maximum values of 0.33 and 1, respectively, when all aerosol particles transported into the cloud are activated to cloud droplets [*Feingold et al.*, 2001; *McComiskey et al.*, 2009].

The introduced ACI values constitute convenient measures for a quantitative description of aerosol-cloud interactions and thus for a quantitative pursuit of objective A. However, the ACI approach can be applied to any other set of observables describing aerosol and cloud properties, e.g., the observables shown in Fig. 2.3. Regardless of the choice of the aerosol and cloud proxies, the ACI approach excels in its simplicity. Nevertheless, it has to be stated that it is a strong simplification of the processes involved in the Twomey effect, because updraft velocity as well as aerosol size distribution are not considered.

2.2.4 Calculation of magnitude of the Twomey effect from ACI values

In the previous subsection the concept of ACI values was introduced for a quantitative pursuit of objective A. This subsection introduces a measure for a quantitative assessment of objective B, the investigation of the Twomey effect. This measure is the quantity CAE, which is named after the cloud albedo effect, i.e., the Twomey effect, and defined as [*Painemal and Zuidema*, 2013]

$$CAE = \frac{\mathrm{d}A}{\mathrm{d}\alpha/\alpha} = \frac{\mathrm{d}A}{\mathrm{d}\ln\alpha} \tag{2.9}$$

with the cloud albedo A. It describes the change of the cloud albedo for a relative change of the aerosol extinction coefficient below the cloud, which represents the aerosol load.

The Twomey effect can be considered to consist of two processes. The first process describes the relative change of CDNC with a relative change in aerosol load and is quantified with ACI_{N}.

The second process describes the change of cloud albedo with a relative change of CDNC. This process can be quantified with the relative cloud susceptibility S_{R}, which is defined as [*Platnick and Oreopoulos*, 2008]

$$S_{\mathrm{R}} = \frac{\mathrm{d}A}{\mathrm{d}N/N} = \frac{\mathrm{d}A}{\mathrm{d}\ln N}. \tag{2.10}$$

Oreopoulos and Platnick [2008] derived the gobal distribution of the relative cloud susceptibility from analyses of MODIS data. As the analyses were performed for four months

(January, April, July, and October) the averages of the relative cloud susceptibilities can be regarded as an estimate for the annual mean values. In-situ measurements confirmed the retrieved susceptibilities for the region of the southeast Pacific Ocean [*Painemal and Zuidema*, 2013]. For the region of central Germany an annual mean relative cloud susceptibility of about 0.049 ± 0.008 was obtained. However, in the analyses of *Oreopoulos and Platnick* [2008] a LWC of $0.3\,\mathrm{g/m^2}$ is assumed. To account for clouds with different mean LWC, a scaling factor of $0.3/w_\mathrm{c}$, with the mean LWC w_c, has to be applied to the relative cloud susceptibilities [*Oreopoulos and Platnick*, 2008].

Thus, *CAE* is obtained as

$$CAE = \frac{\mathrm{d}A}{\mathrm{d}\ln\alpha} = \frac{\mathrm{d}A}{\mathrm{d}\ln N}\frac{\mathrm{d}\ln N}{\mathrm{d}\ln\alpha} = S_\mathrm{R} A C I_\mathrm{N}. \tag{2.11}$$

This aproach is used in this work to assess the magnitude of the Twomey effect.

Alternatively, *CAE* can be obtained from the direct correlation of the cloud albedo with the aerosol load below the cloud. For this approach the cloud albedo can be estimated from the cloud optical thickness τ_c with the approximation [*Lacis and Hansen*, 1974]

$$A \approx \frac{0.13\tau_\mathrm{c}}{1 + 0.13\tau_\mathrm{c}}. \tag{2.12}$$

Alternative approximations of the cloud optical thickness were given by *Schwartz et al.* [2002] and *Platnick and Twomey* [1994].

2.2.5 Airborne in-situ measurements

Airborne in-situ measurements are applied for investigations of aerosol-cloud interactions because of their capability of performing detailed measurements of aerosol as well as cloud microphysical properties with high resolution. An example is the study of *Lu et al.* [2008]. In this study, not only the aerosol number concentration in several size ranges and the CDNC were measured but also the CCN concentration at several supersaturations, the aerosol and cloud droplet size distribution, and the chemical composition of the aerosol particles. Further measurements performed in the framework of the cited publication covered the meteorological situation, assessing the temperature, dew point, relative humidity, pressure, and the wind direction and speed and thus the updraft velocity as well. Besides information on further cloud properties as the LWC, information about the up- and downwelling radiative fluxes above and below a cloud were obtained.

Only airborne in-situ measurements are capable of providing such a multitude of aerosol and cloud properties. Thus, this measurement approach delivers very detailed pictures of aerosol-cloud interactions, giving access to all important determining factors and thereby highlighting several aspects of the investigated processes. These advantages make airborne in-situ measurements a valuable approach for the investigation of objective A, the detailed understanding of microphysical processes of aerosol-cloud interactions.

The capability of pursuing this objective is enhanced through the performance of non-aggregated measurements as the basic object of measurement is the particle. Thus, cloud and aerosol properties can be observed at the scale of the cloud droplet formation process.

The price for these advantages are the high effort and costs of these measurements. Thus, these studies are always restricted to a limited number of case studies and unable to deliver neither a global nor a long-time picture. Even the statistical relevance of those studies may be questioned. *Lu et al.* [2008] used the data from only 22 cloud measurement flights for their approach to determine an ACI value. Hence, this approach is not suitable for the pursuit of objective B.

Another crucial disadvantage of airborne in-situ measurements is that the measurement platform moves with a relatively high horizontal velocity. Even with the usage of helicopters [*Siebert et al.*, 2006], which are capable of moving much slower than the conventionally employed airplanes, the high horizontal velocity does not allow the derivation of vertical profiles of the measured quantities. This drawback might hamper a broader understanding of the investigated processes. A further consequence from the missing profiling capability is that aerosol and cloud properties cannot be measured simultaneously. The inability to assess the temporal development of the observed cloud formation processes is another major disadvantage, which results from the high horizontal speed of the measurement platform.

2.2.6 Satellite observations

Satellite measurements deliver global, long-term datasets. Thus, these measurements suit ideally for the assessment of the Twomey effect and its radiative effect, denoted as objective B in Subsection 2.2.2. A further advantage of satellite measurements in this field is that satellites detect the light that was scattered in clouds from above the cloud, i.e., from the same perspective as relevant for the retrieval of the cloud albedo. On the other hand, the low horizontal resolution of the sensors obscures processes occurring on smaller spatial scales and thus makes this approach not suitable for research related to objective A [*McComiskey and Feingold*, 2008]. Furthermore, the missing height resolution of the retrieved cloud microphysical properties and thus the inability to retrieve cloud properties at cloud base inhibits insights linked to objective A. The lack of wind measurements is a further point which inhibits research related to this field.

Typically, passive remote sensors are used as in the approach by *Quaas et al.* [2008], which is explained in the following as a common example for these approaches. Further, similar studies are listed in Table 2.1 in Subsection 2.2.8. *Quaas et al.* [2008] used the broadband short-wave planetary albedo, obtained from the Clouds and the Earth's Radiant Energy System (CERES) and cloud properties as well as aerosol optical depth retrieved by the MODerate Resolution Imaging Spectroradiometer (MODIS). Both instruments are onboard NASA's satellite Terra. The aerosol optical depth is obtained with a resolution of $1^\circ \times 1^\circ$, which corresponds to about $100 \times 100\,\mathrm{km}^2$. The retrieved cloud properties (cloud cover, cloud phase, LWP, cloud optical depth, cloud droplet effective radius) have a higher resolution of about $20 \times 20\,\mathrm{km}^2$. The cloud optical depth and droplet effective radius were used to calculate the CDNC. Aerosol and cloud properties of neighboring analysis pixels were correlated to calculate the dependence of cloud fraction, LWP, and CDNC on aerosol optical depth. The corresponding ACI_r values were calculated for 14 regions and four seasons. The

lowest values of −0.015 to +0.03 were derived over Australia and the islands of Oceania, South America, North America, and Africa. The highest values ranged from 0.08 to 0.15 and were obtained over the North Pacific, North Atlantic, and Tropical Atlantic Ocean. Thus, a quantitative analysis of the Twomey effect was performed and, additionally, a clear difference of the Twomey effect over land and ocean was shown.

Although this approach seems to suit ideally to deal with objective B, the investigation of the Twomey effect, there are a number of drawbacks. One major point is the usage of passive instruments, which implies that the corresponding measurements are not height-resolved. Hence, aerosol and cloud properties cannot be derived in the same gridpoint of observation. Therefore, aerosol and cloud properties derived in neighboring grid points are correlated, which is a possible source of error. A further reason for a possible decoupling of aerosol and cloud properties is the missing information on the heights of the aerosol and cloud layers. For large height differences decoupling is expected.

Both problems might be overcome with further advances of the measurement approach. For example, combinations of weather or transport model simulations with satellite observations are used. In this approach, aerosol properties are retrieved in cloudy regions from model simulations which assimilate aerosol properties obtained from satellite observations in cloud-free regions [*Bréon et al.*, 2002; *Chameides et al.*, 2002; *Bellouin et al.*, 2013]. The height of the observed aerosol and cloud layers can be obtained from satellite-based active remote-sensing instruments. *Costantino and Bréon* [2013] analyzed combined MODIS and Cloud-Aerosol Lidar and Infrared Pathfinder Satellite Observations (CALIPSO) data with high horizontal resolutions ranging from 1×1 to $10 \times 10\,\mathrm{km}^2$. The authors used the lidar measurements to check if aerosol and cloud layers were located in heights which allow them to interact. Only cases in which an interaction was possible were used to investigate the Twomey effect. The authors showed that the aerosol load has a considerable effect on the cloud properties when appearing in the corresponding height, but cloud droplet size does not show any evident change with change of the aerosol load for aerosol layers located well above cloud layers.

Despite of these advances there remain a number of problems which hamper studies of aerosol-cloud interactions using satellite observations. The distinction between cloudy and cloud-free regions may be ambigiuos which handicaps the distinction between aerosol and cloud properties. This problem is especially severe for thin clouds with a low optical thickness. Furthermore, the properties of those clouds cannot be properly analyzed with passive satellite measurements. Hence, these clouds are not considered in several satellite studies (e.g., *Quaas et al.* [2008]), which may imply a bias of these studies. Moreover, multilayered clouds are excluded from those analyses (e.g., *Quaas et al.* [2008]). The retrievals employed for the evaluation of the measured data have their limitations as well. Bright surfaces (e.g., desert, snow, or ice-covered surfaces) as well as high latitudes constitute problems for the aerosol retrievals and thus are excluded in the corresponding studies (e.g., *Quaas et al.* [2008]). Furthermore, the assumptions made for the retrieval are not always explicitly stated and may lead to oversimplifications of the investigated problems. Additionally, in most stud-

ies the horizontal resolution is too low to investigate small clouds, which are most susceptible to aerosol-cloud interactions [*Kaufman et al.*, 2005].

2.2.7 Ground-based remote sensing

Several ground-based remote-sensing techniques exist for the measurement of aerosol and cloud properties. Multiwavelength Raman lidars can be employed to derive various aerosol properties, as explained in detail in Chapter 4. The aerosol load can be quantified with the aerosol particle extinction coefficient. Furthermore, inversion techniques can be applied to retrieve aerosol microphysical properties, e.g., number concentration and complex refractive index. Cloud properties can be determined with cloud radar and microwave radiometer (MWR) probings (cf. Sections 3.3 and 3.4). These measurements deliver information about the CDNC, droplet size, LWC, and LWP. Further examples for ground-based remote-sensing techniques for the retrieval of cloud properties are given below. The dual-FOV Raman lidar technique, which was employed for this work and is explained in Chapter 5, constitutes another active remote-sensing technique for the measurement of cloud microphysical properties. Hence, a number of aerosol and cloud properties can be retrieved with ground-based remote-sensing techniques, which permits investgations of aerosol-cloud interactions.

A first investigation of aerosol-cloud interactions with active ground-based remote measurements, which did not rely on additional ground-based in-situ measurements, was carried out by *Feingold et al.* [2003]. The authors used Raman lidar measurements to derive the aerosol particle extinction below clouds as a measure for the aerosol load. Cloud properties were obtained from Doppler radar and MWR measurements, employing the retrieval algorithm of *Frisch et al.* [2002]. Thus, under the assumption of a height-constant CDNC, the CDNC and the profile of the effective radius were determined. Furthermore, the LWP, obtained from the MWR, was used to group the measurements for avoiding effects of the LWP on the effective radius. With the knowledge of the vertical wind velocity, measured with the Doppler radar, the analysis was restricted to updraft regions with updrafts stronger than 0.1 m/s. Hence, the study focuses on activation events to avoid influences from other cloud processes on the measured quantities. In this study ACI_{r} values from 0.02 to 0.16 were derived. Airmasses with marine origin yielded higher ACI_{r} values than those with continental origin. An average ACI_{r} value of 0.1 was obtained.

Other studies about aerosol-cloud interactions use ground-based in-situ measurements to quantify the aerosol load below the cloud [*Garrett et al.*, 2004; *Kim et al.*, 2008; *McComiskey et al.*, 2009]. Thus, these studies are capable of retrieving a number of aerosol properties in detail but are restricted to the investigation of comparably low clouds within a well-mixed boundary layer to assure that the aerosol properties on ground are representative for the aerosol load directly below cloud base.

The studies of *Garrett et al.* [2004], *Kim et al.* [2008], and *McComiskey et al.* [2009] show the multitude of possibilities for the retrieval of cloud microphysical properties. *Garrett et al.* [2004] use measurements of radiative fluxes in combination with a radiative-transfer model, supported by MWR measurements to obtain the LWP and radar measurements to detect the

cloud boundaries. Thus, they derive the cloud droplet effective radius, optical thickness, and LWP. For the derivation of these properties *Kim et al.* [2008] employ an inversion method using data from a multi-filter rotating shadowband radiometer and MWR, supported by radar measurements to detect the cloud boundaries. *McComiskey et al.* [2009] derive the cloud droplet effective radius, optical thickness, and LWP from combined measurements of a two-channel narrow-field-of-view radiometer and an MWR.

Compared to airborne and spaceborne measurements ground-based measurements are comparatively simple and low-priced, which makes long-term studies affordable. This point is important for the pursuit of objective B. The restriction of these measurements to one location seems to prevent significant contributions to this objective. However, this hindrance can be overcome with the setup of measurement networks, which is a common strategy to derive results with validity for a larger region, a continent or even the global scale. Examples are the worldwide measurement network of sunphotometers AERONET (Aerosol Robotic Network) [*Holben et al.*, 1998], the European network of cloud radar measurements CLOUDNET [*Illingworth et al.*, 2007], and a number of lidar networks such as the European Aerosol Research Lidar Network (EARLINET) [*Bösenberg et al.*, 2003; *Wandinger et al.*, 2004; *Pappalardo et al.*, 2009], the Micro Pulse Lidar Network (MPLNET) [*Welton et al.*, 2001], the Asian Dust Network (ADNet) [*Murayama et al.*, 2001], and the Latin-American Lidar Network (LALINET) [*Antuna et al.*, 2012]. However, it has to be mentioned that the setup of measurement networks with complex measurement systems requires a large effort regarding the homogenization of the measuring instruments and data analysis methods as well as the quality assurance of every single instrument which is part of the network [*Matthais et al.*, 2004; *Böckmann et al.*, 2004; *Pappalardo et al.*, 2004; *Freudenthaler*, 2008].

Regarding the pursuit of objective B, the utilization of ground-based remote-sensing techniques also bears several advantages compared to the alternatively utilized satellite observations. The height-resolved aerosol and cloud measurements, possible with active remote-sensing instruments, permit that solely properties of aerosol and cloud layers are correlated that are derived in similar altitudes and thus are supposed to be coupled. Furthermore, ground-based remote-sensing techniques permit the derivation of more observables than satellite techniques, e.g., the vertical wind speed and aerosol number concentration, and thus lead to more meaningful measurements. The retrievals of aerosol and cloud properties with active ground-based remote-sensing techniques are simpler and require less assumptions than the corresponding satellite retrievals. An example is the aerosol particle extinction coefficient which is obtained with Raman lidar measurements without any assumptions. In contrast, the satellite retrievals for the derivation of the aerosol optical thickness are complex and need additional information such as the albedo of the corresponding earth's surface.

Ground-based remote-sensing techniques are also capable of investigating issues related to objective A because the temporal and spatial resolutions of most remote-sensing techniques are adequate for this ambition [*McComiskey and Feingold*, 2012]. Airborne in-situ instruments provide more detailed measurements than ground-based techniques in regard to the number of derived aerosol and cloud properties. However, the key parameters as cloud

droplet size and number concentration, cloud LWC, aerosol extinction coefficient, aerosol type, and updraft velocity can be assessed with ground-based remote-sensing measurements.

Ground-based active remote-sensing techniques also have several advantages over airborne in-situ measurements regarding the investigation of aerosol-cloud correlations. First of all, the profile information of the derived quantities is of importance. With active ground-based techniques, cloud properties can be observed directly at cloud base where the aerosol particles are mixed into the cloud. The derivation of cloud mean values or the utilization of cloud properties in an arbitrary cloud penetration depth, which is done in several studies employing airborne in-situ measurements, cannot lead to results of equal quality. Furthermore, the profiling information is important to assess the dependence of aerosol-cloud interactions on cloud penetration depth. This information constitutes the link between the microphysical processes of aerosol-cloud interactions and the resulting albedo change and thus radiative effect. A conjunction of the insights related to objective A and B is established through this link.

Furthermore, the temporal evolution of a cloud can be investigated through stationary measurements. Information about the lifecycle of a cloud from its formation to its dissolution are relevant for the understanding of a number of cloud processes, including aerosol-cloud interactions: at the beginning of the cloud's lifecycle its properties might be stronger influenced by the activation of aerosol particles than towards the end of its lifespan when entrainment gains significance, leading to the dissolution of the cloud.

Summarizing, one may assert that ground-based active remote-sensing techniques are at least equally adequate for the pursuit of objectives A and B as airborne in-situ and satellite approaches, respectively. Ground-based techniques even exhibit some advantages. However, the major advantage of ground-based measurement techniques is the capability of performing investigations for both objectives. Hence, results from research related to both objectives can be combined and justified. Thus, it can be studied to what extent aerosol-cloud interactions, which are initialized at cloud base, influence cloud properties in larger penetration depths as well and what is the resulting overall albedo effect. Likewise, it can be studied which magnitude of aerosol-cloud interactions is required for an obtained albedo change associated with a certain radiative forcing and if aerosol-cloud interactions of this magnitude occur globally often enough to be relevant for the earth's radiative budget.

2.2.8 Summary of ACI values from other studies

Results of ACI values from several investigations of aerosol-cloud relationships are given in Table 2.1, sorted according to the approaches introduced in the Subsections 2.2.5 to 2.2.7. For these investigations different proxies for aerosol as well as cloud properties were used. The choice of the quantity describing cloud properties, i.e., the cloud optical thickness, cloud droplet size, and CDNC has no direct influence on the results as the obtained ACI values can be converted into one another (cf. Eq. (2.6), [*Feingold et al.*, 2001; *McComiskey et al.*, 2009]). In the listed studies the aerosol load is described with the aerosol particle extinction coefficient α, the aerosol optical thickness τ_a, the light scattering coefficient σ_sp,

the aerosol index AI, the APNC N_{a}, or the CCN concentration N_{CCN}. Only in cases for which the aerosol size distribution and type do not vary considerably, approaches employing these different proxies yield identical results because the corresponding ACI values are not physically equivalent. Although this complicacy is to be kept in mind, the comparison with the measurement uncertainties and especially the various obstacles of the approaches introduced in the Subsections 2.2.5 to 2.2.7 shows that the choice of different aerosol proxies are a minor source for differences between the corresponding ACI values. The proxies used to describe the aerosol load are listed in Table 2.1.

The obtained ACI_r parameters have a spread from 0.02 to 0.33 and thus cover almost the entire range of possible values (cf. Subsection 2.2.3). These large discrepancies are partly due to different measurement approaches and objectives as explained before. Generally, higher ACI values are derived from airborne in-situ measurements, which follow objective A for the investigation of aerosol-cloud interactions. Studies utilizing sattelite observations, which are restricted to the pursuit of objective B, obtain lower aerosol-cloud relationships. Further differences result from the investigation of different cloud regimes. E.g., marine clouds tend to be stronger affected from aerosol-cloud interactions than continental clouds [*Quaas et al.*, 2008; *Bellouin et al.*, 2013]. But there remain considerable differences between the results of studies employing similar measurement approaches for the investigation of similar cloud types. These differences point out the large uncertainties in the understanding of aerosol-cloud interactions, which are a major obstacle for a more precise analysis of the earth's radiative budget [*McComiskey and Feingold*, 2008].

Table 2.1: Derived ACI_{r} values from airborne in-situ, satellite-borne remote-sensing and ground-based remote-sensing measurements. The chosen proxy for the aerosol load is denoted in the third column because its choice may have an influence on the derived ACI_{r} value.

Authors, Year	Method	Aerosol Proxy	ACI_{r}
Raga and Jonas [1993]	airborne, in-situ	N_{a}	0.09
Martin et al. [1994]		N_{a}	0.25
Gultepe et al. [1996]		$N_{\mathrm{a}}, N_{\mathrm{CCN}}$	0.22
O'Dowd et al. [1999]		N_{a}	0.20
McFarquhar and Heymsfield [2001]		N_{a}	0.11
Ramanathan et al. [2001]		N_{a}	0.21–0.33
Twohy et al. [2005]		N_{a}	0.27
Lu et al. [2007]		N_{a}	0.19
Lu et al. [2008]		N_{a}	0.14
Zheng et al. [2011]		N_{CCN}	0.24
Terai et al. [2012]		N_{a}	0.18
Painemal and Zuidema [2013]		N_{a}	0.25–0.31
Nakajima et al. [2001]	satellite, passive remote sensing	N_{a}	0.17
Sekiguchi et al. [2003]		N_{a}	0.07–0.1
Quaas et al. [2004]		AI	0.012–0.04
Quaas et al. [2006]		τ_{a}	0.04
Quaas et al. [2008]		τ_{a}	−0.015–0.15
Kaufman et al. [2005]		AI	0.046–0.174
Bulgin et al. [2008]		τ_{a}	0.10–0.16
Lebsock et al. [2008]		AI	0.07
Bréon et al. [2002]	satellite, passive remote sensing and model	τ_{a}, AI	0.04–0.085
Chameides et al. [2002]		τ_{a}	0.17
Bellouin et al. [2013]		τ_{a}	−0.01–0.16
Costantino and Bréon [2013]	satellite, passive and active remote sensing	AI	0.15
Feingold et al. [2003]	ground-based remote sensing	α	0.1
Kim et al. [2003]		σ_{sp}	0.13
Kim et al. [2008]		σ_{sp}	0.15
Garrett et al. [2004]		σ_{sp}	0.15
McComiskey et al. [2009]		AI, N_{CCN}	0.14, 0.16

Chapter 3

Instrumentation

In this chapter, the instruments and additional data sources employed for the investigation of aerosol-cloud interactions are introduced. The described instruments are part of the Leipzig Aerosol and Cloud Remote Observations System (LACROS), which is operated by TROPOS [*Seifert et al.*, 2012]. This measurement platform comprises several ground-based in-situ and remote-sensing instruments, which are shown in Fig. 3.1. The instruments employed for quantitative measurements in this work are highlighted in green and rose color. Coordinated measurements were performed with these instruments to derive a comprehensive dataset of aerosol and cloud properties as well as the vertical air motion.

Section 3.1 describes the Multiwavelength Atmospheric Raman lidar for Temperature, Humidity, and Aerosol profiling (MARTHA), which is highlighted in green color in Fig. 3.1. This lidar is of extraordinary importance for this work because it was utilized to derive aerosol properties as well as cloud microphysical properties for the study of their correlation and thus the investigation of aerosol-cloud interactions. Further instruments which were employed to support these studies are explained in the following sections. These are the Doppler Wind Lidar WiLi (Section 3.2), an MWR (Section 3.3), and a cloud radar (Section 3.4). The chapter closes with Section 3.5, which deals with the Global Data Assimilation System (GDAS). Although not being a measurement instrument but a database, GDAS is listed here as it provides meteorological data utilized for this work. Parts of this chapter have been published in *Schmidt et al.* [2013] and are adopted without explicit citing.

3.1 Raman lidar MARTHA

In the scope of the present work, the multiwavelength Raman lidar MARTHA was employed to assess aerosol as well as cloud properties for investigations of aerosol-cloud interactions, which makes MARTHA to the key instrument of this work. High-quality profiles of several aerosol properties were derived with the methods presented in Chapter 4. Measurements of cloud microphysical properties with this lidar were made possible with the implementation of the dual-FOV Raman lidar technique, which is explained in Chapter 5.

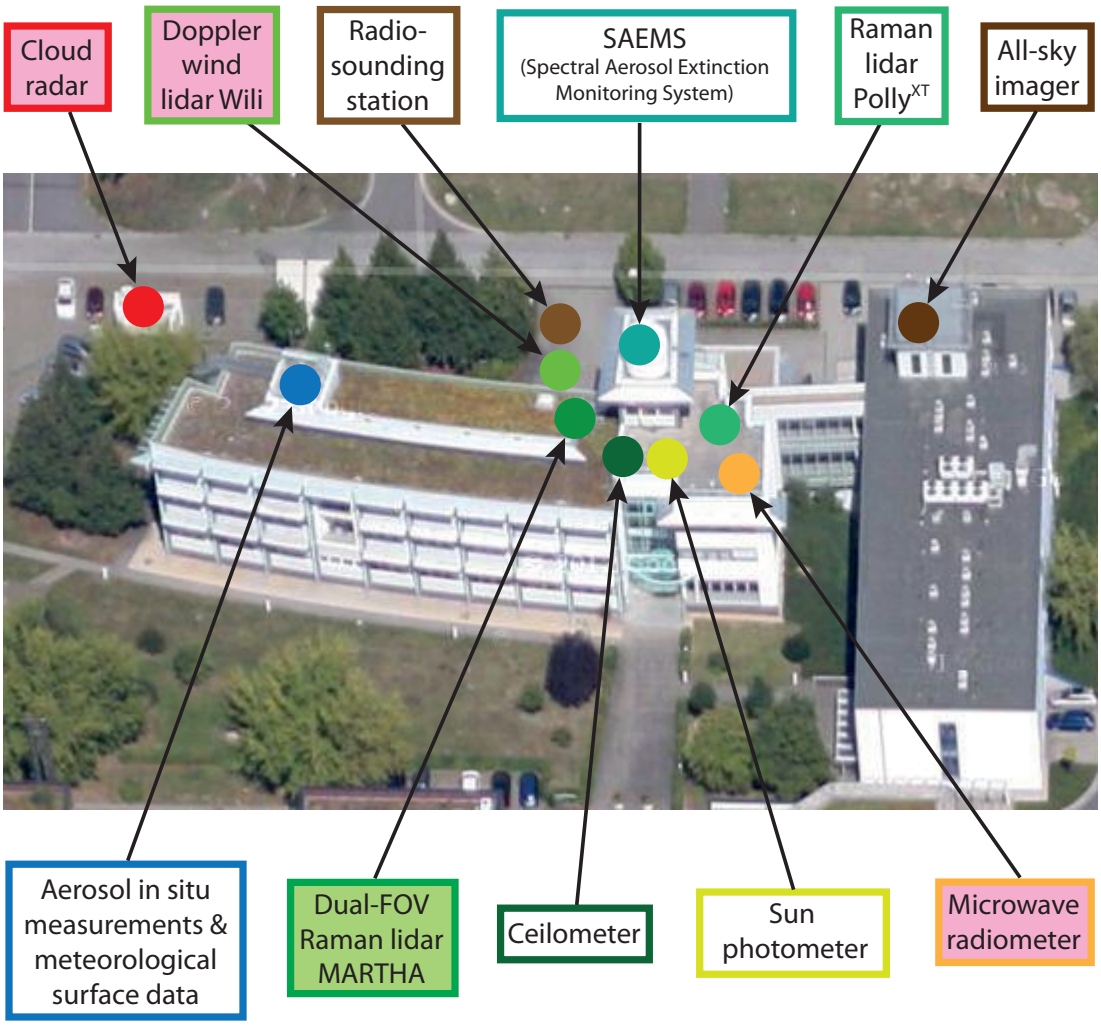

Figure 3.1: Instruments of the measurement platform LACROS at TROPOS. The dual-FOV Raman lidar MARTHA is highlighted in green color. The Doppler wind lidar WiLi and the MWR HATPRO, which are also used in this work, are highlighted with rose color.

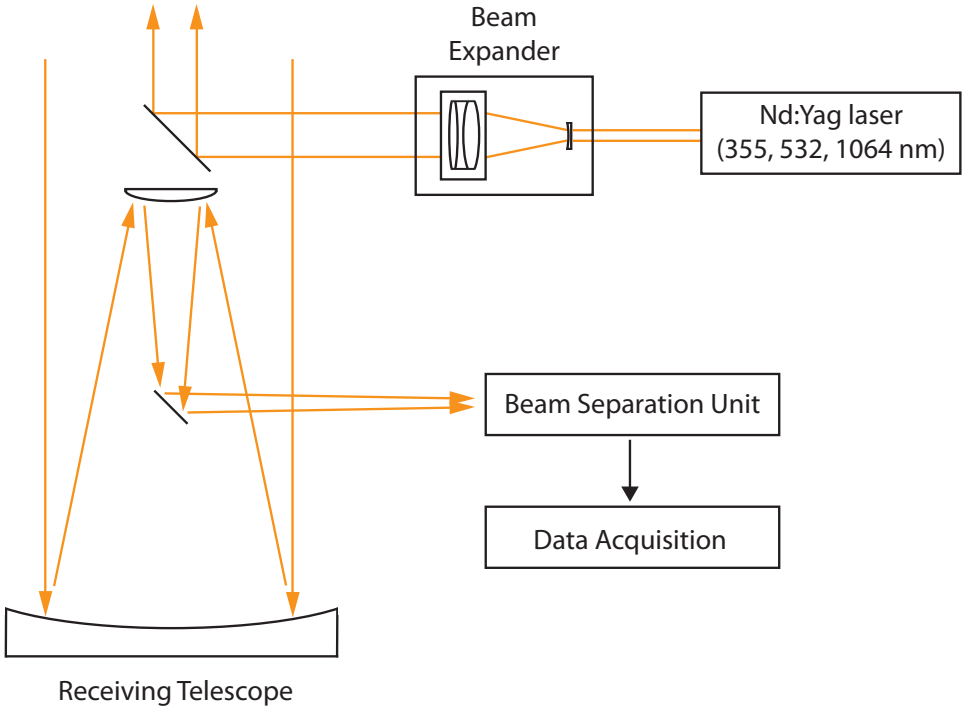

Figure 3.2: Scheme of the Raman lidar MARTHA. Its main parts are the Nd:YAG laser, beam expander, receiving telescope, beam separation unit and data acquisition system.

Beyond this work, the lidar is of particular importance for TROPOS due to the performance of long-term aerosol measurements in the framework of EARLINET as well as its utilization as a laboratory environment for the application of novel lidar techniques [*Mattis et al.*, 2002; *Arshinov et al.*, 2005; *Müller et al.*, 2011; *Ansmann et al.*, 2011]. Nevertheless, this section is restricted to the most important information because a detailed description of the system was provided by *Mattis et al.* [2002].

The basic setup of MARTHA is shown in Fig. 3.2. It comprises a transmitter, receiving telescope, a beam separation unit including detectors, and a data acquisition unit. In the following, the setup is explained in more detail.

The transmitter of MARTHA consists of a pulsed, Q-switched Nd:YAG laser operating with a repetition rate of 30 Hz. By second and third harmonic generation, light at wavelengths of 532 and 355 nm, respectively, is generated. The total pulse energy is 1.4 J, with 0.3 J at 355 nm, 0.6 J at 532 nm, and 0.5 J at 1064 nm. A beam expander with a magnification factor of 15 increases the beam diameter to 150 mm. Thus, the beam divergence is decreased to a turbulence-limited full angle of 0.1–0.2 mrad. The emitted laser beam and the optical axis of the receiver telescope are coaxial. The alignment of the laser beam is controlled with a camera displaying an image of the laser beam with respect to the telescope's FOV. Thus, the pointing of the laser beam can be easily adjusted with two remotely controlled actuators.

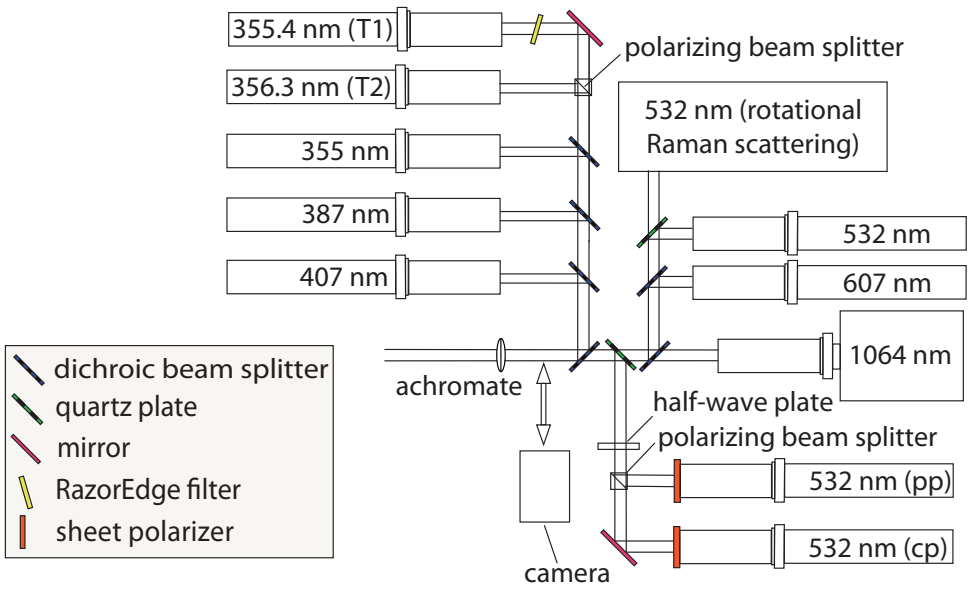

Figure 3.3: Beam separation unit of MARTHA with detection channels for the conventional lidar data analysis. The detection channels are labeled according to the detected wavelength. In case of polarization-sensitive detection, the plane of the detected polarization is denoted as well. The channel "532 nm (pp)" detects light which is parallel-polarized with respect to the polarization plane of the emitted laser light. Cross-polarized light is detected by the channel "532 nm (cp)". The channels "355.4 nm (T1)" and "356.3 nm (T2)" as well as the two channels which are depicted as a box labeld "532 nm (rotational Raman scattering)" detect different parts of the rotational Raman spectrum at 355 and 532 nm, respectively, for the retrieval of temperature profiles.

The backscattered light is received with a 0.8-m Cassegrain telescope, which has an effective focal length of 8974 mm. The light is reflected towards the beam separation unit, which is displayed in Fig. 3.3. There it is collimated with a system of achromatic lenses with a free aperture of 50 mm. Afterwards, the light is separated according to its optical properties by means of dichroic beam splitters, quartz plates, and polarizing beamsplitter cubes. It is detected with twelve channels, named according to the detected wavelength. The resulting signals are utilized for the conventional lidar data analysis as described in Chapter 4. The channels "355 nm", "532 nm", and "1064 nm" detect elastically backscattered light for the retrieval of profiles of the particle backscatter coefficient at the corresponding wavelength, as explained in Subsection 4.2.1. Light that is Raman scattered from nitrogen molecules is detected with the channels "387 nm" and "607 nm" for the determination of the profiles of the backscatter coefficients with the Raman method and the extinction coefficients at the corresponding wavelengths as described in Subsections 4.2.2 and 4.2.3. Further detection channels are employed to measure the polarization of the incoming light ("532 nm (pp)" and "532 nm (cp)"), water-vapor-to-dry-air mixing ratio ("407 nm"), and temperature ("355.4 nm (T1)", "356.3 nm (T2)", and "532 nm (rotational Raman scattering)") [*Mattis et al.*, 2002].

Except for the detection channels for the temperature measurement at 532 nm, which work with two successive diffraction gratings and fiber optics, the selection of the detected wavelengths is achieved with interference filters. In the channels detecting elastically scattered light, interference filters with a full width at half maximum (FWHM) of 5.0 nm are employed. The FWHMs for channels detecting Raman scattered light from nitrogen and water vapor molecules are 0.5 and 0.25 nm, respectively. After these filters an optical setup of an objective and an eyepiece is placed in the beam path. Thus, an image of the primary mirror of the telescope is displayed on the photocathodes of the photomultiplier tubes (PMTs), which are used to detected the incoming light. With this optical imaging a dependence of the PMT sensitivity on backscattering height is avoided [*Freudenthaler*, 2004].

The signals from the detection channels which are relevant for this work and are shown in Fig. 3.3 were recorded with the data acquisition system Purana from MEDAV, Uttenreuth, Germany, until May 2012. The raw spatial resolution is 15 m covering an altitude range of 15 km. This limited height range is an obstacle for a straightforward correction of the signal background in the case of cloud-free measurements, i.e., at measurements during cloud gaps to assess high-quality profiles of aerosol properties. Therefore, in May 2012 the Purana system was replaced with the new data acquisition system CNT80, developed at the Max Planck Institute for Meteorology in Hamburg and at TROPOS. It features an increased height resolution of 7.5 m and a larger altitude range covered by the measurements of about 45 km. Furthermore, the system allows for pretrigger data acquisition, i.e., the recording of the measured signals several microseconds before the emission of the laser pulse, for a more accurate correction of the signal background. Usually, the Purana as well as the CNT80 system were run with a temporal resolution of 4 s. With this comparatively high resolution, the effect of cloud inhomogeneities on the retrieved cloud properties can be minimized (cf. Section 5.7).

3.2 Doppler wind lidar WiLi

The container-based, mobile, coherent Doppler wind lidar WiLi measures the vertical wind speed with an uncertainty of about 0.1 m/s. It consists of a master oscillator and a power amplifier. In both lasers the active medium is a Tm:LuAG crystal. The lidar emits laser pulses with an energy of 1.5 mJ at a wavelength of 2022.5 nm. The pulse repetition rate is 750 Hz. A telescope with a free aperture of 140 mm is used for transmitting the laser pulse as well as receiving the backscattered light. The lidar works with the heterodyne detection method. The system derives profiles of the vertical wind velocity with a height resolution of 75 m. A temporal averaging time of 3 s is sufficient to obtain well-analyzable spectra. Besides measurements of the vertical component of the wind speed, WiLi is capable of deriving the horizontal wind speed by means of conical scans which can be performed with its fast hemispherical scanner. Further technical details can be found in *Engelmann et al.* [2008] and *Bühl et al.* [2012]. The two-dimensional deconvolution method was employed

by *Bühl et al.* [2012] to remove artifacts of the laser chirp. This method is of particular importance for undisturbed measurements of the vertical wind velocity at cloud base.

WiLi measurements were performed at Leipzig, Germany, in the time period from 2010 to 2012. WiLi was placed close to MARTHA within a distance of about 10 m and pointed exactly to the zenith. Thus, MARTHA and WiLi probed identical cloud volumes, considering the averaging times required for the dual-FOV Raman lidar measurements (cf. Subsection 6.2.3). About 100 h of combined cloud measurements with WiLi and the dual-FOV Raman lidar MARTHA were performed in this time period, which cover approximately 100 cloud probings. The obtained dataset was utilized to derive the vertical wind speed for the investigation of the influence of the vertical wind speed on cloud microphysical properties (cf. Section 7.3 and Subsection 8.3.5).

3.3 Microwave radiometer

An MWR is a passive remote-sensing instrument for the detection of microwave radiation which is emitted by the constituents of the atmosphere [*Cimini and Westwater*, 2010]. The measurements are performed with several detection channels. Channels working in the frequency range of 22 to 30 GHz are sensitive to water vapor and liquid water and are used to derive the LWP of clouds as well as the integrated water vapor of the atmosphere. Further detection channels operate at frequencies between 51 and 59 GHz to determine the temperature profile, which can be obtained through elevation scanning. Since 13 March 2011, a HATPRO MWR [*Rose et al.*, 2005], manufactured by the Radiometer Physics GmbH, is employed at TROPOS. Further technical details of HATPRO can be found in *Radiometer Physics GmbH* [2013]. The HATPRO is located about 10 m from MARTHA and was mainly used to derive the LWP of the probed clouds.

The typical uncertainity of LWP measurements with MWR, employing conventional data analysis methods, is about 15 to 30 $\mathrm{g/m^2}$ [*Westwater et al.*, 2001; *Crewell and Löhnert*, 2003; *Gaussiat et al.*, 2007; *Ebell et al.*, 2011]. As LWPs of thin, layered clouds are of similar magnitude, this large error inhibits to gain relevant information about the properties of those clouds. However, the largest contribution to the LWP error originates from an offset of the measured brightness temperature and only about a fifth is caused by its signal-to-noise ratio [*Crewell and Löhnert*, 2003]. Hence, *Gaussiat et al.* [2007] introduced a method for the correction of this offset. Ceilometer or lidar measurements are used to identify cloud-free periods. The LWP retrieved with the HATPRO is calibrated in cloud-free periods to $0\,\mathrm{g/m^2}$. Thus, the error of the retrieved LWP is less than 10%, increasing with time to the nearest clear-sky event. For most cloud probings performed in this work the dual-FOV Raman lidar measurement itself could be used for the identification of the nearest cloud-free time period. However, in some measurements the nearest clear-sky event occurred before or after the corresponding dual-FOV lidar measurement. In these cases, the ceilometer which is operated at TROPOS could be used for the identification of the clear-sky event. The

ceilometer is located in a distance of less than 10 m from MARTHA and operated around the clock.

3.4 Cloud radar

The application of radar in cloud research is a wide field. This section provides only a brief overview of radar cloud probings. Details can be found in *Montopoli and Marzano* [2010]. Besides probings and investigations of precipitation, a major objective for meteorological radar application is the study of cloud properties. Measurements with frequencies of 35 or 90 GHz are performed to monitor the cloud structure, i.e., cloud base and top height. Furthermore, cloud microphysical properties, as for example the cloud droplet effective radius, can be obtained when radar observations are supported with MWR probings or even additionally with ceilometer or lidar measurements [*Frisch et al.*, 2002; *Löhnert et al.*, 2004; *Brandau et al.*, 2010; *Martucci and O'Dowd*, 2011]. Radar cloud probings are performed with ground-based instruments, also within measurement networks as CLOUDNET [*Illingworth et al.*, 2007].

Since 11 August 2011 regular measurements are performed at LACROS with the cloud radar MIRA-35. This instrument was manufactured by the METEK GmbH. Details of the instrument can be found in *Metek GmbH* [2013]. In this work, radar measurements were utilized for the detection of drizzle, which disturbs the lidar probings of clouds but is hard to detect with lidar. Thus, due to the availability of radar measurements, the analysis of drizzling clouds could be avoided at least since August 2011. Furthermore, radar measurements were utilized for the detction of the cloud top height.

3.5 Global data assimilation system meteorological data

For profiles of temperature and pressure, utilized in this work, data of the U. S. National Weather Service's National Center for Environmental Prediction (NCEP) were used. These NCEP data are based on GDAS[1] [*Kanamitsu*, 1989]. GDAS stores assimilated, observational, meteorological data, which are used to initialize runs of weather forecast models. Surface observations are used as well as data from radiosondes and satellite-based instruments. Meteorological standard properties are stored with a horizontal resolution of $1^\circ \times 1^\circ$. The dataset has 23 vertical layers up to about 30 km height and is available every three hours. The GDAS grid point that is closest to Leipzig, Germany, is located at 51.10° N and 12.50° E with a distance of about 25 km to TROPOS.

[1] Information and data of the GDAS archive available at: http://www.arl.noaa.gov/gdas.php

Chapter 4

Standard lidar methodology: Aerosol analysis

In this work, Raman lidar measurements, performed with MARTHA, were utilized for the analysis of aerosol properties. The employed methods are explained here. First of all, Section 4.1 introduces the lidar equation, which constitutes the basis for the methods explained afterwards in Section 4.2. The descriptions are kept short as the application of these lidar methods is common.

4.1 Lidar principle and lidar equation

Lidar is the acronym for light detection and ranging. A laser pulse is emitted into the atmosphere. Photons that are backscattered from molecules or particles are detected with a receiver unit, which typically consists of a telescope and a detection system. The volume from which the telescope can receive photons is called field of view (FOV) and is in general defined with a field stop in or close by the focal plane of the telescope. The received photons are detected with high temporal resolution. From the time t between the emission of the laser pulse and the detection of the backscattered photons, the height z of the scattering volume above the lidar can be calculated from

$$z = \frac{tc}{2}, \tag{4.1}$$

with the speed of light c, when the lidar is pointing vertically.

The lidar equation (e.g., [*Wandinger*, 2005])

$$P_{\lambda_0}(z) = P_0 \frac{O(z)}{z^2} C_i \beta_{\lambda_0}(z) \exp\left[-2 \int_0^z \alpha_{\lambda_0}(\zeta) \mathrm{d}\zeta\right] \tag{4.2}$$

describes the power P_{λ_0} received from the lidar from elastic backscattering at the laser wavelength λ_0. It depends on the emitted power P_0, the height-independent system constant C_i for the utilized detection channel i, the overlap function O, the volume backscatter coefficient

β_{λ_0} of the backscattering volume, and the volume extinction coefficient α_{λ_0} along the path between the backscattering volume and the lidar at the wavelength λ_0.

From the photons arriving at the receiving telescope, only a height-dependent part can pass to the beam separation unit. This fraction is the value of O in the corresponding height. The overlap function O increases from 0 to 1 with altitude, affecting the measured signal and thus the derived quantities in heights below it reaches 1. However, with the knowledge of the overlap function, the measured lidar signals can be corrected for this overlap effect down to an altitude where the gradient of the overlap function becomes too steep and thus dominates the signal. Below this altitude, lidar data cannot be evaluated due to the overlap-implicated loss of sensitivity of the lidar.

The backscatter coefficient β_{λ_0} as well as the extinction coefficient α_{λ_0} employed in the Lidar Equation (4.2) consist of molecular (superscript mol) and particle (superscript par) contributions. Hence, these coefficients can be split into a molecular ($\alpha_{\lambda_0}^{\mathrm{mol}}$, $\beta_{\lambda_0}^{\mathrm{mol}}$) and a particle part ($\alpha_{\lambda_0}^{\mathrm{par}}$, $\beta_{\lambda_0}^{\mathrm{par}}$):

$$\alpha_{\lambda_0}(z) = \alpha_{\lambda_0}^{\mathrm{mol}}(z) + \alpha_{\lambda_0}^{\mathrm{par}}(z) \tag{4.3}$$

$$\beta_{\lambda_0}(z) = \beta_{\lambda_0}^{\mathrm{mol}}(z) + \beta_{\lambda_0}^{\mathrm{par}}(z) \tag{4.4}$$

The profiles of $\alpha_{\lambda_0}^{\mathrm{mol}}$ and $\beta_{\lambda_0}^{\mathrm{mol}}$ can be calculated for given temperature and pressure [*Bucholtz*, 1995]. E.g., the molecular backscatter coefficient can be derived by

$$\beta_{\lambda_0}^{\mathrm{mol}}(z) = N^{\mathrm{mol}}(z)\sigma_{\lambda_0}^{\mathrm{mol}}\Phi_{\lambda_0}^{\mathrm{mol}}(180^\circ) \tag{4.5}$$

with the number concentration N^{mol} of the scattering molecules, their scattering cross section $\sigma_{\lambda_0}^{\mathrm{mol}}$ at the corresponding wavelength λ_0, and the value of the corresponding phase function Φ_{λ_0} (cf. Subsection 5.1.1) for scattering angles of 180°(backscattering). Thus, the particle backscatter and extinction coefficients remain as the only unknown quantities in the Lidar Equations (4.2) and (4.6).

The Lidar Equation (4.2) is the basic equation for the retrieval of optical particle properties with an elastic backscatter lidar. In the case of a Raman lidar, as applied for this work, inelastically backscattered light is detected additionally. The power $P_{\lambda_{\mathrm{Ra}}}$ received by the lidar from Raman backscattering by atmospheric molecules (e.g., nitrogen) is described by

$$P_{\lambda_{\mathrm{Ra}}}(z) = P_0 \frac{O(z)}{z^2} C_i \beta_{\lambda_0}^{\mathrm{Ra}}(z) \exp\left\{ -\int_0^z \left[\alpha_{\lambda_0}(\zeta) + \alpha_{\lambda_{\mathrm{Ra}}}(\zeta)\right] \mathrm{d}\zeta \right\}, \tag{4.6}$$

with the the volume extinction coefficient $\alpha_{\lambda_{\mathrm{Ra}}}$ at the shifted wavelength λ_{Ra} and the backscatter coefficient for vibrational-rotational Raman scattering $\beta_{\lambda_0}^{\mathrm{Ra}}$ for light with a wavelength of λ_0. Similarly to Eq. (4.5), this backscatter coefficient can be derived by

$$\beta_{\lambda_0}^{\mathrm{Ra}}(z) = N^{\mathrm{Ra}}(z)\sigma_{\lambda_0}^{\mathrm{Ra}}\Phi_{\lambda_0}^{\mathrm{Ra}}(180^\circ), \tag{4.7}$$

with the number concentration N^{Ra} of the molecules where Raman scattering events may occur leading to the shifted wavelength λ_{Ra}, the corresponding scattering cross section $\sigma_{\lambda_0}^{\mathrm{Ra}}$, and the value of the corresponding phase function $\Phi_{\lambda_0}^{\mathrm{Ra}}$ for backscattering.

4.2 Data analysis

The following subsections give a brief overview about the conventional methods for the analysis of lidar data. Details can by found in *Ansmann and Müller* [2005].

4.2.1 Backscatter coefficient – Klett-Fernald method

In the Lidar Equation (4.2) there is only one measured variable P_{λ_0} but two unknown quantities α and β. Nevertheless, the backscatter and extinction coefficient can be retrieved with the assumption of a given extinction-to-backscatter ratio S^{par} of the scattering particles, which is also called lidar ratio. It is defined as

$$S^{\mathrm{par}}(z) = \frac{\alpha^{\mathrm{par}}(z)}{\beta^{\mathrm{par}}(z)} \tag{4.8}$$

and depends on the measured wavelength and particularly the aerosol type. Thus, the particle backscatter coefficient can be retrieved from the Lidar Equation (4.2) [*Klett*, 1981; *Fernald*, 1984]:

$$\beta^{\mathrm{par}}_{\lambda_0}(z) = -\beta^{\mathrm{mol}}_{\lambda_0}(z) + \frac{U(z_0, z)}{V(z_0) - 2S^{\mathrm{par}} \int_{z_0}^{z} U(z_0, r)\mathrm{d}r} \tag{4.9}$$

with

$$U(z_0, z) = P_{\lambda_0}(z) z^2 \exp\left[-2(S^{\mathrm{par}} - S^{\mathrm{mol}}) \int_{z_0}^{z} \beta^{\mathrm{mol}}_{\lambda_0}(\zeta)\mathrm{d}\zeta\right] \tag{4.10}$$

and

$$V(z_0) = \frac{P_{\lambda_0}(z_0) z_0^2}{\beta^{\mathrm{par}}_{\lambda_0}(z_0) + \beta^{\mathrm{mol}}_{\lambda_0}(z_0)}. \tag{4.11}$$

The extinction-to-backscatter ratio of air S^{mol} is given by $S^{\mathrm{mol}} = \frac{8\pi}{3} K$ [*Collis and Russel*, 1976] with K being the King factor.

This approach requires the estimate of a reference value $\beta^{\mathrm{par}}_{\lambda_0}(z_0)$. Usually, the corresponding reference height z_0 is chosen in an cloud-free height with a low aerosol load where $\beta^{\mathrm{par}}_{\lambda_0}(z_0) \ll \beta^{\mathrm{mol}}_{\lambda_0}(z_0)$.

As the three wavelengths of 355, 532, and 1064 nm are emitted and detected by the Raman lidar MARTHA, three particle backscatter coefficients $\beta^{\mathrm{par}}_{355}$, $\beta^{\mathrm{par}}_{532}$, and $\beta^{\mathrm{par}}_{1064}$ at the corresponding wavelengths can be retrieved.

4.2.2 Backscatter coefficient – Raman method

The assumption of a lidar ratio in the Klett-Fernald method can introduce large errors of more than 100% [*Sasano et al.*, 1985]. These errors are avoided with the Raman method by the utilization of a second measured quantity, which is $P_{\lambda_{\mathrm{Ra}}}$. Thus, the particle backscatter

coefficient can be obtained from the Lidar Equations (4.2) and (4.6) according to *Ansmann et al.* [1992a]:

$$\beta_{\lambda_0}^{\mathrm{par}}(z) = \left[\beta_{\lambda_0}^{\mathrm{par}}(z_0) + \beta_{\lambda_0}^{\mathrm{mol}}(z_0)\right] \frac{P_{\lambda_0}(z) P_{\lambda_{\mathrm{Ra}}}(z_0) N_{\mathrm{Ra}}(z)}{P_{\lambda_{\mathrm{Ra}}}(z) P_{\lambda_0}(z_0) N_{\mathrm{Ra}}(z_0)} \times \frac{\exp\left\{-\int_{z_0}^{z} \left[\alpha_{\lambda_{\mathrm{Ra}}}^{\mathrm{par}}(\zeta) + \alpha_{\lambda_{\mathrm{Ra}}}^{\mathrm{mol}}(\zeta)\right] \mathrm{d}\zeta\right\}}{\exp\left\{-\int_{z_0}^{z} \left[\alpha_{\lambda_0}^{\mathrm{par}}(\zeta) + \alpha_{\lambda_0}^{\mathrm{mol}}(\zeta)\right] \mathrm{d}\zeta\right\}} - \beta_{\lambda_0}^{\mathrm{mol}}(z), \tag{4.12}$$

with the number density of nitrogen molecules N_{Ra}, which can be calculated from the profiles of temperature and pressure (cf. Eq. (4.7)) [*Bucholtz*, 1995]. The reference height z_0 is to be chosen as for the Klett-Fernald method.

An advantage of this method is the utilization of the ratio of two measured lidar signals. As the overlap functions are identical for both signals for an ideal lidar, they cancel out in the calculation of the signal ratio. Therefore, the Raman method can be applied even in low altitudes where the overlap function is far from reaching 1.

4.2.3 Extinction coefficient

In the Lidar Equation for Raman backscattering (4.6) $\beta_{\lambda_{\mathrm{Ra}}}$ is known via N_{Ra} from the profiles of temperature and pressure (cf. Eq. (4.7)). Thus, the equation can be solved for $\alpha_{\lambda_0}^{\mathrm{par}}$ [*Ansmann et al.*, 1990]:

$$\alpha_{\lambda_0}^{\mathrm{par}}(z) = \frac{\frac{\mathrm{d}}{\mathrm{d}z} \ln \frac{N_{\mathrm{Ra}}(z)}{z^2 P_{\lambda_{\mathrm{Ra}}} / O(z)} - \alpha_{\lambda_0}^{\mathrm{mol}}(z) - \alpha_{\lambda_{\mathrm{Ra}}}^{\mathrm{mol}}(z)}{1 + \left(\frac{\lambda_0}{\lambda_{\mathrm{Ra}}}\right)^{\mathring{a}_\alpha}} \tag{4.13}$$

with the Ångström exponent $\mathring{a}_\alpha$, which describes the wavelength dependence of the particle extinction coefficient (cf. Eq. (4.16)). As the extinction coefficient is calculated from the derivative of the Raman signal, even with the typically ten times larger vertical and temporal averaging lengths and periods, respectively, its signal-to-noise ratio is significantly lower than for methods utilizing the lidar signals directly, e. g., the methods calculating the backscatter coefficient (cf. Subsections 4.2.1 and 4.2.2). With the two Raman detection channels of MARTHA with the wavelengths of 387 and 607 nm the particle extinction coefficients $\alpha_{355}^{\mathrm{par}}$ and $\alpha_{532}^{\mathrm{par}}$ can be retrieved. Hence, together with the particle backscatter coefficients $\beta_{355}^{\mathrm{par}}$ and $\beta_{532}^{\mathrm{par}}$, the lidar ratios at 355 and 532 nm can be derived (cf. Eq. (4.8)).

4.2.4 Ångström exponent

Besides the aerosol particle backscatter and extinction coefficients and the lidar ratio the Ångström exponent is another aerosol optical property which can be retrieved from lidar measurements. It describes the spectral dependence of the aerosol optical properties

[*Ångström*, 1964; *Ansmann and Müller*, 2005]. From measurements of MARTHA, the particle backscatter-related Ångström exponents

$$\mathring{a}_{\beta_{355/532}} = -\frac{\ln\left[\beta^{\mathrm{par}}_{532}(z)/\beta^{\mathrm{par}}_{355}(z)\right]}{\ln\left(532/355\right)} \tag{4.14}$$

and

$$\mathring{a}_{\beta_{532/1064}} = -\frac{\ln\left[\beta^{\mathrm{par}}_{1064}(z)/\beta^{\mathrm{par}}_{532}(z)\right]}{\ln\left(1064/532\right)} \tag{4.15}$$

as well as the particle-extinction-related Ångström exponent

$$\mathring{a}_{\alpha_3 55/532} = -\frac{\ln\left[\alpha^{\mathrm{par}}_{532}(z)/\alpha^{\mathrm{par}}_{355}(z)\right]}{\ln\left(532/355\right)}. \tag{4.16}$$

can be derived.

4.2.5 Microphysical particle properties by inversion

Vertical profiles of aerosol microphysical properties can be derived from measured profiles of the backscatter coefficients at three wavelengths (355, 532 and 1064 nm) and extinction coefficients at two wavelengths (355 and 532 nm) with an inversion algorithm [*Müller et al.*, 1999a,b; *Veselovskii et al.*, 2004; *Ansmann and Müller*, 2005; *Kolgotin and Müller*, 2008]. The algorithm retrieves the aerosol particle effective radius, volume concentration, APNC, the complex refractive index, and further aerosol microphysical properties.

Chapter 5

Dual-field-of-view Raman lidar: Cloud analysis

This chapter deals with the dual-FOV Raman lidar technique. As multiple scattering is the basis for dual-FOV Raman lidar measurements, Section 5.1.1 gives an introduction into this topic. Afterwards, the principle of the dual-FOV Raman lidar technique is explained in Section 5.2. Furthermore, this section describes the implementation of this technique in the Raman lidar MARTHA and the quality assurance of the realized setup. The algorithm utilized for the analysis of dual-FOV Raman lidar measurements as well as its adaptation to the setup of the Raman lidar MARTHA is presented in Section 5.3. The retrievals of the LWC, CDNC, and cloud base height are explained in Sections 5.4, 5.5, and 5.6, respectively. The chapter closes with a description of the scheme for the analysis of dual-FOV Raman lidar measurements, i.e., the pre- and postprocessing of the measured data, in Section 5.7. Parts of this chapter have been published in *Schmidt et al.* [2013] and *Schmidt et al.* [2014] and are adopted without explicit citing.

5.1 Lidar and multiple scattering

This section deals with the occurrence of multiple scattering in lidar measurements. After the explanation of the principles, three lidar approaches are introduced, which make use of multiple-scattering effects to derive information about the scattering medium. Thus, an overview is given about the state-of-the-art lidar approaches exploiting information from multiple-scattering-affected lidar signals, as does the dual-FOV Raman lidar technique.

5.1.1 Multiple scattering in lidar measurements

The lidar equations and the retrievals introduced in Chapter 4 are based on the assumption of single scattering, which means that no further scattering event occurs before or after the backscattering of the detected photons. This assumption complies very well in scattering

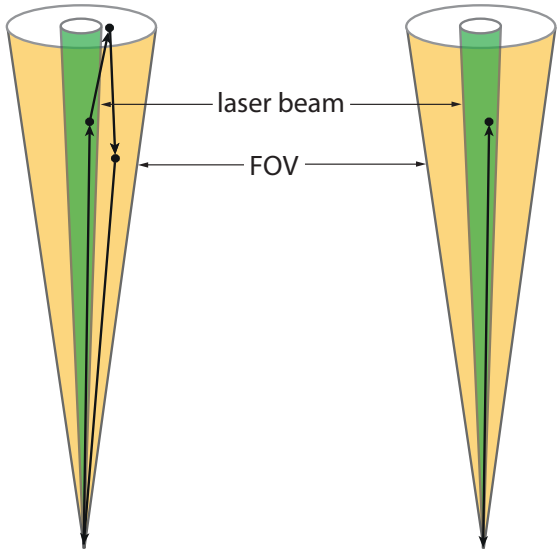

Figure 5.1: Path of a photon which is emitted from the laser and detected from the lidar. Scattering particles or molecules are shown as black dots. Left: multiple-scattering process consisting of several scattering events. Through multiple scattering the emitted photon leaves the volume of the laser beam. The photon is backscattered to the lidar from within the FOV and thus can be detected. For a comparison the right panel shows the path of a photon returning to the lidar after single scattering.

media that are optically thin and consist of scatterers that are smaller than or have a similar size as the employed wavelengths, as it is the case for conventional aerosol measurements.

In lidar probings of water clouds, which are considered in the following, multiply scattered light is detected. Fig. 5.1 illustrates a scattering process consisting of several scattering events. Photons are forward scattered by cloud droplets, which are larger than the measurement wavelength, with scattering angles close to 0° before or after a backscattering event. Fig. 5.2 compares the phase functions, which denote the relative occurrence of scattering angles for a scattering event, for scattering in clouds and molecular scattering. This figure illustrates the pronounced forward scattering peak for cloud droplets, which is the reason for the detection of multiply scattered light. Depending on cloud microphysical properties, up to 50% of the scattered light is scattered with angles smaller than 1° in forward direction [*Wandinger*, 1994].

The forward-scattered photons, which can be backscattered by subsequent scattering events and detected with the lidar, lead to a signal increase compared to the case in which these photons are extinguished. Thus, the obtained extinction coefficient is decreased, if single scattering is assumed. This effect may lead to errors of the retrieved extinction coefficient of up to 50% [*Wandinger*, 1998].

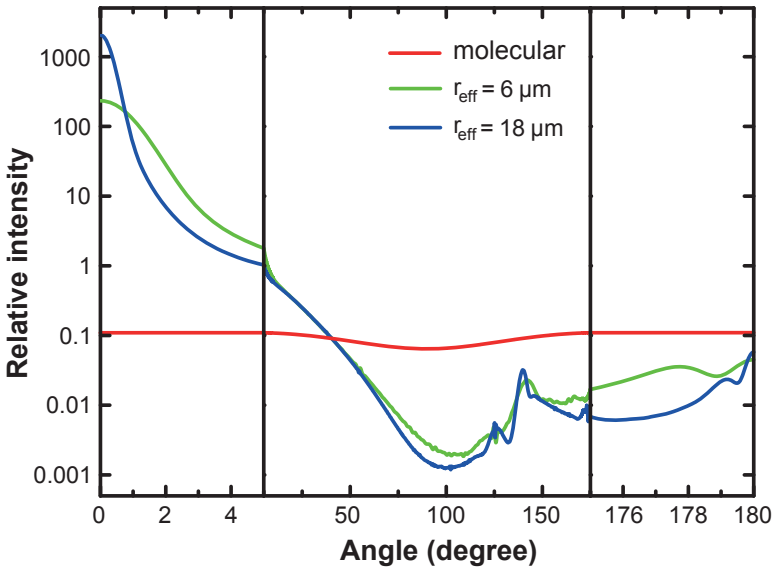

Figure 5.2: Phase function for scattering by cloud droplets with effective radii of 6 and 18 µm and molecular scattering at 532 nm. Scattering by droplets leads to a pronounced forward scattering peak.

Multiple-scattering processes may consist of solely elastic scattering events but may also contain a Raman scattering process. In the latter case, the photon is Raman backscattered by a molecule, e.g., nitrogen. The alternative multiple-scattering process, in which the Raman scattering process occurs in forward direction and the backscattering is elastic, has a much lower probability of about three orders of magnitude [*Deirmendjian*, 1969; *Wandinger*, 1994; *Malinka and Zege*, 2003]. This behavior is due to the strong forward scattering peak of cloud droplets whereas the molecular scattering is almost isotropic (see Fig. 5.2).

5.1.2 Multiple scattering lidar measurements for the retrieval of cloud properties

Despite the problems caused by multiple scattering in lidar measurements, the multiple-scattering effect may be used to derive additional information about the probed cloud. In the following subsections, three approaches used to derive cloud properties from multiple-scattering influenced lidar measurements are introduced.

Wide-angle FOV lidar

Wide-angle FOV lidars, also termed wide-angle imaging lidars or off-beam lidars, were introduced by *Love et al.* [2001] as well as *Cahalan et al.* [2005], who developed lidar systems working with extremely large FOVs of up to 60 °and 5.7 °, respectively. These angles are to be understood as a full angles as well as the following angles in this work regarding FOV,

laser beam divergence, or similar, unless stated otherwise. Due to the large FOV, the lidar signal can be recorded from large penetration depths up to 3 km. Both airborne [*Cahalan et al.*, 2005] as well as ground-based instruments [*Love et al.*, 2001] have been developed.

The approaches derive the angular distribution of the detected light from measurements with eight FOVs [*Cahalan et al.*, 2005] or time-resolved recordings of images of the full, wide FOV [*Love et al.*, 2001], which corresponds theoretically to an infinite number of FOVs. This information is utilized to determine the cloud geometrical and optical thickness as well as in the case of *Cahalan et al.* [2005] the profile of the cloud extinction coefficient.

The introduced approaches constitute valuable techniques for the investigation of cloud properties. Especially the large penetration depths, which are untypical for lidar techniques, are an important feature. However, the assumption of horizontal homogeneity [*Love et al.*, 2001; *Cahalan et al.*, 2005] is a constraint. Vertical inhomogeneities cause problems for the retrieval of *Love et al.* [2001]. The approach of *Cahalan et al.* [2005] has problems in dealing with clouds whose vertical variability deviates from idealized models of vertical variability of cloud properties. Furthermore, these measurements are restricted to night time, because the large FOVs lead to a strong background signal under daylight conditions. Still, the most important drawback of the wide-angle FOV lidar approaches is that these techniques are not capable of measuring cloud droplet size, LWC, and CDNC, which are all very important quantities for investigations of aerosol-cloud interactions.

Small-angle multiple-FOV lidar

The determination of cloud droplet size from multiple-FOV measurements becomes possible through the restriction of the measurement to small FOVs and thus small scattering angles in the forward direction [*Bissonnette*, 1996]. Hence, the small-angle approximation can be used for the treatment of the forward scattering in the corresponding retrieval algorithms. This approximation simplifies the analysis which can be seen in Fig. 5.2. There is a bijective correlation betweeen the width of the forward scattering peak of the phase function and droplet size for small forward scattering angles. Smaller droplets cause larger scattering angles. However, the limitation to smaller FOVs restricts the retrievals to smaller penetration depths compared to the approaches introduced in the previous subsection. On the other hand, the smaller FOVs assure the capabiliy of performing daylight measurements because the daylight signal background is much weaker than for the approaches explained in the previous section.

Bissonnette and Hutt [1995] used a lidar measuring elastically backscattered light with four FOVs to derive profiles of the extinction coefficient and droplet effective radius in water clouds. The size of the FOVs ranged from 4 to 40 mrad, which restricts the retrieval of the cloud properties to the lower part of the cloud up to an optical thickness of 4 to 4.5. Other multiple-FOV lidar setups are known, performing measurements with up to 32 FOVs with a maximum size of 12 mrad [*Bissonnette et al.*, 2002, 2005]. *Veselovskii et al.* [2006] suggested to use six FOVs for an optimum measurement setup to retrieve cloud droplet size.

For all the approaches mentioned in this and the previous subsection the number of measured signals (i.e., the number of employed FOVs) outnumber the two derived quatitities, which are the extinction coefficient and cloud droplet size. This high demand of required information is due to the complicated and irregular behavior of the phase function for the backscattering event at cloud droplets. Thus, the angular distribution of the backscattered light does not exclusively depend on the forward scatterering events, having a straighforward relationship between the scattering angle and cloud droplet size, but also on the complicated backscattering. The necessity of a high number of employed FOVs constitutes a drawback as it makes the retrieval algorithm and measurement setup more complicated and thus susceptible for errors.

Polarization lidar

Multiple scattering does not only alter the angular distribution of the detected light but also its state of polarization [*Pal and Carswell*, 1973, 1976; *Sassen and Petrilla*, 1986]. Hence, measurements of the polarization of the detected light can be used to derive cloud microphysical properties.

Hu et al. [2006] derived an empirical relationship between the accumulated depolarization ratio and the accumulated single-scattering fraction. *Roy and Cao* [2010] used this relationship for an inversion technique which is capable of retrieving the extinction coefficient within clouds from lidar measurements. Similar to the approach introduced in the previous subsection, the retrieval is limited to low optical depths, in this case optical depths less than 2.

An interesting combination of the small-angle multiple-FOV and the polarization lidar approaches was introduced by *Roy et al.* [1999]. The authors measured the polarization of the light detected in all of the 32 FOVs of the lidar that was used by *Bissonnette et al.* [2002] and *Bissonnette et al.* [2005]. In this way, the particle size distribution is obtained. However, the retrieval algorithm considers only scattering processes with one forward scattering event in order to keep it relatively straightforward. Hence, the analysis is limited to optical depths of 0.3 to 0.4, corresponding to a penetration depth of about 10 m only, which is a severe constraint for investigations of aerosol-cloud interactions.

5.2 Dual-field-of-view Raman lidar technique

In this section the dual-FOV Raman lidar technique is introduced. This technique was implemented in the Raman lidar MARTHA in the scope of this work. The technique was employed to retrieve cloud microphysical properties from lidar measurements. The measurement principle as well as the technical details of the measurement setup are explained. The section closes with the presentation of quality checks of the measurement setup.

5.2.1 Measurement principle

Three approaches to derive cloud properties with lidar measurements were presented in Subsection 5.1.2. The dual-FOV Raman lidar technique, which is the subject of this work, resembles the method of *Bissonnette and Hutt* [1995], described in Subsection 5.1.2. It also derives profiles of the extinction coefficient and droplet effective radius in water clouds from measurements of the angular dependence of the backscattered light within the small-angle approximation, i.e., for comparatively small FOVs. Similar to the work of *Bissonnette and Hutt* [1995], the work makes use of the bijective dependence of the width of the forward scattering peak, which is measured through the angular distribution of the received light, on the size of the scattering object, i.e., the cloud droplet, as illustrated in Fig. 5.2.

The major difference of the dual-FOV Raman lidar technique to the approach followed by *Bissonnette and Hutt* [1995] is the detection of light that is Raman scattered by nitrogen molecules. As the Raman scattering event occurs at the backscattering (cf. Subsection 5.1.1) and the scattering phase function for molecular scattering is almost isotropic (cf. Fig. 5.2), the detection of Raman-scattered light avoids an effect of the backscattering event on the angular distribution of the received light. Thus, the complex behavior of the phase function for the backscattering at cloud droplets (cf. Fig. 5.2), which hampers approaches detecting elastically scattered light, does not impair the dual-FOV Raman lidar retrieval. This advantage simplifies the retrieval algorithm significantly, allowing the reduction of the measurement setup to a straightforward and robust lidar working with only two FOVs of different size [*Malinka and Zege*, 2007]. However, the utilization of Raman scattering involves small scattering cross sections. The resulting comparatively weak signals restrict dual-FOV Raman lidar measurements to night time because in the larger FOV, where the background lighting is stronger, the signal cannot be separated from the daylight background.

5.2.2 Measurement setup

Hardware and measurement geometry

The measurement geometry of dual-FOV Raman lidar measurements is presented in Fig. 5.3. Light is detected with an inner, narrow FOV and an outer, wide FOV. In contrast to the inner FOV, the outer FOV is not a full cone but has an annular cross section. Furthermore, Fig. 5.3 shows two scattering processes, illustrating that smaller cloud droplets and the corresponding larger scattering angles in forward direction lead to a larger signal in the outer FOV.

Simultaneous measurements with two FOVs are rendered possible through the utilization of a mirror field stop, which is presented in Fig. 5.4. It consists of a dielectric mirror, which is high-reflective for wavelengths of 532 and 607 nm, with an elliptical bore and an elliptical obstruction. The mirror diaphragm is placed under an angle of 45° in the optical path. The projections under this angle of the bore and the obstruction are circular. As the light from the narrow, inner FOV is transmitted through the bore, the bore defines the inner FOV. Light from the annular, wide, outer FOV is reflected by the mirror. Thus, the size of

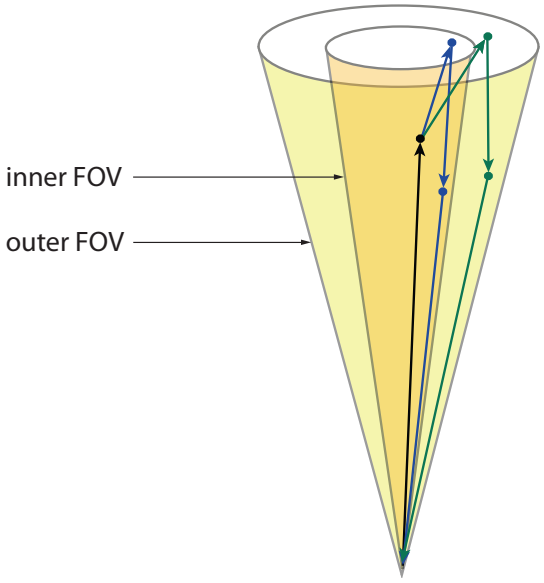

Figure 5.3: Dual-FOV measurement geometry. The inner, narrow FOV is shown in orange, the annular, outer FOV is displayed in yellow. Scattering particles or molecules are shown as black, green, and blue dots. Two multiple-scattering processes are illustrated: One photon is scattered with smaller forward scattering angles and detected from the inner FOV, which is typical for larger cloud droplets (blue). Another scattering process shows larger forward scattering angles, which leads to a detection in the outer FOV (green).

the obstruction defines the outer FOV. Both ellipses are centered at the optical axis of the receiver. Hence, the narrow and wide FOV are aligned to the same axis.

Figure 5.4 shows the complete beam separation unit of the Raman lidar MARTHA. In addition to Fig. 3.3 the beam paths of the channels detecting light from the outer FOV are shown as well. There, the light is collimated with a system of achromatic lenses with a free aperture of 74 mm. A dichroic beamsplitter separates the light into the detection channels for light of the wavelengths of 532 and 607 nm, detecting elastically scattered light and light that was Raman scattered by nitrogen molecules, respectively. The corresponding interference filters have FWHMs of 5.0 and 3.0 nm, respectively. A system of an objective and eyepiece is employed, similarly as in the detection channels for the inner FOV. The signals are detected with PMTs of the type R7400-U20 from Hamamatsu Photonics K.K., Hamamatsu City, Japan, which are employed in photomultiplier modules from Licel GmbH, Berlin, Germany.

Optimization of the measurement geometry

Malinka and Zege [2007] showed that the sensitivity of dual-FOV Raman lidar measurements to cloud microphysical properties depends strongly on the measurement geometry. Hence,

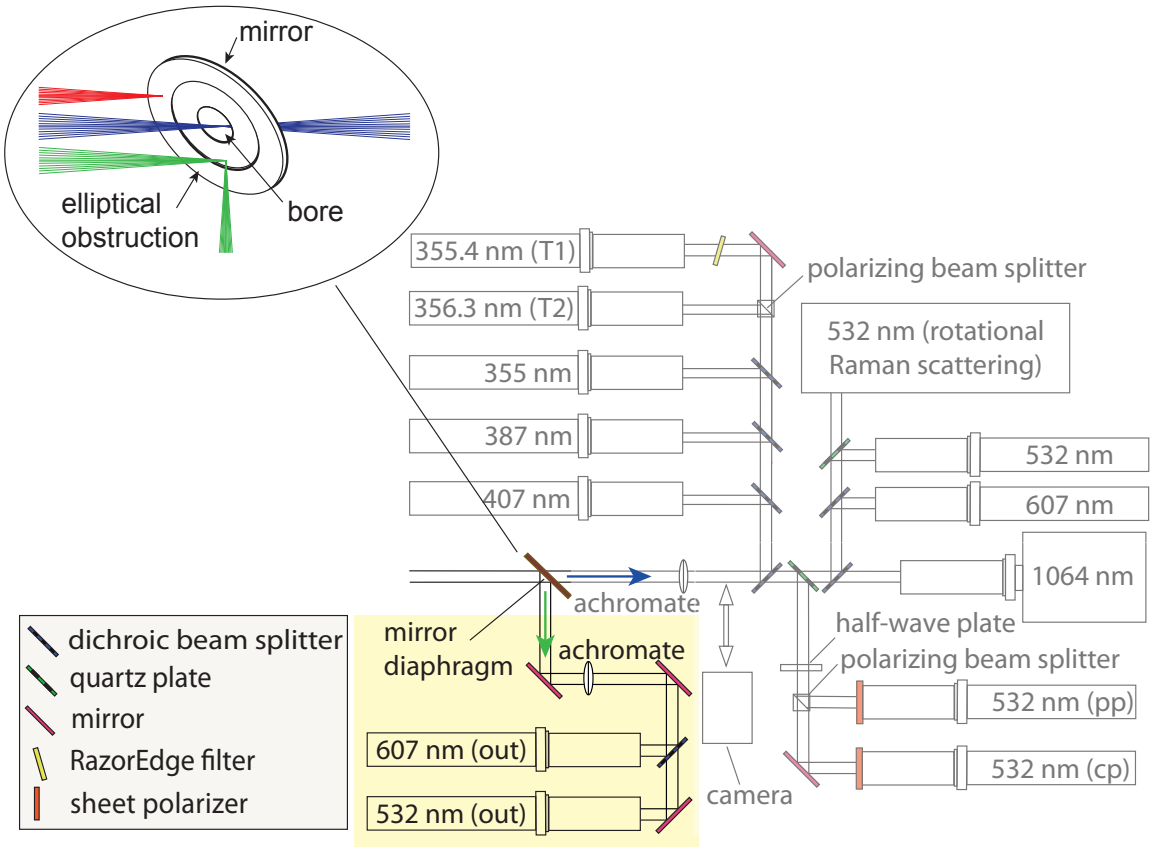

Figure 5.4: Beam separation unit of MARTHA. Light from the inner FOV (indicated with a blue arrow) is detected with the channels displayed in gray color, which correspond to the depiction of Fig. 3.3. Light from the outer FOV (indicated with a green arrow) is reflected towards the corresponding detection channels "532 nm (out)" and "607 nm (out)", which are highlighted with yellowish color and labeled according to the detected wavelength. Top left: illustration of the mirror diaphragm. Incoming light from the wide, annular FOV is reflected (green rays), incoming light from the narrow FOV is transmitted (blue rays). Light from outside both FOVs is blocked by the elliptical obstruction of the mirror diaphragm (red rays).

Table 5.1: Inner and outer FOVs, conjugate diameters for mirror diaphragms which can be employed in MARTHA, and cloud base heights for dual-FOV measurements with MARTHA, considering and not considering a tilt of the laser beam. For dual-FOV measurements the mirror diaphragm is chosen according to the altitude ranges considering a tilt of the laser beam.

Inner FOV	Conjugate Diameter Of Bore	Outer FOV	Conjugate Diameter Of Obstruction	Cloud Base Height	
				Laser Not Tilted	Laser Tilted
0.28 mrad	2.5 mm	0.78 mrad	7.0 mm	3.0–6.0 km	4.0–6.0 km
0.50 mrad	4.5 mm	2.00 mrad	18.0 mm	1.5–3.0 km	2.0–4.0 km
0.78 mrad	7.0 mm	3.80 mrad	36.0 mm	0.9–1.5 km	1.3–2.0 km

the authors gave recommendations for the sizes of the employed FOVs to optimize dual-FOV cloud probings. The optimum for the inner FOV γ_{in} is

$$\gamma_1 < \gamma_{\text{in}} < \gamma_2, \tag{5.1}$$

with

$$\gamma_1 = \max\left\{\gamma_{\text{s}}, \frac{D_{\text{r}}}{z_{\text{p}} + H}, \frac{D_{\text{s}}}{z_{\text{p}} + H}\right\}, \tag{5.2}$$

$$\gamma_2 = \gamma_{\text{s}} + \frac{D_{\text{r}}}{z_{\text{p}} + H} + \frac{D_{\text{s}}}{z_{\text{p}} + H}, \tag{5.3}$$

with the laser beam divergence $\gamma_{\text{s}} = 0.2\,\text{mrad}$, the aperture of the receiving telescope $D_{\text{r}} = 0.8\,\text{m}$, the laser beam diameter $D_{\text{s}} = 0.15\,\text{m}$, the penetration depth into the cloud z_{p}, and the cloud base height H. The recommendation for the size of the outer FOV γ_{out} is

$$\gamma_{\text{out}} = 0.01\frac{z_{\text{p}}}{H}. \tag{5.4}$$

The recommended size for the inner as well as for the outer FOV depends on the cloud base height. The receiving unit of MARTHA is set up in a way that it is possible to choose between three differently sized mirror diaphragms to enable cloud measurements with a high sensitivity to cloud properties in an extended altitude range from 1.3 to 6.0 km. The dimensions of the three different mirror diaphragms that can be employed and the corresponding pairs of FOV are listed in Table 5.1. Table 5.1 also shows altitude ranges for dual-FOV cloud measurements which comply with Eq. (5.1) and (5.4) and a penetration depth of $z_{\text{p}} = 200\,\text{m}$.

In the derivation of Eq. (5.1) and (5.4), a tilt of the laser beam against the optical axis of the telescope is not considered. However, due to the limited accuracy of the laser beam alignment, there is always a small tilt of the laser beam (cf. Subsection 5.2.3 and Section 5.3). The effect of a tilt of the laser beam on the overlap function is illustrated in Fig. 5.5. This figure shows overlap functions for the FOVs of 0.5 and 0.78 mrad with a non-tilted as well a tilted laser beam. The overlap functions were obtained with ray-tracing simulations with the

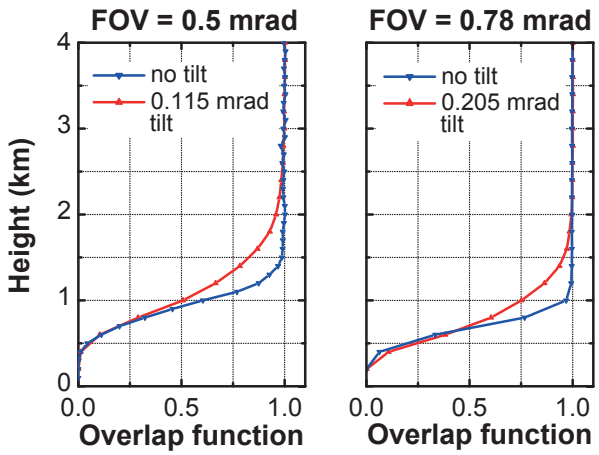

Figure 5.5: Overlap functions for MARTHA from ray-tracing simulations with and without a tilt of the laser beam of 0.115 and 0.205 mrad for a FOV of 0.5 and 0.78 mrad, respectively.

Software ZEMAX^{TM} as described by Reichardt et al. [*Reichardt et al.*, 2012]. The choice of the parameters used for the simulation is explained in Subsection 5.2.3 and Section 5.3. These parameters are listed in Table 5.2. The tilt of the laser beam for the FOVs of 0.5 and 0.78 mrad were 0.115 and 0.205 mrad, respectively (cf. Subsection 5.2.3 and Section 5.3).

A tilt of the laser beam leads to a weaker increase of the overlap function with height and thus shifts the optimum altitudes for cloud measurements upwards (cf. Table 5.1). At the altitudes relevant for cloud measurements, there is a height shift of 0.5 to 1.0 km between equivalent values of the overlap functions with and without the tilt of the laser beam. Thus, the altitude ranges of the clouds for the selection of the corresponding mirror diaphragm are corrected by these differences. In Table 5.1 the optimum cloud base heights for dual-FOV measurements with the corresponding mirror diaphragms, considering a tilt of the laser beam, are listed. These height requirements were applied for the performed dual-FOV cloud measurements.

Data acquisition

The signals from the detection channels for the outer FOV are recorded with the Licel transient recorder TR20-160. This data acquisition system is run synchronously with the Purana or CNT80 system, respectively, with a temporal resolution of 4 s. To increase the number of profiles which can be detected within each 4-s interval the maximum detection height is decreased from the maximum possible 120 to 30 km because the corresponding lower amount of data consumes less time for data storage and thus enables longer measurement times within each 4-s interval. Still, the 30 km signal range is far enough to do an accurate background correction of the measured signals. The raw spatial resolution is 7.5 m.

As the data acquisition systems for the signals from the inner and outer FOVs are triggered independently, the corresponding signals have to be corrected for a possible height

shift. This shift was determined from cloud measurements by comparing the measured cloud base height. The 0-m height of the Purana system was found to correspond to the height of 22.5 m in the Licel system. The 0-m height in the CNT80 system, identified by the recording of the emitted laser pulse through the pretrigger capability, corresponds to an altitude of 30 m in the Licel system.

Adaptation of signal intensity

To avoid effects of the PMT dead time on the measured signals, the intensity of the detected light is decreased with neutral-density filters in each detection channel separately. The optical density of the filters employed for the detection of light at 607 nm from the inner FOV is varied depending on cloud base height and aerosol properties between 0.2 and 1.1. For the detection of light at 607 nm from the outer FOV, filters with optical densities between 0 and 1.1 are used. With the appropriate setting of the neutral-density filters for each cloud measurement a maximum penetration depth into the cloud is achieved.

5.2.3 Quality checks of dual-FOV Raman lidar setup

Comparison of overlap functions derived from measurement and simulation: Effect of mirror diaphragm on overlap function

An exact knowledge of the overlap function is crucial for the retrieval algorithm described below. Therefore, the effect of employing a mirror diaphragm instead of a conventional field stop on the overlap function was investigated in detail. An ideal field stop has an infinite small thickness and is placed orthogonally to the optical axis in the optical path. The mirror diaphragm is 2 mm thick and is positioned under 45°. Ray-tracing simulations with the software ZEMAX^{TM} were performed to compare the overlap functions of the Raman lidar MARTHA employing the mirror diaphragm as well as an ideal field stop. Fig. 5.6 displays the obtained results: the simulated overlap functions (blue and green lines) agree very well. This finding demonstrates that the usage of a mirror diaphragm instead of an ideal field stop does not affect the overlap function and thus the measured lidar signals. Furthermore, the overlap function of the Raman lidar MARTHA was determined experimentally as decribed by *Wandinger and Ansmann* [2002]. This overlap function matches the simulated functions very well (see Fig. 5.6, red line), illustrating that the lidar system is well represented in the ray-tracing simulations.

The parameters used for the simulation are listed in Table 5.2. The given radius of the telescope's secondary mirror describes an obstruction at the center of the primary mirror in the ray-tracing simulations. The values for the FOV, radii of the telescope's mirrors, and radius of the laser beam were either measured directly or calculated from measurements. The effective focal length of the telescope was given by the trader (Astro Optik Philipp Keller, Neutraubling, Germany). To obtain a steeper increase of the overlap function, the field stop of the Raman lidar MARTHA is not placed in the focal plane of the telscope but slightly behind. Due to the large focal length of the receiving telescope, it is difficult to obtain an

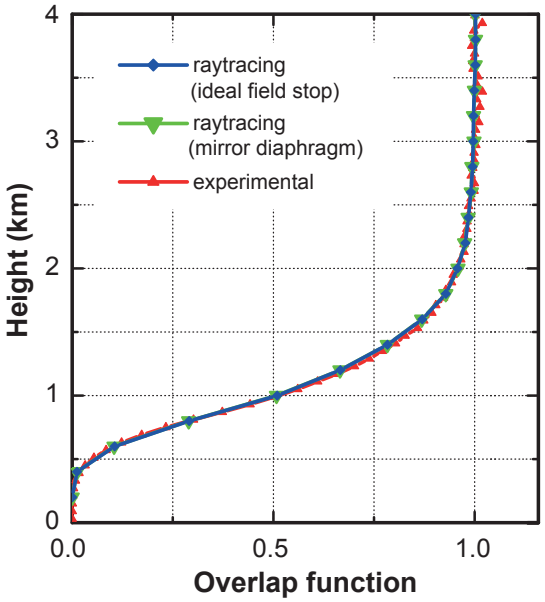

Figure 5.6: Overlap functions of MARTHA from ray-tracing simulations with ideal field stop (blue) and mirror field stop (green) as well as from measurement (red) for an FOV of 0.5 mrad.

exact measure of the distance between the focal plane of the telescope and the field stop. With the auto-collimation method, where a point light source is placed in the telescope's focal plane and a plane mirror behind the telescope reflects its light back into the focal plane *Wilson* [2001], it was determined to 20 ± 10 mm. The value was varied within this range to obtain the best fit of the overlap function obtained from the measurement and the ray-tracing simulations. Neither the divergence of the laser beam nor the tilt of the laser beam against the telscope's optical axis were measured directly. A rough estimate of the divergence of the laser beam of 0.1 mrad was made from the initial laser beam divergence obtained from the manufacturer's specification (1.5 mrad) divided by the beam's expansion factor of 15. Still, the divergence obtained in this way is influenced among other effects by diffraction at optical elements of the transmitting unit, atmospheric turbulence, a non-perfect setup of the beam expander, and thermal effects within the laser cavity. Thus, the laser beam divergence was varied within the boundaries of 0.08 to 0.3 mrad to obtain the best match between the measured and simulated overlap functions. The procedure to obtain the best-match value of the tilt of the laser beam was similar. From pictures of the camera, which is used to align the laser beam for the measurements, the range of possible tilts of the laser beam was estimated to be between 0 and 0.15 mrad.

Table 5.2: Parameters used for ray-tracing simulations of MARTHA's overlap functions which are shown in Fig. 5.6.

FOV	0.5 mrad
Radius of telescope's primary mirror	0.4 m
Radius of telescope's secondary mirror	0.11 m
Effective focal length of telescope	8974 mm
Radius of emitted laser beam	0.075 m
Distance of focal plane of telescope and field stop	15.4 mm
Divergence of laser beam	0.2 mrad
Tilt of laser beam	0.115 mrad

Angles of incidence in receiver: performance of dichroic beam splitters and interference filters

For a proper performance of the interference filters and dichroic beam splitters in the receiver, small deviations from the nominal angles of incidence of 0°and 45°, respectively, are required. In general, the deviations from the nominal angles of incidence increase with increasing FOV. In the dual-FOV technique large FOVs are employed, in particular for the outer FOVs. Thus, a check of the angles of incidence on the optical elements in the beam separation unit is necessary. The distribution of these angles was investigated with help of ray-tracing simulations with ZEMAX^{TM}. The lidar parameters for the simulations of the inner FOVs were the same as used for the retrieval of the overlap functions, listed in Table 5.2. The simulations for the outer FOVs were done with a virtual laser beam divergence of 2 and 4 mrad to account for the possible backscattering of photons from the entire volume of the outer FOV due to multiple scattering in clouds. Fig. 5.7 shows the angular distribution for inner FOVs of 0.5 and 0.78 mrad and outer FOVs of 2.0 and 3.8 mrad on the interference filters of the detection channels for different backscattering heights. Rays from the outer FOVs show much larger angular deviations from the optical axis than rays from the inner FOVs. Ray-tracing simulations show that the acceptance angles of the employed interference filters are of the order of 5°[*Schmidt*, 2009] with dichroic beamsplitters accepting deviations from their nominal angle of incidence of 45°of similar magnitude. Since all angles of incidence are well below this value, no effect of the limited angular acceptance of the dichroic beamsplitters and interference filters on the measured signals is expected.

5.2.4 Dual-FOV Raman lidar cloud probings with MARTHA: Overview

In the scope of this work 29 dual-FOV Raman lidar measurements of water clouds were performed with the described measurement setup. For the analyses of the measurements the forward iterative algorithm, described in the following section, was employed. Thereby, cloud properties could be derived up to a geometrical and optical penetration depths of 60 to 255 m and 1.2 to 4.1, respectively. The corresponding means are 140 ± 50 m and 2.8 ± 0.9.

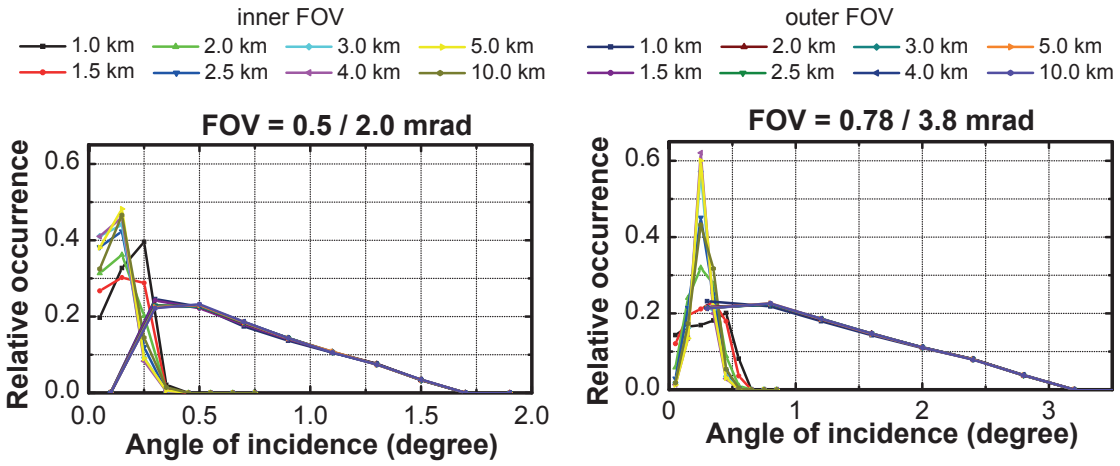

Figure 5.7: Distribution of angles of incidence on interference filters. Rays from the outer FOV have larger angles of incidence than rays from the inner FOV.

5.3 Forward iterative algorithm

This section describes the algorithm which was used for the evaluation of the performed dual-FOV Raman lidar measurements as well as its adaptation to the specific measurement geometry of the Raman lidar MARTHA.

5.3.1 Basic information

Malinka and Zege [2007] developed a forward iterative algorithm for the analysis of dual-FOV Raman lidar measurements. It uses Raman lidar signals from multiple scattering, measured synchronously with two FOVs as described in Sections 3.1 and 5.2, to retrieve profiles of the cloud droplet effective radius and extinction coefficient in water clouds. No assumptions on cloud properties, as for example adiabaticity, are made for the retrieval.

The algorithm makes use of a solution for analytical modeling of Raman lidar signals influenced by multiple scattering based on a small-angle approximation, published by *Malinka and Zege* [2003]. The scattering process of one or multiple elastic scattering events in forward direction and an inelastic backscattering event, leading to signals at the Raman-shifted wavelength, is considered.

In the algorithm the investigated cloud is assumed to consist of a number of homogeneous cloud layers, each with its own characteristics regarding extinction and effective radius. For each layer the extinction and effective radius are determined and thus profiles of the derived quantities are obtained. The number of layers can be set manually to balance the demands of a successful forward iteration and an adequate height resolution which is necessary to resolve the cloud's characteristics. Furthermore, the algorithm includes a function to set the number of cloud layers automatically according to the strength of the measured lidar signals in each height range. The altitude range for which the forward iterative algorithm is run is

chosen manually. More details regarding the selection of the number of cloud layers and the altitude range for the forward iteration are given in Section 5.7.

The algorithm runs iteratively. In the first run, the effective radii in all cloud layers are set to 9 µm. The extinction coefficient is set to the values calculated from the signal measured in the inner FOV, applying the single-scattering approximation. From these cloud properties the expected lidar signals of both FOVs are calculated analytically. The results are compared with the measured signals. The assumed cloud microphysical properties are adapted according to the comparison and used for the next iteration step by calculating the resulting lidar signals again. The iteration is stopped when the calculated signals converge. The difference d between the calculated and measured signal is calculated as

$$d = \sqrt{\frac{1}{n}\sum_{k=0}^{n}(\ln N_k^{\mathrm{meas}} - \ln N_k^{\mathrm{calc}})^2}, \tag{5.5}$$

with the count rates N_k^{meas} and N_k^{calc} of the measured and calculated signals in the k-th cloud layer, respectively, and the number of cloud layers n used in the forward iteration. If $d < 10^{-3}$ for the signals in both FOVs, the forward iteration is considered to be successful. The algorithm performs a maximum of 50 forward iterations. If the signal differences d remain larger than 10^{-3} or if the calculated signals do not converge to a stable solution, the forward iteration is declared as not successful and not used for further analysis.

5.3.2 Adaptation to measurement geometry

For analyzing dual-FOV measurements performed with the Raman lidar MARTHA, the forward iterative algorithm was adopted to the measurement geometry of the lidar, which is represented by the overlap function. A correct representation of the lidar parameters (e.g., tilt of laser beam, laser beam divergence, position of field stop) in the forward iterative algorithm is necessary, because the resulting measurement geometry has a strong effect on the dual-FOV lidar signals and thus the retrieved cloud microphysical properties. The measurement geometry can be characterized by the overlap function of the lidar system.

Functions which are part of the source code of the forward iterative algorithm were used to calculate the overlap function analytically [*Malinka and Schmidt*, 2010]. Fig. 5.8 shows a comparison of these overlap functions with the functions obtained experimentally and from ray-tracing simulations. The parameters for the ray-tracing simulation for the FOV of 0.5 mrad are identical to those given in Subsections 5.2.2 and 5.2.3 and are listed in Table 5.2. The simulation for the FOV of 0.78 mrad uses the same parameters except for a larger uncertainty in the tilt of the laser beam. For a larger FOV the image of the footprint of the FOV is larger which makes it more difficult to adjust the displayed laser beam to the center of the image causing a larger tilt of the laser beam. To find the best match between the measured and simulated overlap functions, the tilt was varied between 0 and 0.23 mrad, giving the best match at a tilt of 0.205 mrad.

The parameters used for the analytical calculation, which produced the best match with the overlap functions derived experimentally and from ray-tracing simulations, are utilized

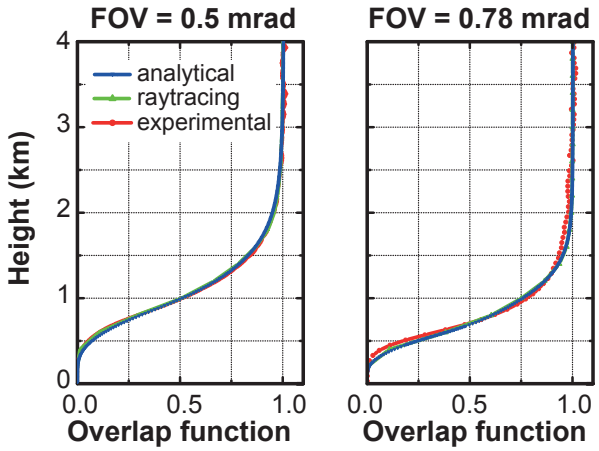

Figure 5.8: Overlap functions derived experimentally, analytically, and from ray-tracing simulations for inner FOVs of 0.5 and 0.78 mrad.

Table 5.3: Parameters for ray-tracing simulation and analytical calculation of the overlap function. The parameters from the analytical calculation are used for the forward iterative algorithm to represent the measurement geometry of the Raman lidar MARTHA.

	Ray-tracing Simulation		Analytical Calculation	
FOV	0.5 mrad	0.78 mrad	0.5 mrad	0.78 mrad
Divergence of laser beam	0.2 mrad		0.21 mrad	
Tilt of laser beam	0.115 mrad	0.205 mrad	0.1 mrad	0.19 mrad

to represent the measurement geometry in the forward iterative algorithm. The radii of the telescope's mirrors and the laser beam, the effective focal length of the telescope, as well as the distance between the focal plane of the telescope and the mirror diaphragm are set as listed in Table 5.2. In the ray-tracing simulation and the analytical calculation the edge of the laser beam (cut-off intensity) is treated differently. Thus the the tilt and divergence of the laser beam were slightly varied for the analytical calculation in the intervals of ± 0.03 mrad from the corresponding values used for the ray-tracing simulation. Table 5.3 shows the tilt and divergence for the analytical calculation and ray-tracing simulation that yield the best match of the overlap functions. The small deviations between the analytically calculated overlap functions and the functions obtained from measurements and ray-tracing simulations (cf. Fig. 5.8) confirm that the dual-FOV Raman lidar measurement geometry of MARTHA is well represented in the forward iterative algorithm, which is mandatory for high-quality cloud analyses.

5.4 Retrieval of liquid-water content

The forward iterative algorithm retrieves profiles of the effective droplet radius r_e and the extinction coefficient α of clouds. These two quantities together with the water density $\rho = 1\,\mathrm{g/cm^3}$ can be used to calculate profiles of the LWC w_c, which is another important cloud microphysical property:

$$w_\mathrm{c}(z) = \frac{2}{3}\rho r_\mathrm{e}(z)\alpha. \tag{5.6}$$

This equation is derived from the expression for the extinction coefficient α of a cloud,

$$\alpha = \int_0^\infty n(r) Q_\mathrm{ext}(x, m)\pi r^2 \mathrm{d}r, \tag{5.7}$$

with the droplet size distribution $n(r)$, droplet radius r, and the extinction efficiency Q_ext being dependent on the size parameter $x = \frac{2\pi r}{\lambda}$ with the laser wavelength λ and the refractive index m. As the investigated cloud droplets are much larger than the laser wavelength, the approximation $Q_\mathrm{ext} \approx 2$ can be applied. Substituting

$$\int_0^\infty n(r) r^2 \mathrm{d}r = \int_0^\infty n(r) r^3 \mathrm{d}r \frac{1}{r_\mathrm{e}} \tag{5.8}$$

and

$$w_\mathrm{c} = \frac{4\pi}{3}\rho \int_0^\infty n(r) r^3 \mathrm{d}r \tag{5.9}$$

leads to Eq. (5.6).

5.5 Retrieval of cloud droplet number concentration

As explained in Subsection 2.2.3, the CDNC is an important cloud microphysical quantity because it is a convenient proxy for cloud properties in investigations of aerosol-cloud relationships. The CDNC N can be derived from

$$N = \frac{\alpha}{2\pi r_\mathrm{s}^2}, \tag{5.10}$$

with the surface mean droplet radius $r_\mathrm{s} = (\overline{r^2})^{1/2}$. However, the surface mean droplet radius cannot be assessed with dual-FOV Raman lidar measurements directly and thus has to be derived from the effective radius. The relationship between these two quantities depends on the cloud droplet size distribution. Gamma distributions adequately model many droplet size distributions obtained from in-situ measurements [*Miles et al.*, 2000], and their usage in cloud models is common [*Cohard and Pinty*, 2000; *Khairoutdinov and Kogan*, 2000; *Liu and Daum*, 2004]. Furthermore, gamma distributions are frequently employed in radiative-transfer studies of scattering media [*Deirmendjian*, 1969]. The modified gamma distribution is defined as

$$n(r) = \frac{N}{\Gamma(p)} r^{p-1} b^p \exp(-br), \tag{5.11}$$

with the parameters $b, p > 0$. For droplet size distributions that comply with a gamma distribution the surface mean radius is related to the effective radius by

$$r_{\mathrm{s}}^2 = \frac{p(p+1)}{(p+2)^2} r_{\mathrm{e}}^2 = l r_{\mathrm{e}}^2, \tag{5.12}$$

with the factor $l = \frac{p(p+1)}{(p+2)^2}$. Thus, the CDNC of a cloud with a droplet size distribution that meets a gamma distribution can be calculated to

$$N = \frac{\alpha}{2\pi l r_{\mathrm{e}}^2} \tag{5.13}$$

as a combination of Eq. (5.10) and (5.12).

Miles et al. [2000] set up a database from various in-situ measurements of droplet size distributions of low-level stratus clouds. The fit of a modified gamma distribution to the size distributions obtained from measurements in continental air masses yielded $p = 8.7 \pm 6.3$ and thus $l = 0.74 \pm 0.20$.

The work of *Martin et al.* [1994] permits an alternative approach. A linear relationship between the volume mean radius $r_{\mathrm{v}} = (\overline{r^3})^{1/3}$ to the power of three and the effective radius to the power of three,

$$r_{\mathrm{v}}^3 = k r_{\mathrm{e}}^3, \tag{5.14}$$

was established from a number of in-situ measurements of warm stratocumulus clouds (i.e., clouds above 0°C) with negligible entrainment effects. For continental air masses it was found that $k = 0.67 \pm 0.07$. *Lu and Seinfeld* [2006] compiled a list of k values from stratiform clouds. The values for continental air masses range from 0.67 to 0.9. With the relationship

$$N = \frac{3 w_{\mathrm{c}}}{4\pi\rho r_{\mathrm{v}}^3} \tag{5.15}$$

and Eq. (5.6) and (5.14) the CDNC can be calculated to

$$N = \frac{\alpha}{2\pi k r_{\mathrm{e}}^2}, \tag{5.16}$$

which has the identical structure as Eq. (5.13). The k values are slightly larger than the l values and have a larger uncertainty. Still, the two approaches can be considered as consistent. As the dataset of *Miles et al.* [2000] is larger than the dataset of *Lu and Seinfeld* [2006], Eq. (5.13) was used to derive CDNC profiles in this work.

5.6 Retrieval of cloud base height

When using lidar, typically the profile of the backscatter coefficient is utilized for the determination of the cloud base height. However, the backscatter coefficient increases already below the cloud due to the growth of aerosol particles in the humid environment, which complicates the corresponding retrievals. Dual-FOV lidar measurements provide another approach to retrieve cloud base height because multiple scattering by cloud droplets leads

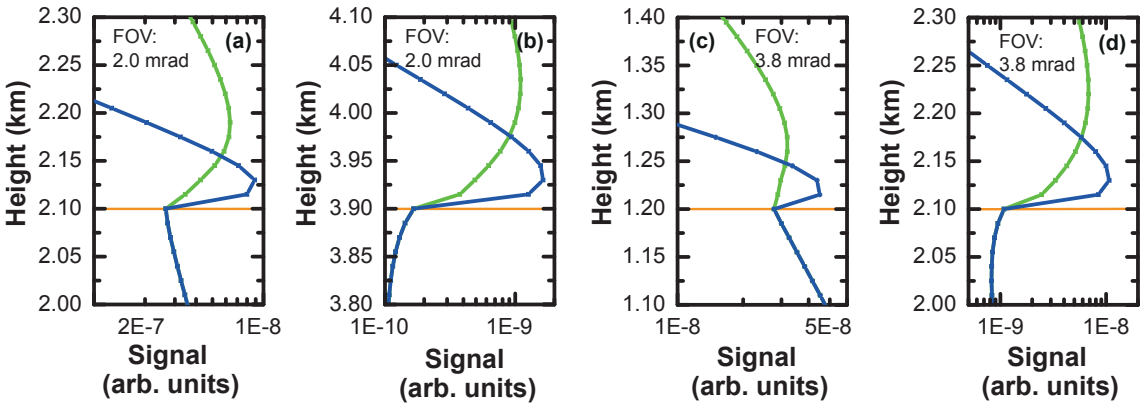

Figure 5.9: Simulated Raman signals from the outer FOV of (a), (b) 2.0 and (c), (d) 3.8 mrad for clouds with droplet effective radii of 8 and 3 µm and extinction coefficients of 5 and 20 km^{-1} in green and blue, respectively. The cloud base is indicated by an orange line. All simulations show a signal increase at cloud base. For some simulations the aerosol particles below cloud base cause a signal increase. However, this signal increase is much weaker than the increase at cloud base.

to an increase of the Raman signal from the outer FOV. Still, the signal depends on the measurement geometry as well, particularly the FOV and cloud base height.

The behavior of the Raman signal from the outer FOV was investigated with simulations based on the work of *Malinka and Zege* [2003]. Fig. 5.9 presents the results of this investigation. Simulated Raman signals are shown from the outer FOV of 2.0 and 3.8 mrad for several cloud base heights in the corresponding altitude range suitable for cloud measurements [*Schmidt et al.*, 2013]. For the simulation cloud droplet effective radii of 8 and 3 µm and cloud extinction coefficients of 5 and 20 km^{-1}, were assumed, which correspond to the range of microphysical cloud properties derived at the cloud bases in the measurements analyzed in the present work.

In the simulations the growth of aerosol particles due to an increased humidity was considered. The resulting increase of the scattering cross section was calculated as described in *Hänel* [1976] and *Randriamiarisoa et al.* [2006]. The gamma parameter, describing the magnitude of this increase, was set to 0.5, which is a common value [*Gasso et al.*, 2000; *Randriamiarisoa et al.*, 2006; *Skupin*, 2013]. An increase of the relative humidity from 65% at 1 km below cloud base to 98% at 15 m below cloud base was considered.

In all of the simulations shown in Fig. 5.9 the Raman signal from the outer FOV increases at cloud base. The slope of the increase differs strongly with the measurement geometry and cloud properties. Furthermore, the aerosol growth below cloud base leads to a signal increase for some measurement geometries. However, in all presented cases the cloud base height can be identified from the strong increase of the derivative of the Raman signal from the outer FOV exactly at cloud base. Thus, for all relevant altitudes of dual-FOV measurements the cloud base height can be retrieved with the accuracy of the measurement's height resolution (15 m for MARTHA), which is another unique feature of the dual-FOV lidar.

5.7 Scheme for analysis of dual-FOV measurements

This section describes the pre- and post-processing of the data for the forward iterative algorithm as well as the settings for running the cloud forward iterations. Before May 2012 the signals of the inner and outer FOV were recorded with different height resolutions due to the usage of different data acquisition systems (cf. Subsection 5.2.2). Thus, the signal from the outer FOV, recorded with the Licel transient recorder at a height resolution of 7.5 m, was averaged to a height resolution of 15 m which corresponds to the height resolution of the Purana system. With the installation of the CNT80 data acquisition system instead of the Purana system, the detection channels of the inner as well as of the outer FOV worked with the same height resolution of 7.5 m, which is used in the data analysis.

The cloud base height often varies within a time span of several seconds to minutes by 10 to 100 m. Averaging profiles with different cloud base heights would result in inaccurately retrieved cloud microphysical properties, especially at the cloud base where cloud-free and cloud-containing signals would be averaged. Therefore, for each of the 4-s profiles the height of the cloud base is determined from the derivative of the signal from the outer FOV at 607 nm (cf. Section 5.6). For the averaging only profiles are considered for which the cloud base does not differ by more than 30 m.

For the analysis of a cloud measurement the cloud forward iterations are performed with height resolutions of four, five, six, and seven layers as well as an automatically determined height resolution. Forward iterations with more than seven height layers often show oszillations in the retrieved results, indicating that the obtained solutions are not stable.

In the following, the choice of the lower and upper height limit for the execution of the forward iterative algorithm is explained. The lower height limit is set to the cloud base height, which is retrieved with the Raman signal measured in the outer FOV, as described in Section 5.6. To account for uncertainties in the retrieved cloud base height, due to its temporal variations, the lower height limit is varied by 30 m in steps of 15 m. In case of complete penetration of the cloud, the upper height limit is set to the cloud top height, which is derived from the elastic-backscatter signal of the inner FOV. However, due to the weak signals in that altitude the accuracy is limited. Furthermore, the variations of the cloud top height even exceed the variability at cloud base. In the much more common case of complete attenuation of at least one of the two Raman signals measured in the inner and outer FOV, the upper height limit of the forward iteration is set to the altitude where the first Raman signal is completely attenuated. However, the measured lidar signals close to that height limit are usually very weak and thus the forward iteration might not run successfully. Hence, in both cases, the penetration of the cloud or the complete attenuation of at least one Raman signal, the derived upper height limit for the forward iteration has to be varied. This is done by 45 to 90 m towards lower altitudes in steps of 15 m. Hence, for each height resolution the algorithm is executed with a variety of lower and upper height limits.

The measurement error of the lidar signals used for the forward iteration is considered by input variation, using Monte Carlo simulations. Thus, for a forward iteration run the algorithm is executed 14 times with count rates c being varied within the range $[c-\sqrt{c}, c+\sqrt{c}]$

for each height bin, according to the standard deviation of a Poisson distribution. These variations are done with the height resolution of the signals used in the forward iteration, i.e., 15 and 7.5 m before and after May 2012, respectively (cf. Subsection 3.1). The results of the corresponding forward iterations are used to compute for each cloud layer the mean value and its error from the standard deviation, yielding profiles of the effective radius, the extinction coefficient, and the corresponding error margins.

According to the five different height resolutions (number of layers) used for the forward iteration runs as well as the three and four to seven different altitudes for the lower and upper height limits, respectively, a total of 60 to 105 forward iterative runs are performed for the analysis of a cloud measurement. The obtained profiles of cloud microphysical properties are checked for their quality. Profiles with a data point having a relative error of more than 60% are excluded as well profiles for which the average error of two consecutive data points exceeds 45% and profiles for which the average relative error of all data points exceeds 30%. Furthermore, profiles that are physically unrealistic are discarded. Thus, profiles with effective radii greater than 30 µm are rejected as well as profiles that show oscillations. Moreover, profiles that show a strong difference between two consecutive data points are excluded. These profiles are defined as profiles with a data point that has a relative difference to its neighboring points of larger than 500%. On average, 30% to 85% of the forward iterative results are accepted. These profiles are averaged to a common height resolution which corresponds to the lowest height resolution leading to successful cloud forward iterations. The resulting profiles are averaged with a weight according to the calculated statistical error from the input variation. The standard deviation of these data points in each height bin is considered as the error of the corresponding mean.

Chapter 6

Measurement example, error analysis, and evaluation

An example of a dual-FOV Raman lidar measurement is introduced in this chapter. The measurement as well as the retrieved cloud properties are presented in the first section. An MWR was employed to verify the measured LWP which is shown in this section as well. In Section 6.2 extensive error analyses of the retrieved results and the methods employed in the retrieval are performed. The chapter closes with Section 6.3, where the dual-FOV Raman lidar technique is evaluated regarding its capabilities for investigations of aerosol-cloud interactions. These discussions are based on the explanations given in Section 2.2. Parts of this chapter have been published in *Schmidt et al.* [2014] and *Schmidt et al.* [2013] and are adopted without explicit citing.

6.1 Measurement of an altocumulus cloud

6.1.1 Overview

Fig. 6.1 shows the time-height cross section of the range-corrected lidar signal at 532 nm from the inner FOV, obtained during a dual-FOV Raman lidar measurement on 5 September 2011. Aerosol layers are indicated by yellowish colors. The measured cloud is shown in red colors.

For the cloud retrieval 132 profiles were summarized excluding profiles where cloud gaps or variations of the cloud base of more than 30 m occurred, as explained in Section 5.7. The Raman signals at 607 nm measured in the inner and outer FOV are shown in Fig. 6.2. The figure shows that the corresponding signals calculated with the forward iterative algorithm compare well with the measured signals.

The Raman signal measured in the outer FOV indicates a cloud base height of 2.92 km, which is highlighted in Fig. 6.2. This figure shows an increase of the signal at 532 nm from the inner FOV already about 50 m below that altitude. This increase can be explained with aerosol growth below the cloud due to the increased humidity, which is discussed in

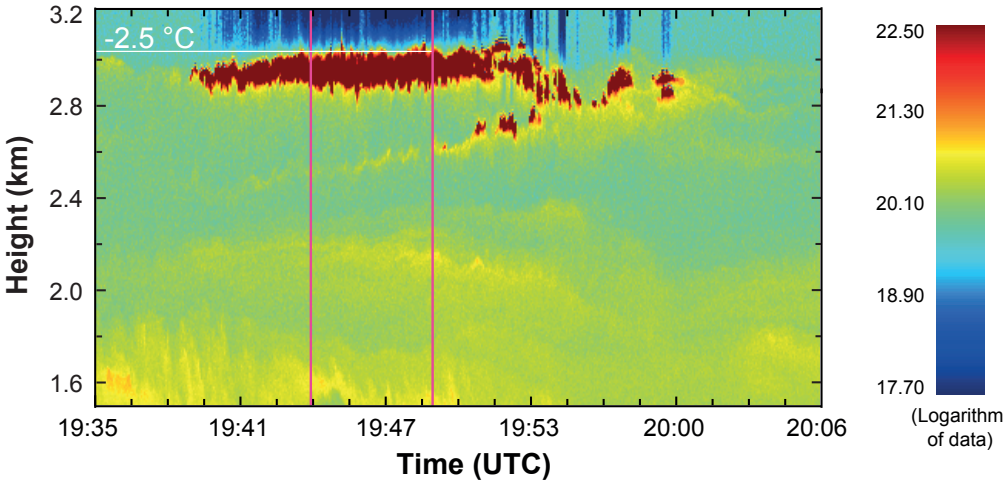

Figure 6.1: Time-height cross section of the range-corrected lidar signal at 532 nm, inner FOV. The time period used for the cloud forward iteration is indicated by pink lines. Profiles with cloud gaps, indicated by light blue colors above the cloud layer, were not used for the forward iteration. The cloud top temperatures derived from the GDAS temperature profile for grid point Leipzig at 21:00 UTC on 5 September 2011, is inscribed in white color.

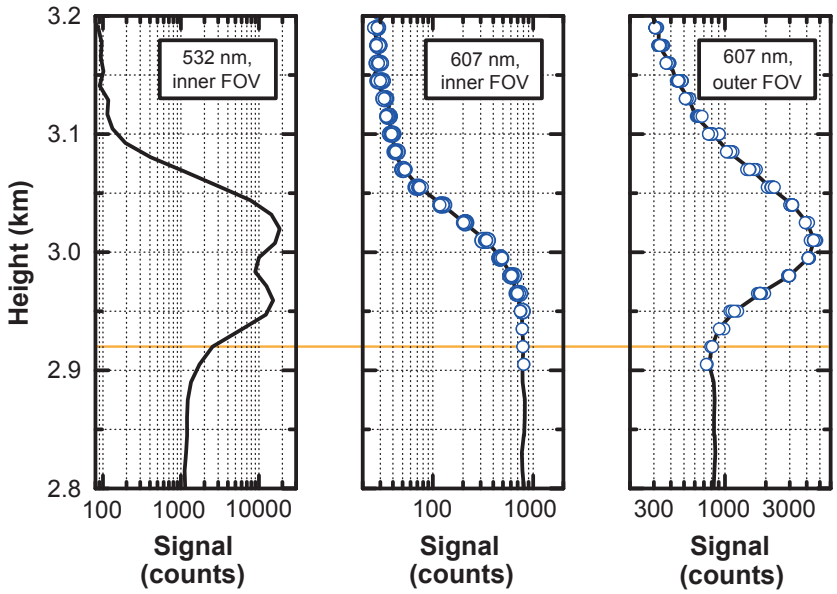

Figure 6.2: Measured signals from the inner FOV at 532 and 607 nm and outer FOV at 607 nm. In the plots for the inelastic signals the signals simulated from the forward iterative algorithm are shown as blue circles. The cloud base height, derived from the signal at 607 nm from the outer FOV, is shown as an orange line. The profile of the elastic signalis affected by dead-time effects due to the high count rates inside the cloud. The Raman signals are not dead-time affected because of a good neutral-density filter setting.

detail in Subsection 6.1.4. The 532-nm signal from the inner FOV indicates the cloud top at approximately 3.1 km.

The elastic backscatter lidar signal is influenced by detector saturation (dead-time effects) [*Donovan et al.*, 1993] because of the high count rates inside the cloud. Hence, Fig. 6.2 shows a signal decrease at 532 nm inside the cloud. Because of a good setting of the neutral-density filters, the Raman signals are not dead-time affected which is important for reliable results from the forward iterative algorithm.

6.1.2 Cloud microphysical properties

Figure 6.3 presents the cloud microphysical properties obtained from the dual-FOV Raman lidar measurement. As described in Section 5.3, the forward iterative algorithm considers the cloud to consist of a number of homogeneous cloud layers, and the microphysical properties obtained for the various layers yield the profiles of the obtained quantities. Hence, for a correct representation of the retrieval results, the display of step functions for the retrieved quantities would be appropriate. Nevertheless, to attain more clearly arranged plots, especially for comparisons of several cloud property profiles, the retrieval results of the various layers are connected with straight lines in this figure and all following figured presenting results from dual-FOV Raman lidar measurements.

On the left side of Fig. 6.3 the extinction coefficient of the cloud is displayed. The profile retrieved with the forward iterative algorithm is compared with the extinction coefficient obtained from the conventional Raman method not considering multiple scattering (cf. Subsection 4.2.3, *Ansmann et al.* [1990]). The extinction coefficient from the forward iterative algorithm exceeds the extinction coefficient calculated with the Raman method as expected because of the multiple-scattering effect. Light that is forward scattered under small angles remains in the inner FOV and is backscattered to the lidar instead of getting lost.

The second plot from left shows the profile of the effective cloud droplet radius. Over the largest part of the cloud the effective radius increases with penetration depth. This can be explained with the further condensation of water vapor due to the cooling of the ascending air parcel. The increase of the LWC, shown next to this plot, is caused by the same process. The top of the uppermost cloud layer from the retrieval algorithm is at 3.075 km, which is almost the estimated cloud top height of 3.1 km. Hence, the decrease of the effective droplet radius and LWC at larger penetration depths can be explained with the downmixing of dry air from above the cloud leading to the evaporation of some liquid water. The right panel shows the profile of the CDNC. Its error is calculated according to Gaussian error propagation from the errors of the extinction coefficient and cloud droplet radius (c.f. Eq. (5.13)), as done for the errors of the LWC. The two lowest data points have large errors due to the corresponding errors of the extinction coefficient and effective radius. The decrease of CDNC above penetration depths of 55 m can be explained with coagulation of cloud droplets. At penetration depths between 30 and 140 m, which correspond to the inner part of the cloud, the effective radius is between 4 and 16 µm. The LWC has values between 0.02 and 0.35 g/m^3, and the CDNC ranges between 30 and 210 cm^{-3} in this altitude. These

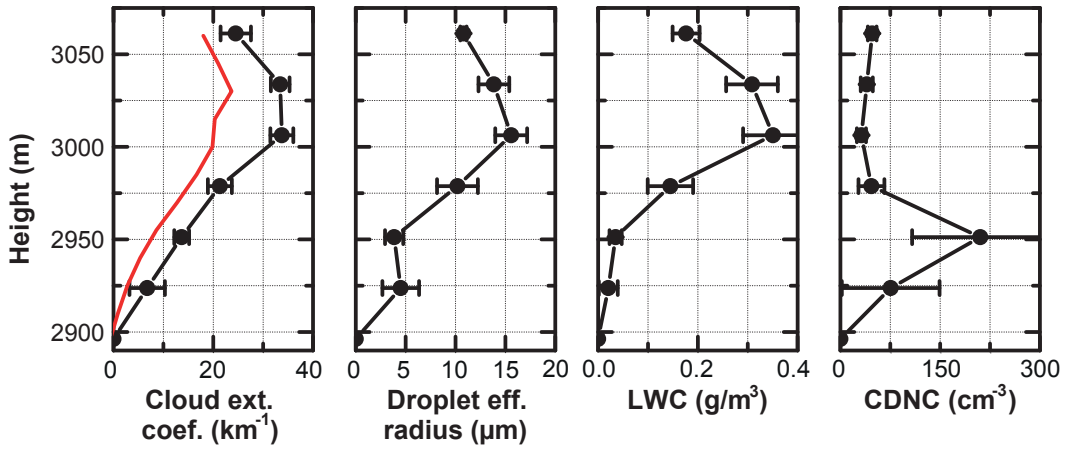

Figure 6.3: Extinction coefficient, efective droplet radius, LWC, and CDNC of the cloud probed on 5 September 2011, 19:44–19:49 UTC, retrieved with the forward iterative algorithm. The retrieved cloud extinction coefficient (black) is compared with the extinction coefficient calculated with the Raman method not considering multiple scattering (red line).

values fit to results from in-situ measurements compiled by *Miles et al.* [2000]. Furthermore, *Lu et al.* [2007] derived from in-situ measurements of marine stratocumulus clouds droplet effective radii of 5.6 to 9.3 µm for clouds with LWPs from 15 to 45 g/m^2, which corresponds to the LWP of the observed cloud (cf. Subsection 6.1.3). The obtained CDNCs range from 43 to 290 cm^{-3}. During the VOCALS-REx (VAMOS Ocean-Cloud-Atmosphere-Land Study Regional Experimemt) field study over the southeastern Pacific west of South America in October and November 2008, typical CDNC values in the strotocumulus-topped marine boundary layer were mostly in the range from 50 to 350 cm^{-3} [*Kleinman et al.*, 2012; *Twohy et al.*, 2013] and droplet effective radii were mostly 4 to 12 µm [*Twohy et al.*, 2005].

6.1.3 Verification: Comparison of LWP with MWR measurement

The MWR which is part of LACROS (cf. Section 3.3) was used for a verification of the forward iterative results. The LWP measured with the MWR was compared with the LWP calculated from the LWC obtained from the dual-FOV Raman lidar measurement. As mentioned in Subsection 6.1.2 the top height of the uppermost cloud layer from the retrieval algorithm and the cloud top height estimated from the 532-nm signal from the inner FOV are in good agreement. This match ensure a reasonable comparison between the integral of the profile information derived with the dual-FOV Raman lidar probing and the non-height-resolved LWP measurement of the MWR.

Fig. 6.4 shows the LWP obtained from the MWR during the time period used for the forward iteration as well as its average and the LWP from the dual-FOV measurement. The average LWP measured with the MWR is 33.2 ± 3.1 g/m^2. This value matches the LWP of 28.5 ± 5.9 g/m^2 from the dual-FOV measurement. A reason for the slightly smaller LWP from the forward iteration might be that possibly the cloud was not completely penetrated with the

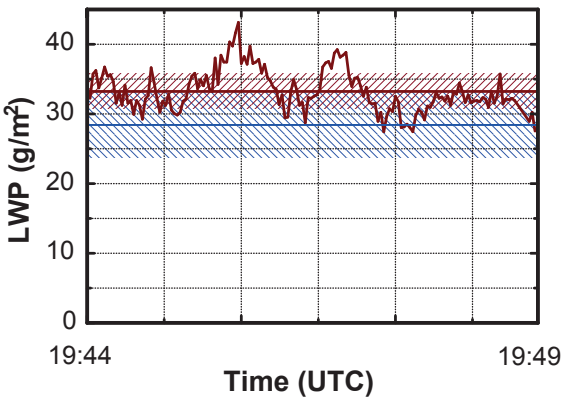

Figure 6.4: LWP from MWR measurement and and its average (red) compared to the LWP calculated from the LWC from the forward iteration (blue). The error bars of the average values are indicated by the hatched areas.

dual-FOV measurement, at least not all the time. Furthermore, the measurement geometry might cause deviations: an MWR probes a much larger volume than the comparably narrow FOV of a lidar.

6.1.4 Aerosol particle growth and derivation of cloud base height

The increase of the backscatter coefficient due to the growth of aerosol particles in a humid environment was investigated in detail for this measurement. Fig. 6.5 shows the signal measured in the outer FOV at 607 nm during the time span used for the cloud analysis for the 500 m below the cloud. Furthermore, this figure presents the profile of the backscatter coefficient obtained from the Raman lidar measurement (cf. Subsection 4.2.2, *Ansmann et al.* [1992a]) in this time period.

The increase of the measured backscatter coefficient due to increasing humidity is compared with the increase expected from theory, displayed in Fig. 6.5 as well. For the calculation of the expected increase of the backscatter coefficient, the profile of the water-vapor mixing ratio was derived from the Raman lidar measurement [*Mattis et al.*, 2002] in the time period used to derive the cloud properties and the aerosol particle backscatter coefficient. For the calibration, the integrated water-vapor content, measured in the cloud-free period from 20:04 to 20:16 UTC with the MWR was used. From the resulting profile and the GDAS profile of the temperature for grid point Leipzig at 21:00 UTC on 5 September 2011, the profile of the relative humidity was calculated. At 2.4 km altitude a relative humidity of 77% was derived. The retrieved profile of the backscatter coefficient increases monotonically from this altitude onwards. Thus, the corresponding relative humidity was estimated for the respective altitude with the assumption of a linear increase up to 100% at cloud base. The resulting particle growth and increase of the backscatter coefficient were calculated according to *Hänel*

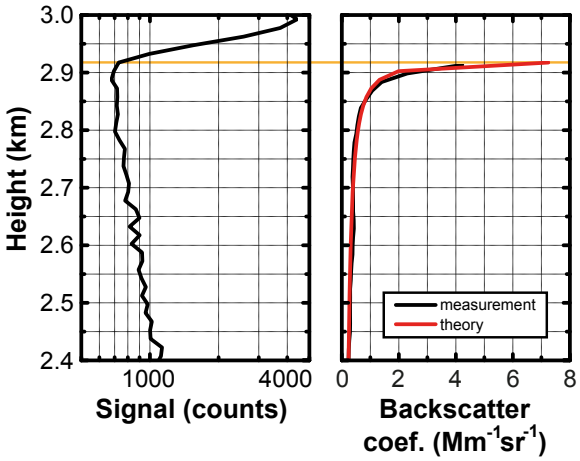

Figure 6.5: Left: signal from outer FOV at 607 nm measured on 5 September 2011, 19:44–19:49 UTC. The cloud base height, which was determined from this measured signal, is highlighted in orange. Right: measured and calculated profiles of the backscatter coefficient for the corresponding time period. Both signals agree and illustrate the particle growth due to increasing humidity below cloud base. The backscatter coefficient increases by a factor of about 16 from the altitude of 2.4 km with a relative humidity of 77% to the height of 2.9 km with a relative humidity of 99%.

[1976] and *Randriamiarisoa et al.* [2006] with a gamma value of 0.58, which is in the range of realistic values for aerosol particles over Leipzig [*Skupin*, 2013].

The measured and calculated profiles agree well, showing an increase of the backscatter coefficient from 0.24 Mm^{-1} at 2.4 km altitude with a relative humidity of 77% by a factor of 16 to about 4 Mm^{-1} at 2.9 km altitude with a relative humidity of 99%. A significant increase of the backscatter coefficient occurs already 100 m below cloud base. This increase illustrates the uncertainty involved in the determination of the cloud base height from the profile of the backscatter coefficient, which can be overcome by dual-FOV measurements because they always provide robust information on the cloud base height. However, it has to be mentioned that the time period for the cloud analysis has to be chosen such that fluctuations of the cloud base height are minimized to obtain well utilizable dual-FOV signals.

6.2 Error analysis

This section deals with the accuracy and quality of the results retrieved from forward iterations. In the first two subsections an error analysis is done on the base of the dual-FOV Raman lidar measurement presented in the previous section. Thus, in Subsection 6.2.1 the statistical error derived through the averaging of iteration results with differently set cloud boundaries and height resolutions is compared to the error obtained from the variation of the lidar signals as the input of the forward iteration. Subsection 6.2.2 investigates the influence of the measurement geometry, set in the forward iterative algorithm, on the retrieved results. In the following subsections error analyses are performed on a statistical basis. The minimal

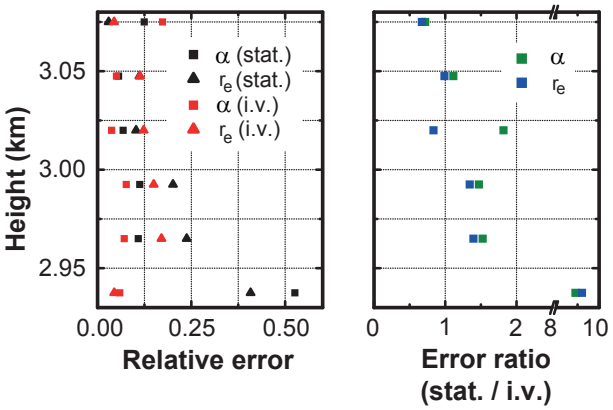

Figure 6.6: Left: relative errors of the forward iterative results presented in Fig. 6.3. Black symbols denote statistical errors (stat.), red symbols show the averaged errors obtained from input variations (i.v.). Squares indicate errors of the extinction coefficient α. The errors of the effective radius r_e are displayed by triangles. Right: ratio of the statistical errors to the errors from input variation of the extinction coefficient α (green) and effective radius r_e (blue). For the lowest penetration depth the statistical errors dominate. For greater penetration depth both errors have the same magnitude with the statistical error often being slightly larger.

duration of a dual-FOV cloud measurement which is necessary to obtain successful forward iteration runs is determined from 49 forward iterations in Subsection 6.2.3. The mean errors of the cloud microphysical properties derived from all dual-FOV Raman lidar measurements analyzed in this work (29 measurements) are evaluated and compared in Subsection 6.2.4. Subsection 6.2.5 has a closer look on the uncertainties of the CDNC.

6.2.1 Error from averaging over different forward iterative runs and input variation

As explained in Section 5.7, the stated errors of the retrieved mircophysical properties are statistical errors, obtained from the standard deviations from the averaging of the forward iteration results from differently set cloud boundaries and height resolutions in the forward iterative algorithm. Here, these errors are compared to the errors obtained through input variation of the utilized lidar signals of the inner and outer FOV. Figure 6.6 shows the relative statistical errors of the forward iteration results presented in Fig. 6.3 as well as the relative errors obtained from input variation averaged over all successful forward iterative runs. The relative statistical errors are largest at the cloud base with values of 0.41 and 0.53 for the effective radius and the extinction coefficient, respectively. These uncertainties are due to variations of the cloud base height. On the one hand, variations of the cloud base height of up to 30 m occur in the profiles chosen for the cloud analysis. On the other hand, consequently, the cloud base heights of the forward itertive runs are varied by 30 m (cf. Section 5.7). Both effects contribute to the high errors directly at cloud base. At larger penetration depths the corresponding relative errors are below 0.25.

At the lowest penetration depth the statistical errors are about nine times larger than the errors from input variation. The ratio of the relative statistical error to the relative error from input variation is much lower for the other penetration depths, as illustrated in Fig. 6.6. Still, for most penetration depths the statistical error is slightly larger than the error from input variation. Thus, the statistical error is considered as a reasonable measure for the uncertainty of the retrieved cloud microphysical properties.

6.2.2 Effects of uncertainties of measurement geometry on results of forward iteration

In Section 5.3 it was demonstrated that the dual-FOV measurement geometry of MARTHA is well represented in the forward iterative algorithm. In this section, the uncertainties of the most crucial parameters controlling the measurement geometry are evaluated. These parameters are the tilt and the divergence of the laser beam as they have the strongest influence on the overlap function and are most difficult to determine. The parameters were varied as listed in Table 6.1 in order to obtain two overlap functions with opposite deviations from the overlap function that represents the measurement geometry best. The overlap function for the employed measurement geometry and the two overlap functions for the varied measurement geometries were calculated analytically as explained in Section 5.3 and are shown in Fig. 6.7. The chosen parameters lead to deviations of the overlap functions that are considerably larger than the deviations between the overlap functions in Fig. 5.8 which characterize the uncertainties of the employed measurement geometries. Hence, the utilization of these parameters in the forward iterative algorithm provides an expedient estimation of the maximum possible error due to uncertainties of the measurement geometry.

Table 6.1: Variations of tilt and divergence of laser beam for ray-tracing simulations for investigation of sensitivity of the forward iterative algorithm towards the measurement geometry.

Parameter	Setup Used for Forward Iteration	Variation A	Variation B
Tilt	0.10 mrad	0.12 mrad	0.07 mrad
Divergence	0.21 mrad	0.26 mrad	0.18 mrad

The three measurement geometries were used in the forward iterative algorithm to analyse the measurement presented in Section 6.1. The obtained cloud microphysical properties are presented in Fig. 6.8, which shows that the deviations between the results from different measurement geometries are smaller than the corresponding errors. The mean deviation of the two forward iteration results with the varied measurement geometry to the results obtained with the original measurement geometry was calculated and averaged over height. Its value is compared with the height-averaged error of the corresponding cloud microphysical property, derived as described in Section 5.7. For the extinction coefficient the ratio of the derivation to the errors is 0.29. The corresponding values for the effective radius, LWC, and

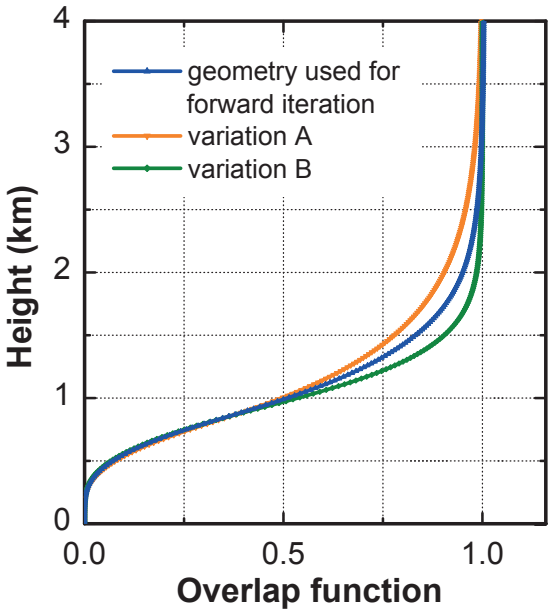

Figure 6.7: Overlap functions for a FOV of 0.5 mrad and for the measurement geometry usually used in the forward iteration (blue) as well as slightly modified measurement geometries listed in Table 6.1 (orange and green).

CDNC are 0.37, 0.32, and 0.31, respectively. This finding illustrates that the results of the forward iterative algorithm are dominated by the cloud microphysical properties and the measurement geometry causes only minor uncertainties of the results.

6.2.3 Required averaging time for forward iteration

Due to the signal noise several measured dual-FOV profiles have to be summed to obtain profiles suitable for running the forward iterative algorithm. The usage of weak, noisy signals results in forward iterations that do not run successfully. In this section the neccessary measurement time for dual-FOV cloud studies is examined. Different time periods for summation of measured dual-FOV profiles were utilzed to check for successful runs of the forward iterative algorithm. To obtain representative results, this analysis was performed with four different dual-FOV cloud measurements, which are listed in Table 6.2. Altogether 49 forward iterations with summation time periods between 4 s and 22 min were run. The height resolution of the forward iterative algorithm was set automatically by the algorithm. Additionally, the algorithm was run with height resolutions of four and seven layers as well.

The signal-to-noise ratio of the summed signal depends not only on the measurement time but on the signal strength of the single profiles as well. To avoid an effect of a different signal strength due to different cloud heights, cloud microphysical properties, and neutral-density filter settings on the analysis, the study examines the success of the forward iterations regarding the signal strength of the summed signal. The success of the forward iterations

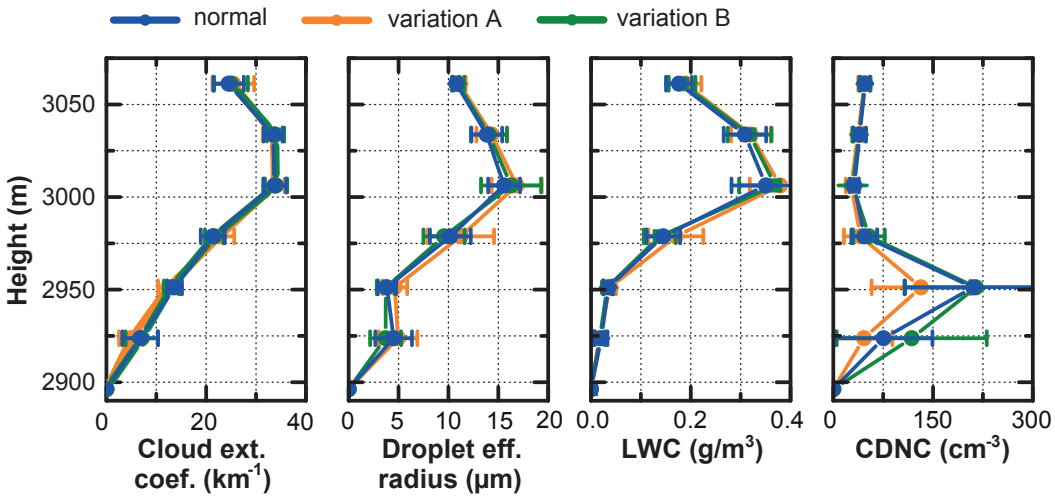

Figure 6.8: Cloud microphysical properties retrieved with the measurement geometry being generally used for forward iterations (blue) as well as the varied measurement geometries listed in Table 6.1 (orange and green).

Table 6.2: Measurements analyzed for study of necessary averaging time of dual-FOV measurements.

Date Of Measurement	Shortest Averaging Time	Longest Averaging Time	Number Of Forward Iterations
09-08-2010	20 s	5 min	20
20-09-2010	10 s	7 min	7
15-08-2011	8 s	14 min	11
30-08-2011	4 s	5 min	11

is checked in dependence of the sum of the signals from the inner and outer FOVs because the success of a forward iteration depends on the signal quality in the inner as well as in the outer FOV. The sum of the signals is considered below the cloud. Thus, single-scattering signals are evaluated. These signals are a measure for the signal strength inside the cloud without being affected by the cloud properties. The signal strength at the cloud base is considered as suitable for running the forward iterative algorithm, if more than 25% of the forward iterations with the corresponding variations of cloud base and top height as well as height resolution produce successful runs. For less than 5% successful forward iterations the signal strength is considered as not suitable. Measurements which do not fall in either of these categories are designated as ambiguous.

Fig. 6.9 displays the results of the study. All measurements with more than 1100 counts below the cloud base were suitable for running the forward iterative algorithm. Below 80 counts no measurement could be used for a forward iteration. As a threshold for obtaining

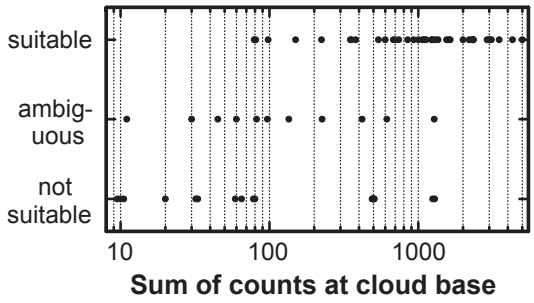

Figure 6.9: Suitability of dual-FOV measurements for forward iteration in dependence of signal strength at the cloud base. The signal strength is represented by the sum of both FOV's count rates at the cloud base.

a suitable dual-FOV measurement 700 counts appears to be reasonable as the vast majority of the measurements exceeding this value turned out to be suitable for running the forward iteration. The performed dual-FOV measurements had a neutral-density filter setting which induced count rates of about 1 Mc/s directly below the cloud base in the detection channel for the outer as well as the inner FOV. With this signal strength a measurement time of about two minutes is required to detect 700 counts at the cloud base in both FOVs. Assuming that due to the variation of the cloud base height about every third measured profile has to be rejected, the required measurement time for running the forward iterative algorithm is about three minutes.

6.2.4 Uncertainties of retrieved cloud microphysical properties

In this subsection the quality of the retrieved cloud microphysical properties is evaluated through the comparison of their uncertainties. For this objective the errors of cloud microphysical properties from 29 dual-FOV Raman lidar cloud measurements performed in the scope of the present work were averaged and compared. To assess the height dependence of the errors, the comparison was performed in three height layers for cloud penetration depths of 0 to 30 m, 30 to 70 m, and 70 to 120 m. The height ranges were chosen such that solely the lowest range covers the penetration depth where the derived cloud microphysical properties may be influenced by possible variations of the cloud base height (cf. Section 5.7). The upper height limit of 120 m was chosen because for 72% of the performed forward iterations penetration depths larger than this value were achieved. Hence, this upper limit serves as a good compromise between a high penetration depth and a comprehensive dataset. Furthermore, the extent of each height range was increased by 10 m for each step. This choice partially compensates for the decrease of the signal-to-noise ratio of the measured lidar signals with increasing cloud penetration depth. The height ranges are identical to the height ranges used in Chapter 8 for the statistical analysis of aerosol-cloud relationships. Hence, the retrieved errors describe the uncertainties of the cloud properties utilized in that investigation. In

addition to the height-resolved comparisons of the errors of the derived cloud properties, the comparison was also performed for the mean values of the three height ranges.

Table 6.3 lists the corresponding results. In general, the relative errors are largest in the lowest height range from 0 to 30 m, which can be explained with variations of the cloud base height. Above the penetration depth of 30 m, the relative errors drop by 30% to 50%. The cloud extinction and droplet effective radius, which are directly obtained from the forward iterative algorithm, show the lowest uncertainties with cloud mean values of 22% and 23%, respectively. The cloud properties that are calculated from these values have larger relative errors, as their errors follow from Gaussian error propagation and thus the uncertainties of both cloud extinction and droplet effective radius contribute to the resulting errors. The uncertainty of the CDNC is particularly high with a height-averaged relative error which is almost a factor of two higher than the corresponding LWC error. The largest part of this error originates from the uncertainty of the cloud droplet effective radius because the square of the radius occurs in Eq. (5.13) for the calculation of the CDNC. The contribution of the error of the parameter l which is employed in the CDNC calculation according to Eq. (5.13) is discussed in the following subsection.

Table 6.3: Mean relative errors of cloud extinction coefficient α, droplet effective radius r_e, LWC, and CDNC for analyses of 29 dual-FOV Raman lidar cloud measurements.

Cloud Property	Penetration Depth 0–30 m	30–70 m	70–120 m	Average
α	0.34	0.17	0.14	0.22
r_e	0.32	0.21	0.14	0.23
LWC	0.48	0.27	0.21	0.32
CDNC	0.82	0.58	0.43	0.61

6.2.5 Effect of unknown cloud droplet size distribution on CDNC error

The derivation of the CDNC from the measured profiles of the cloud droplet effective radius and extinction coefficient is explained in Section 5.5. A parameter l, which depends on the cloud droplet size distribution, has to be assumed to calculate the droplet surface mean radius from the effective radius (cf. Eq. (5.12)). In this work a value of $l = 0.74 \pm 0.20$ is utilized, which was derived from an extensive dataset of in-situ measurements. The relative error of 0.27 does not only result from measurement uncertainties but also from variations of l itself due to different cloud droplet size distributions of different clouds. This subsection deals with the effect of the lack of knowledge of the cloud droplet size distribution on the overall uncertainty of the derived CDNCs.

Therefore, Table 6.4 compares the relative errors of the CDNC averaged from 29 dual-FOV Raman lidar cloud measurements calculated with Gaussian error propagation from the relative error of the cloud extinction coefficient and droplet effective radius and with as well

as without the uncertainty of the l parameter. This comparison is done for three different cloud penetration depths of 0 to 30 m, 30 to 70 m and 70 to 120 m as well as for the average of these three height ranges, similar to the study in Subsection 6.2.4.

Table 6.4: Mean relative errors of CDNC for analyses of 29 dual-FOV Raman lidar cloud measurements with and without consideration of the uncertainty of the l parameter, which describes the uncertainty of the derived CDNCs resulting from variations of the cloud droplet size distribution.

	Penetration Depth			
	0–30 m	30–70 m	70–120 m	Average
Δl not considered	0.77	0.50	0.35	0.54
Δl considered	0.81	0.58	0.43	0.61

The differences of the relative CDNC errors with and without the consideration of the uncertainty of the l parameter range from 5% to 19%. Hence, the l parameter constitutes only a minor contribution to the overall error of the CDNC. The small effect of the uncertainty of the l parameter on the CDNC error emphasizes the feasibility of the approach to derive the CDNC from the measured cloud extinction and droplet effective radius according to Eq. (5.13).

6.3 Evaluation of the dual-FOV Raman lidar technique

The investigation of aerosol-cloud interactions is a keystone of this thesis. Therefore, the following subsections evaluate the applied dual-FOV Raman lidar technique with respect to the suitability for investigations regarding aerosol-cloud relationships and compare it with other ground-based remote-sensing techiques for cloud probings.

6.3.1 Feasibility for investigations of aerosol-cloud interactions

Choice of observables for investigation of aerosol-cloud relationships

In Subsection 2.2.3 possible observables which suit as proxies for aerosol and cloud properties in the investigation of aerosol-cloud interactions were listed. Fig. 6.10 summarizes these observables with a color code indicating their suitability for approaches with the dual-FOV Raman lidar technique.

The capabilities of Raman lidar measurements to derive high-quality information about aerosol properties were explained in detail in Section 4.2. The aerosol particle extinction coefficient can be obtained without any a priori assumptions. In combination with the Ångström exponent, which can be derived from Raman lidar measurements as well, the aerosol index can be calculated. With the inversion technique described in Subsection 4.2.5 the APNC can be obtained from Raman lidar measurements. From these quantities, the

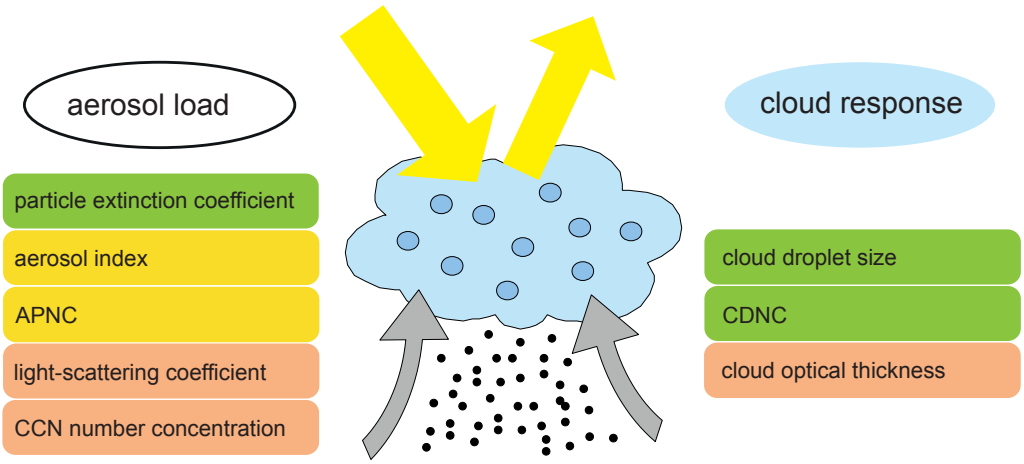

Figure 6.10: Possible observables for the examination of aerosol-cloud interactions. Green colors show observables which are easily accessible with dual-FOV Raman lidar measurements and are used for investigations of aerosol-cloud interactions presented in the following chapters. Observables which can be obtained from dual-FOV Raman lidar measurements with a much higher effort regarding data analysis are solely used in single case studies (APNC) or not used at all (aerosol index) and are highlighted with yellow color. Quantities which cannot be measured with a dual-FOV Raman lidar are shown in red color.

retrieval of the aerosol particle extinction coefficient is most simple. Therefore, the extinction coefficient is used to describe the aerosol load in the majority of the case studies presented in Chapter 7 as well as in the statistical approaches for the investigation of the aerosol-cloud interactions related to the Twomey effect, which are depicted in Chapter 8.

In Chapter 5 and in this chapter it was explained that the dual-FOV Raman lidar technique is capable of deriving profiles of the effective cloud droplet radius and CDNC. In contrast to the derivation of the effective droplet radius, which does not require any assumptions regarding cloud properties, the calculation of the CDNC needs an assumption of the relationship between the volume mean radius and the cloud droplet effective radius. This assumption leads to some additional uncertainty of the retrieved results, although it is based on a comprehensive statistics of in-situ cloud measurements (cf. Section 5.5). However, these uncertainties are small compared to the uncertainties which originate from the forward iterative algorithm which analyzes the dual-FOV Raman lidar measurements, as shown in Subsection 6.2.5. Therefore, the CDNC is an important proxy describing cloud properties in investigations of aerosol-cloud interactions. It has to be highlighted that the CDNC has no direct microphysical link to the LWC, which revokes the need to group measurements of aerosol and cloud properties according to LWC as necessary for analyses employing the effective radius as a proxy for cloud properties (cf. Subsection 2.2.3).

Because only a fraction of the probed warm clouds could be penetrated with the dual-FOV Raman lidar measurement, the cloud optical thickness can be derived only for those

clouds. As this restriction would constrain the available dataset needlessly, the cloud optical thickness is not used as a proxy for cloud properties in this thesis.

Suitability for objectives regarding investigations of aerosol-cloud interactions

In Subsection 2.2.2 the objectives of investigations related to aerosol-cloud interactions were distinguished between studies dealing with the detailed understanding and quantification of the microphysical processes involved in aerosol-cloud interactions (objective A) and studies focussing on the Twomey effect itself and the related radiative forcing (objective B). Investigations concerning the microphysical processes are mainly limited by the spatial resolution of the employed measurement technique. A horizontal resolution of at least 1 km should be achieved [*McComiskey and Feingold*, 2012]. As the required averaging time for a successful dual-FOV forward iteration is about 3 min (cf. Subsection 6.2.3), this demand is fulfilled for clouds moving with a moderate horizontal velocity of up to 5.5 m/s. The availability of Doppler lidar measurements to derive the vertical wind speed (cf. Section 3.2) as well as the advanced capabilities of multiwavelength Raman lidar measurements to derive a number of aerosol properties enable the use of the dual-FOV Raman lidar technique, embedded in the research platform LACROS, for studies towards objective A. The availability of profiles of the cloud droplet size and CDNC within the cloud constitutes an important advantage of this approach. Furthermore, the measurement of the LWC is of relevance as it allows the comparison of the obtained LWC profiles with LWC profiles assuming adiabatic conditions. Thus, the magnitude of entrainment can be assessed. This potential is of great interest as entrainment has a strong influence on the magnitude of aerosol-cloud interactions [*Kim et al.*, 2008].

In principle, objective B can be pursued as well because of the possibility of long-term measurements with the dual-FOV Raman lidar technique. However, the limited penetration depth of the dual-FOV Raman lidar technique is a drawback for this aim. For a cloud's effect on the earth's radiative budget, the upper cloud layers are more important than the cloud properties of the layers below, especially in the case of thick clouds. Still, thin clouds can be completely or almost completely penetrated with the dual-FOV Raman lidar technique and the contribution of a cloud parcel to the cloud's albedo is almost independent of its vertical position relative to cloud base and top [*Lacis and Hansen*, 1974; *Bohren*, 1987; *King*, 1987]. The fraction of these clouds, among the ice-free, non-precipitating clouds occurring over Leipzig during night time is extraordinarily high, which can be also seen from the overview of the measurements performed for this thesis [*TROPOS - LACROS*, 2013].

A further drawback of the dual-FOV Raman lidar technique is the restriction of the cloud measurements to night time. This constraint is especially severe for the pursuit of objective B – the investigation of the effect of clouds on earth's radiative budget through the scattering of sunlight. Nevertheless, regarding the currently poor understanding about aerosol-cloud interactions, also studies utilizing solely night time measurements are beneficial. These studies are expected to contribute to the understanding of aerosol-cloud interactions related to the Twomey effect as well, because the basic physical principles remain identical.

The confinement of the measurements to one single location is a hindrance for an overall understanding of aerosol-cloud interactions, particularly for the pursuit of objective B. However, the measurements are another step towards a better understanding of aerosol-cloud interactions. Furthermore, the investigations conducted in the scope of this work are a demonstration of the capabilities of this technique and might be a motivation to perform dual-FOV Raman lidar cloud probings also at other locations within a network approach.

As the dual-FOV Raman lidar technique suits principally both objectives A and B it is one of the few measurement techniques that can link the insights obtained by following both approaches. This link is very important for a deeper understanding of aerosol-cloud interactions since it can bring together outcomes from numerous investigations.

6.3.2 Comparison with other ground-based cloud probing techniques

The basic advantages as well as drawbacks of various measurement approches to investigate aerosol-cloud interactions were explained in the Subsections 2.2.5 to 2.2.7. Therefore, this subsection is confined to the comparison of the dual-FOV Raman lidar techniques to other active ground-based remote-sensing techniques for cloud measurements.

Comparison with other lidar measurement techniques

In comparison with the lidar techniques presented in Subsection 5.1.2, the dual-FOV Raman lidar technique stands out as the most robust and straightforward approach, considering measurement setup and retrieval algorithm to derive profiles of the cloud droplet size. This is a great and important advantage regarding investigations of aerosol-cloud interactions, especially because robust setups are important for long-term measurements. The major drawback of the dual-FOV Raman lidar technique is the restriction to night time measurements. A minor point is that the only alternative approach for deriving profiles of the cloud droplet size [*Bissonnette and Hutt*, 1995; *Bissonnette et al.*, 2002, 2005] works up to optical depths of 4 to 4.5, exceeding the average penetration depth of the performed dual-FOV Raman lidar cloud probings of about 3.0 slightly.

Comparison with radar measurements

As mentioned in Section 3.4, cloud microphysical properties can be retrieved with radar measurements. In several investigations of aerosol-cloud relationships radars were employed [*Feingold et al.*, 2003; *McComiskey et al.*, 2009]. Profiles of LWC, cloud droplet size, and CDNC can be obtained. With the capability of penetrating even thick clouds these profiles can be derived up to the upper cloud layers which are most important for the cloud albedo. A further advantage of radar cloud probings is the possibility to perform not only night time but also day time measurements.

Despite the advantages of radar measurements, there are also shortcomings. The accuracy of the radar retrievals for thin water clouds is modest, also because of the limited accuracy of the corresponding MWR measurements which are used by the radar retrievals. Hence, for

the examination of the radiative effects of these clouds in earth's radiative budget, dual-FOV Raman lidar measurements are the ideal complement to radar probings.

Also for investigations regarding objective A, the dual-FOV Raman lidar technique is the ideal complement to radar measurements as it can remedy the problems of radar retrievals at cloud base. The retrievals used to analyze radar measurements show their largest uncertainties at cloud base because of the limited sensitivity of radar measurements to small droplets, which are formed in this region. This deficiency is an important drawback because of the importance of the cloud base region for investigations of aerosol-cloud interactions (cf. Subsection 2.2.2). The highly demanded measurements at cloud base become possible with dual-FOV Raman lidar measurements, which have a very high sensitivity at cloud base as this is the region where the detected lidar signals are least attenuated.

Additionally, the synergy of radar and dual-FOV Raman lidar measurements provides profiles of cloud microphysical properties from base to top. Thereby, it establishes a link between investigations pursuing objective A (requiring information at cloud base) and B (requiring primarily information at cloud top).

Furthermore, dual-FOV Raman lidar measurements can be employed to enhance radar retrievals. For example, the retrieval of *Martucci and O'Dowd* [2011] requires the knowledge of the profile of the extinction coefficient inside the cloud from lidar measurements. Not considering multiple-scattering effects in water clouds, conventional lidar data analysis methods lead to errors of the retrieved extinction coefficient of up to 50% [*Wandinger*, 1998]. The dual-FOV Raman lidar technique suits ideally to overcome this problem.

Chapter 7

Case studies

The following chapter presents four case studies for which cloud microphysical properties are derived with the dual-FOV Raman lidar technique. These studies deal with aerosol-cloud interactions, a comparison of CCN concentration and CDNC, and the influence of the vertical wind velocity on cloud microphysical properties. On the one hand, these case studies deal with issues of high scientific interest. On the other hand, these investigations illustrate the capabilities of the dual-FOV Raman lidar technique to examine aerosol-cloud interactions with a profound approach as the case studies do not merely assess the aerosol particle extinction coefficient and cloud droplet effective radius but also the cloud dynamics, the APNC, and CDNC. Parts of this chapter have been published in *Schmidt et al.* [2014] and are adopted without explicit citing.

7.1 Altocumulus in clean and moderately polluted air

In Section 6.3 the feasibility to examine aerosol-cloud interactions with the Raman lidar MARTHA, employing the dual FOV technique, was asserted. In this section, a case study is presented in which aerosol-cloud relationships are investigated. The results of two dual-FOV Raman lidar probings of warm, layered altocumulus clouds are compared. As reasoned in Subsections 6.3.1, the aerosol particle extinction coefficient is utilized as a measure for the aerosol load below the cloud and thus CCN concentration. The cloud response to a change in aerosol load was examined in terms of the cloud droplet effective radius as well as CDNC.

Fig. 7.1 shows the time-height cross section of the range-corrected lidar signal at 532 nm from the inner FOV of MARTHA of the measurements performed on 26 July 2011 and 5 September 2011 with FOV pairs of 0.78 and 3.8 mrad and 0.5 and 2.0 mrad, respectively. The signal averaging periods used for the cloud analysis are indicated by pink lines in Fig. 7.1.

The probed layered clouds formed at free-tropospheric heights above 2.5 km in clean and polluted air. The Hybrid Single-Particle Lagrangian Integrated Trajectory (HYSPLIT) model [*Draxler and Rolph*, 2013] was employed to identify the origin of the air masses by calculations of ten-day backward trajectories, which are shown in Fig. 7.2. The rather clean air mass measured on 26 July 2011 was advected from Greenland over Iceland and the

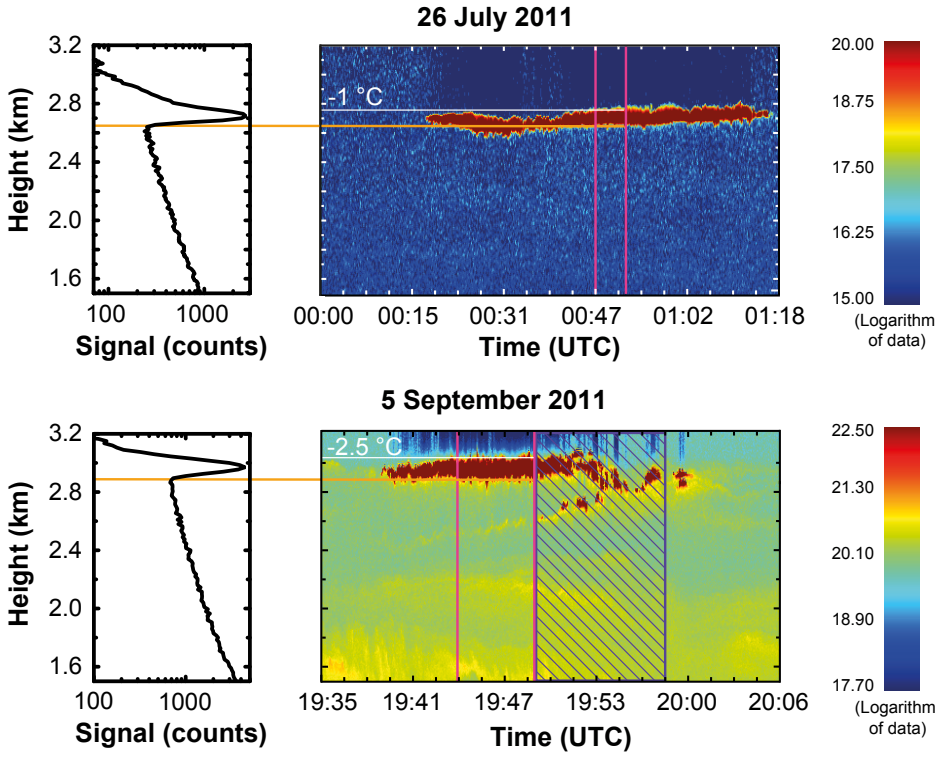

Figure 7.1: Altocumulus layers (in red) observed with MARTHA on 26 July 2011 (top) and 5 September 2011 (bottom). The range-corrected signal (arbitrary units) at 532 nm from the inner FOV is shown. The time period used for the cloud analysis is indicated by pink lines. For the retrieval of the aerosol backscatter and extinction coefficients on 26 July, displayed in Fig. 7.3, the complete time period shown here is used. For the retrieval of the aerosol properties on 9 September the purple hatched time period was not considered. The cloud-top temperatures, derived from the GDAS temperature profiles for grid point Leipzig at 0:00 UTC on 26 July 2011 and 21:00 UTC on 5 September 2011, are given as white numbers. The left panels show the signal profiles from the outer FOV at 607 nm measured during the time periods highlighted with pink lines. The cloud base heights, derived from these profiles, are indicated with orange lines.

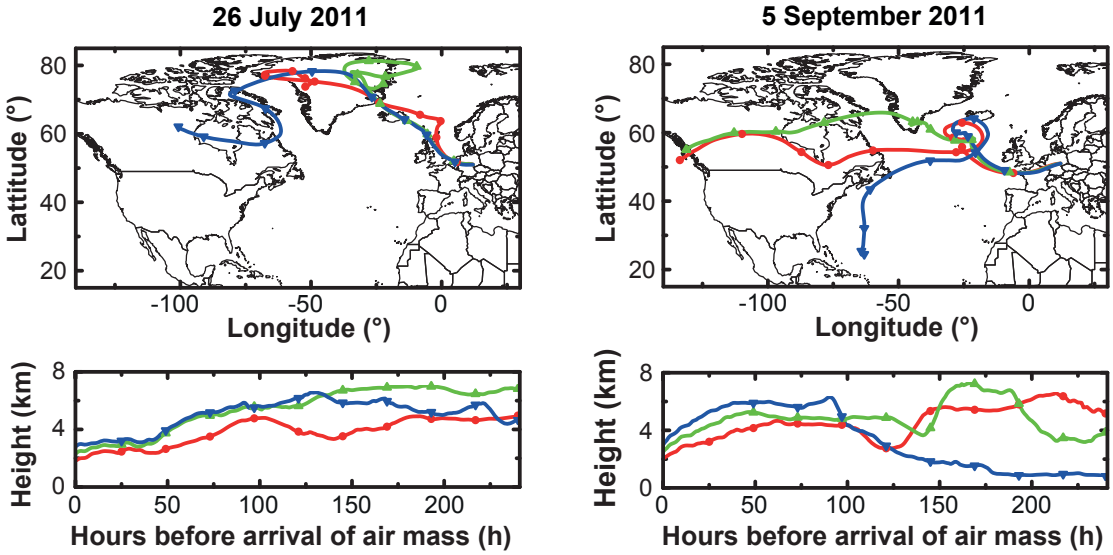

Figure 7.2: Ten-day backward trajectories calculated with HYSPLIT. The trajectories arrive over Leipzig at altitudes of 1.8, 2.3, and 2.8 km on 26 July 2011, 1:00 UTC (left) and at altitudes of 2.0, 2.5, and 3.0 km on 5 September 2011, 20:00 UTC (right).

North Atlantic towards Germany. Hence, the corresponding cumulus layer developed under background aerosol conditions. The hazy air mass on 5 September 2011 originated from polluted regions of North America and crossed polluted parts of western Europe before arriving at Leipzig, Germany, according to the backward trajectory analysis.

Profiles of the particle extinction and backscatter coefficients at 532 nm, which are displayed in Fig. 7.3, were derived from the Raman lidar measurement (cf. Subsections 4.2.2 and 4.2.3). For the determination of the aerosol backscatter and extinction coefficients on 26 July 2011 the complete time period shown in Fig. 7.1 was used, because the corresponding aerosol layer is relatively homogeneous and thus represents the aerosol properties in the time period utilized for the cloud analysis. For the retrieval of the aerosol properties on 5 September 2011 the purple hatched time period was excluded. The occurrence of clouds in about 2.7 km altitude and the corresponding influence of water uptake by particles leads to an increase of the particle backscatter and extinction coefficients, which is not correlated with the APNC in the time period in which the cloud properties were derived. The reference heights for the profiles of the backscatter coefficients were set in relatively homogeneous aerosol layers with few hundred meters extent below the clouds. The corresponding values of the backscatter coefficients in these layers were obtained from the profiles of the backscatter coefficients derived from the cloud-free profiles shown in Fig. 7.1, which have in the corresponding height range similar structures as in the time periods of the cloud analyses. The reference heights for the profiles from the cloud-free periods were set in the upper troposphere.

In the case of the extinction coefficient a smoothing length of 500 m was applied. For the determination of the backscatter coefficient, displayed in Fig. 7.3, a smoothing length

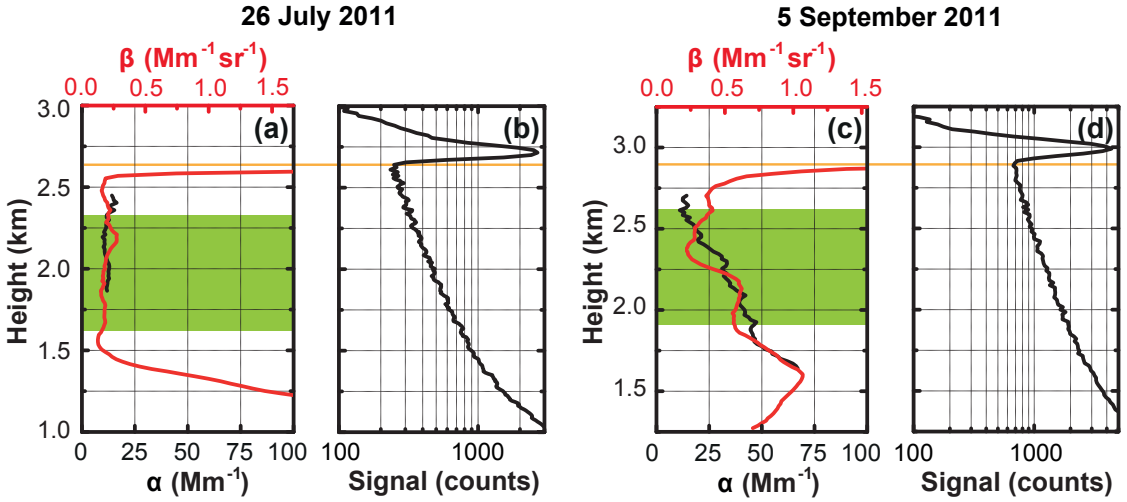

Figure 7.3: (a) Profiles of the aerosol particle extinction α (black) and backscatter coefficients β (red) below the clouds measured from 00:00–01:18 UTC on 26 July 2011 and (c) from 19:35–19:49 and 19:58–20:06 UTC on 5 September 2011. The scalings of the backscatter coefficients with regard to the extinction coefficients correspond to the derived lidar ratios of 60 and 65 sr, respectively. The altitude ranges used for the determination of the average extinction coefficients and lidar ratios are highlighted in green. (b), (d) Signal profiles from the outer FOV at 607 nm for the corresponding cloud measurements. The cloud base height, derived from these profiles, is highlighted in orange.

of 60 m was used. The lidar ratio was calculated in the altitude where both extinction and backscatter coefficients could be derived. For this calculation the same smoothing length was applied to the profiles of the backscatter and extinction coefficients (500 m). Lidar ratios of 60 ± 14 and 65 ± 20 sr were obtained from the measurements on 26 July and 5 September, respectively. These lidar ratios are typical for aged fine-mode particles of anthropogenic origin [*Müller et al.*, 2007].

The profiles of the particle extinction coefficients, used to quantify the aerosol loads below the clouds, were calculated from the derived profiles of the particle backscatter coefficients and the obtained lidar ratios. The advantage of this method, compared to the utilization of the extinction coefficient calculated directly from the measured Raman signal according to Section 4.2.3, is the higher signal-to-noise ratio as well as the finer height resolution which enables a better representation of the aerosol load directly below the clouds. Furthermore, this methods allows the determination of the extinction coefficient also in lower altitudes (with the assumption that no variations in the aerosol type occur) as the backscatter coefficient derived with the Raman method is far less susceptible to the overlap function than the extinction coefficient (cf. Section 4.2.2).

The increase of the extinction coefficient due to the growth of aerosol particles in a humid environment was treated already in Section 6.1.4. This increase, which is caused by aerosol growth and which is not correlated with an increase in CCN concentration, was obtained

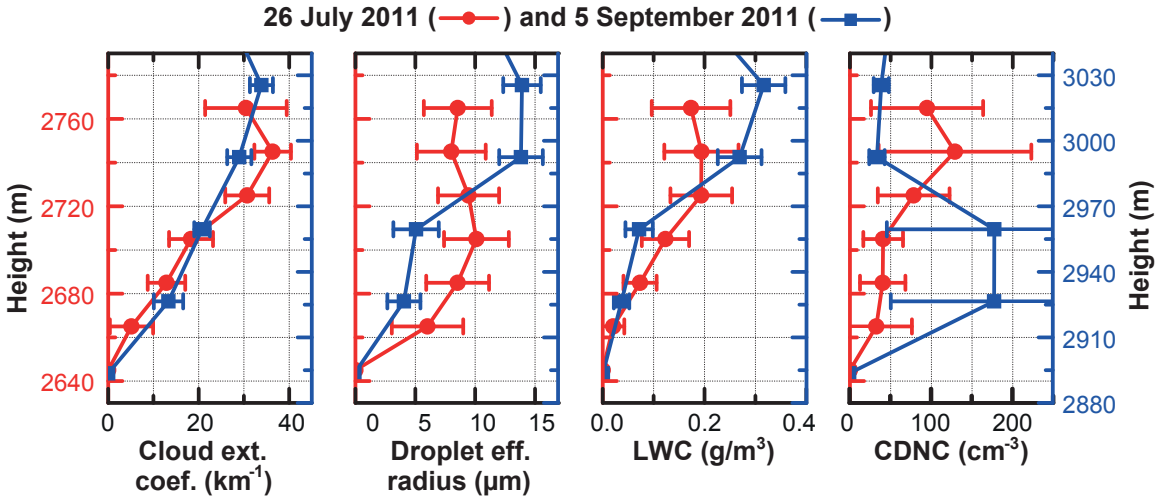

Figure 7.4: Cloud microphysical properties (extinction coefficient α, effective radius r_{eff}, liquid water content LWC, and CDNC) obtained with the forward iterative algorithm. Error bars show the corresponding uncertainties. On 26 July (red profiles) the aerosol load below cloud base was a factor of two to three lower than on 5 September 2011 (blue profiles). For similar LWC conditions, larger cloud droplets and lower CDNC are observed in the lower part of the cloud in the case of the lower aerosol load.

already 100 m below cloud base. Figure 7.3(c) as well as the profiles of the extinction coefficients from the follwing case studies, presented in Fig. 7.9 and 7.14, show a corresponding increase already about 300 m below cloud base. Hence, for the quantification of the aerosol load below the clouds the extinction coefficient within a distance of 300 m to the cloud base was not considered. The extent of the layer, where the extinction coefficient is to be considered and averaged, was set to 700 m to minimize the effects of signal noise. Thus, the aerosol particle extinction coefficients were averaged from 300 to 1000 m below cloud base. The measurement on 26 July shows an average extinction coefficient of 12 Mm^{-1} which constitutes a rather clean case, whereas the measurement from 5 September shows an average extinction coefficient of about 29 Mm^{-1} and thus can be considered as a hazy aerosol case.

The cloud microphysical properties retrieved with the forward iterative algorithm are presented in Fig. 7.4. In the lower part of the clouds the LWCs are similar with slightly larger values in the clean case. The cloud in the hazy case shows smaller droplet effective radii than the cloud in the clean case. In the height range between about 30 and 70 m above cloud base, the cloud droplet effective radii are 5.1 and 9.6 µm in the hazy and clean case, respectively, for LWCs of 0.054 and 0.083 g/m^3. These findings correspond to aerosol-cloud interactions related to the Twomey effect, although the differences in LWC might play a role for the differences in cloud droplet size as well. The difference between the effective radii is about a factor of two, whereas the LWC difference is about a factor of 1.5.

The case becomes clearer with the comparison of the profiles of the CDNC. In penetration depths between about 30 and 70 m the CDNC is much higher in the hazy case ($180 \pm 150\ \text{cm}^{-3}$)

than in the clean case ($50 \pm 40\,\mathrm{cm}^{-3}$). Care has to be taken with quantitative analyses due to the large errors of the derived CDNCs. However, it should be mentioned that the difference between the CDNCs of a factor of about 4 is similar to the difference of the aerosol extinction coefficients below the clouds which is of the order of a factor of 3.

However, above a penetration depth of about 90 m the observed behavior of the cloud microphysical properties reverses. In this height region, the cloud with the higher aerosol load below exhibits larger droplet radii and a lower CDNC. This finding illustrates that aerosol-cloud relationships are strongest in the lower part of clouds. In larger penetration depths other cloud processes, such as coagulation or various mixing processes, may become dominant.

Three main conclusions can be drawn from this case study. First, the dual-FOV Raman lidar technique is capable of assessing aerosol-cloud interactions. Second, the capability of deriving profiles of cloud microphysical properties is of extraordinary importance. Without the profiling information and thus the access to the cloud microphysical properties in the lower part of the cloud, the effect of aerosol-cloud interactions could not be ascertained in this case. Third, despite the large errors (cf. Subsection 6.2.4), the CDNC is an important quantity for investigations of aerosol-cloud interactions. As possible effects of changing LWCs do not have to be considered the analyses become clearer.

7.2 CDNC at altocumulus cloud base and CCN concentration

In Subsection 4.2.5 it was stated that aerosol microphysical properties, e.g., APNC, can be derived from multiwavelength Raman lidar measurements, applying the method of inversion with regularization. Here, this capabality is used to assess the CCN concentration in the proximity of two clouds and to compare this concentration with the CDNC at the cloud bases obtained from dual-FOV Raman lidar measurements. Figure 7.5 shows two probed cloud layers in an altiutude of 3.3 and 3.7 km. The time periods utilized for the cloud analyses are indicated with pink lines. The cloud-free period from 19:10–19:30 UTC between the clouds was used for the aerosol analysis. The measurement was performed with FOVs of 0.5 and 2.0 mrad.

The aerosol optical properties for the cloud-free period are presented in Figs. 7.6(a) to (d). In the case of the extinction profiles, the Raman signals were vertically smoothed with a height-dependent window length of 500 to 800 m. For the calculation of the lidar ratio, the same smoothing length was applied to the profiles of the backscatter coefficients. In contrast, the backscatter coefficients shown in Fig. 7.6(a) are given with a resolution of 60 m. The aerosol optical properties indicate moderately polluted aerosol conditions up to 3 to 4 km height. The 532-nm particle extinction and backscatter coefficients were about $20\,\mathrm{Mm}^{-1}$ and $0.4\,\mathrm{Mm}^{-1}\mathrm{sr}^{-1}$, respectively.

These results were utilized to derive the APNC of the accumulation and coarse modes (retrieval radius range from 0.05 to 5 μm) with the inversion method. In this case, the number concentration of aerosol particles which are in the height range of the probed clouds and are

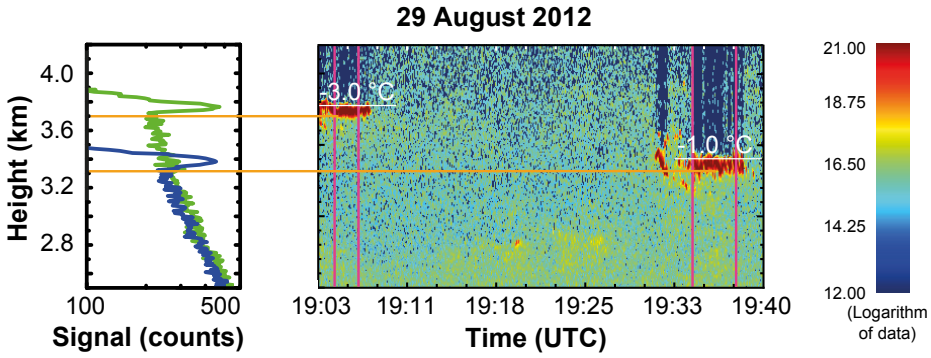

Figure 7.5: Time-height cross section of the range-corrected lidar signal from MARTHA at 532 nm, inner FOV. The time periods used for the cloud studies are indicated by pink lines. The cloud-top temperatures, derived from the GDAS temperature profile for grid point Leipzig on 29 August 2012, 18:00 UTC, are inscribed in white color. The left panel shows the signal profiles from the outer FOV at 607 nm measured during the time periods used for the cloud analyses, 19:04–19:07 UTC (green) and 19:34–19:38 (blue). The cloud base heights, derived from these profiles, are highlighted with orange lines.

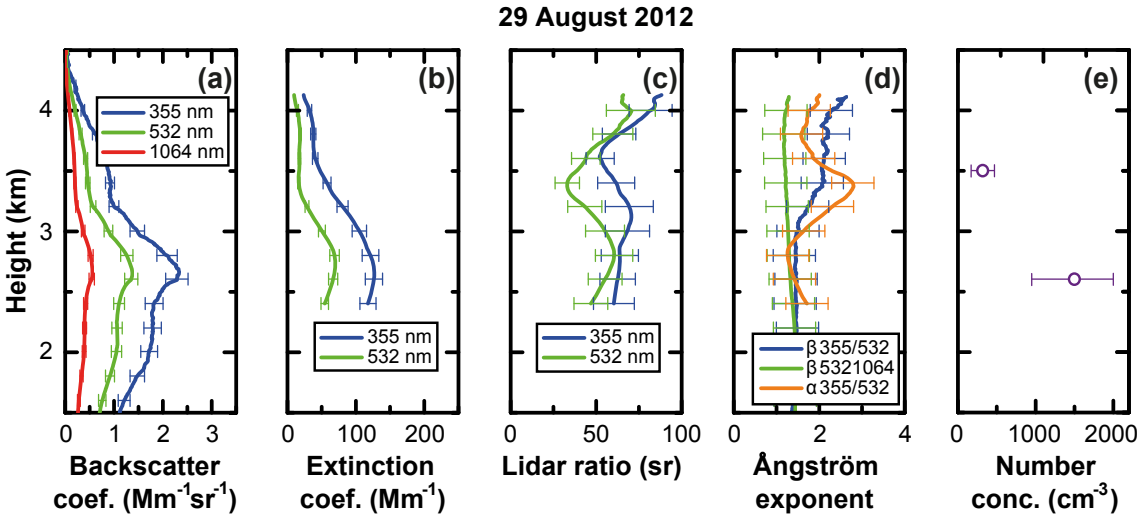

Figure 7.6: (a)–(d) Aerosol optical properties used for the inversion scheme. The profiles were measured on 29 August 2012 in the cloud-free period from 19:15 to 19:30 UTC. The relative errors of the backscatter and extinction coefficients were estimated to 10%. From these errors the uncertainties of the lidar ratios and Ångström exponents were derived according to Gaussian error propagation. (e) Number concentration of aerosol particles with a radius greater than 85 µm, which are assumed to be capable of acting as CCN. The corresponding values are given for the 600-m-thick aerosol layers in the altitudes around 2.7 and 3.5 km, characterizing the aerosol below the cloud and at cloud formation level, respectively.

of sufficient size to be potential CCNs is of particular interest. Although dependent on the supersaturation at cloud base (cf. Section 2.1), this critical size, also denoted as activation radius, is typically about 50 nm [*Twohy et al.*, 2005; *Dusek et al.*, 2006; *Asmi et al.*, 2012; *Kleinman et al.*, 2012; *Ditas et al.*, 2012]. However, the activation radius of about 50 nm refers to aerosol particles in a dry environment. The probed aerosol layers are exposed to humidity and thus aerosol particle growth.

For the estimation of the impact of this effect, the profile of the relative humidity for the corresponding time period was determined from the water-vapor mixing ratio measured with MARTHA [*Mattis et al.*, 2002]. For the required calibration, the integrated water-vapor content obtained with the MWR was used. The profiles of temperature and pressure were taken from the simulated GDAS sounding at 18 UTC. In the height range from 3.2 to 3.8 km a relative humidity of 65% was found. Compared to aerosol particles in a dry environment, this humidity leads to a growth factor for the aerosol particle radius of about 1.7 for a gamma value of 0.5, which is the average value for aerosol particles over Leipzig [*Skupin*, 2013]. Thus, the dry activation radius of 50 nm corresponds to a particle radius of about 85 nm under the conditions present in the aerosol layer between the clouds in the altitude of the cloud occurrence (3.2 to 3.8 km).

The APNC for particles exceeding this size was determined to about $300\,\mathrm{cm}^{-3}$ with an uncertainty of approximately $150\,\mathrm{cm}^{-3}$ in the corresponding aerosol layer. Due to the homogeneity of the probed aerosol layer this result is supposed to be representative for the airmass in which the clouds formed. This result as well as the similarly obtained APNC in about 2.7 km altitude are displayed in Fig. 7.6(e).

Figure 7.7 presents the microphysical properties of the two clouds. The cloud extinction coefficients and the LWC values are higher in the upper cloud layer (displayed in blue) than in the lower one (displayed in red). Effective radii are similar in both clouds. The CDNC values are rather uncertain because of the relatively large errors in the cloud droplet effective radii of 25% to 40% and a respective error contribution to the CDNC relative uncertainty of 50% to 100% (cf. Subsection 6.2.4). The co-located cloud radar did not indicate any drizzle formation.

According to Figs. 7.6(e) and 7.7, the CDNC is of the order of 50 to $80\,\mathrm{cm}^{-3}$ with relative errors of about 100% in the lowest part of the cloud layers, whereas the APNC is around $300 \pm 150\,\mathrm{cm}^{-3}$ in the corresponding altitude. Despite of the large errors in both the CDNC and APNC the tendency that only a fraction of the aerosol particles with dry radii exceeding 50 nm acts as CCN becomes obvious. Roughly 15% to 25% of these aerosol particles served as CCN in this measurement case. However, the relative error of these values is about 110% which expands the error range of the derived CDNC/APNC ratio from 0.07 to 0.53.

Airborne in-situ measurements in the stratocumulus-topped marine boundary layer over the Pacific, which assessed the APNC for particles larger than 50 nm in dry radius, yield CDNC/APNC ratios of 0.6 to 1.0 at CDNCs of 25 to $400\,\mathrm{cm}^{-3}$ with the tendency of slightly higher CDNC/APNC ratios for smaller CDNCs [*Twohy et al.*, 2005, 2013; *Kleinman et al.*, 2012]. At an European continental mountain site, *Asmi et al.* [2012] observed CDNC/APNC

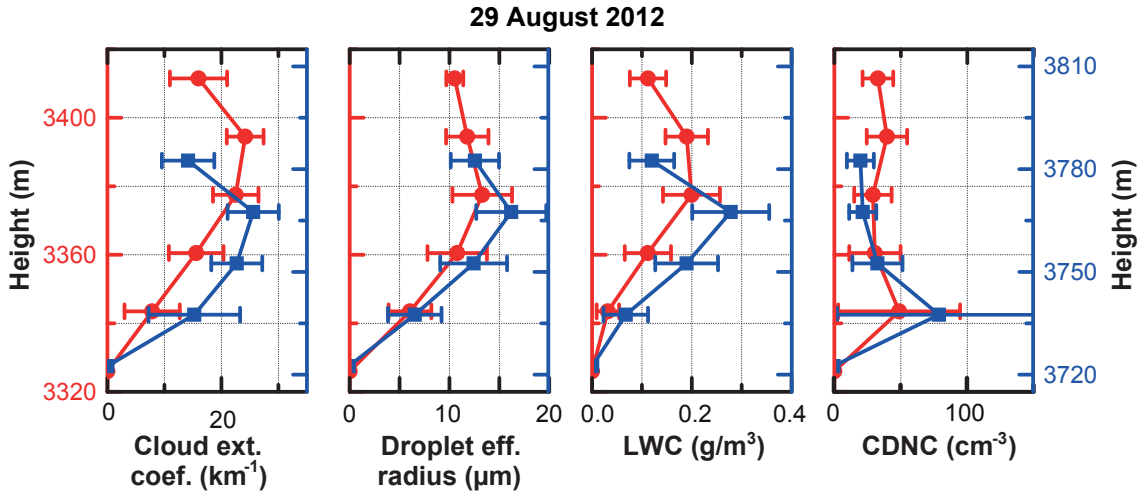

Figure 7.7: Cloud microphysical properties obtained from the dual-FOV Raman observation on 29 August 2012, 19:04–19:07 (displayed in blue) and 19:34–19:39 UTC (displayed in red). The lowest 20 m of the clouds show CDNCs of 79 ± 106 and $49 \pm 65\,\mathrm{cm}^{-3}$.

values of 0.5–0.7 within the continental PBL. Large variations in the ratio were typical for all observations.

Considering the uncertainties of the applied method as well as the uncertainties of the methods in the cited publications, these results agree to a certain degree, with a tendency of a lower CDNC/APNC ratio derived with ground-based remote sensing. Generally CDNC/APNC ratios below 1 are reasonble for the following reason. For both the cited studies as well as the dual-FOV Raman lidar measurements the cloud properties are mean values for the entire cloud without consideration of up- and downdraft regions. At best during updraft periods, when aerosol particles are mixed into the cloud, one might expect the aerosol to dominate the cloud properties at cloud base, which would cause a CDNC/APNC ratio of about 1. In other time periods, coagulation, evaporation, and various mixing processes may take place to a significant extent, decoupling CCN concentration below cloud base and CDNC at cloud base to some degree. The mentioned processes will also occur in cloud regions with moderate updrafts although to a much smaller extent. Hence, differences in vertical wind velocities also might cause the differences of the CDNC/APNC ratios between this and the cited studies. The cause for not considering the vertical wind speed in the dual-FOV Raman lidar measurement was the short duration of the cloud probing. Thus, the averaging time for the analysis considering updraft-influenced profiles only, would have been too short for a successful run of the forward iterative algorithm to retrieve the cloud properties.

7.3 Influence of up- and downdraft motions

In this section, the impact of up- and downdrafts on the evolution of the microphysical characteristics of layered clouds is discussed. This examination is done on the basis of two

case studies for which combined measurements of the Doppler wind lidar WiLi and the dual-FOV Raman lidar MARTHA are analyzed.

7.3.1 Activation and downmixing of large droplets

Figure 7.8 shows a dual-FOV Raman lidar measurement performed on 15 August 2011. A 150 to 250 m thick, stable cloud layer was present for more than two hours. There was no drizzle observed with the cloud radar. The FOVs employed in the dual-FOV lidar measurement were 0.5 and 2.0 mrad. The pink lines in Fig. 7.8 indicate the time period used for the cloud analysis. During this period, the altocumulus showed homogeneous structures with a constant cloud base height at 2.78 m (cf. Fig. 7.8). Afterwards, the cloud base height was slightly lifted by about 50 to 100 m.

The profiles of the aerosol particle backscatter and extinction coefficients are shown in Fig. 7.9. The backscatter profile increases from 300 m below cloud base onwards due to particle water uptake. The particle extinction coefficient ranges from 20 to 50 Mm^{-1} between 1.5 and 2.5 km height. For the height range from 1.8 to 2.3 km, a lidar ratio of 55 sr was found.

The vertical wind velocity at the cloud base, obtained with the Doppler lidar for the selected 16-minute cloud observation, is presented in Fig. 7.10 (top). Corresponding vertical wind statistics are shown in Fig. 7.10 (bottom). The up- and downdraft speeds were mostly below 0.5 m/s.

The measured dual-FOV Raman signals were sorted according to the occurrence of up- and downdrafts. A dual-FOV Raman signal profile was assigned to an updraft or downdraft region, if the corresponding vertical velocity showed a positive or negative value at cloud base, respectively. 83 updraft-related and 123 downdraft-related MARTHA signal profiles

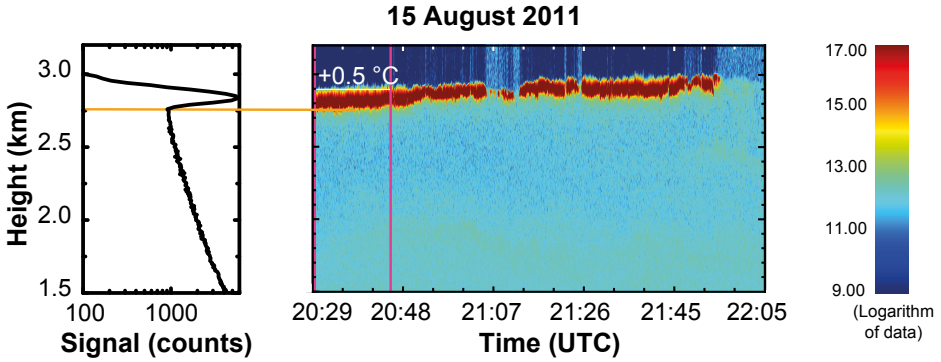

Figure 7.8: Time-height cross section of the range-corrected lidar signal (arbitrary units) from MARTHA at 532 nm, inner FOV. The time period used for the cloud study is indicated by pink lines. The cloud-top temperature, derived from the GDAS temperature profiles for grid point Leipzig at 21:00 UTC on 15 August 2011, is inscribed in white color. The left panel shows the signal profile from the outer FOV at 607 nm, measured during the time period used for the cloud analysis. The cloud base height, derived from this profile, is highlighted with an orange line.

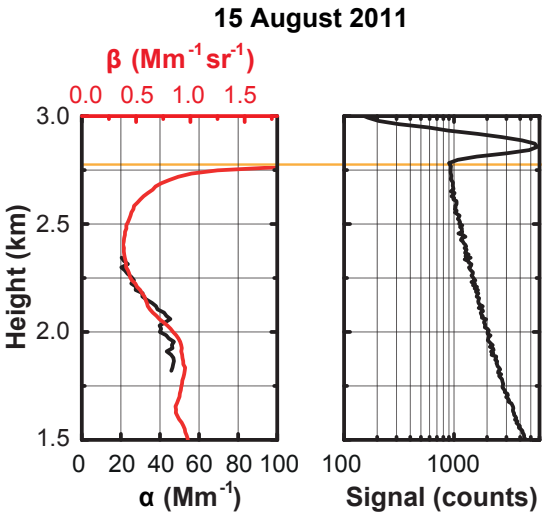

Figure 7.9: Left: profiles of the aerosol particle extinction α (black) and backscatter coefficient β (red) measured on 15 August 2011, 20:29–21:30 UTC. The backscatter coefficients are almost equal to the extinction coefficients when multiplied with a lidar ratio of 55 sr. Right: signal from the outer FOV at 607 nm, measured in the time period used for the cloud analysis. The cloud base height was derived from this signal and is highlighted in orange. The higher humidity below cloud base leads to an increase of the backscatter coefficient by a factor of 3.5 from 0.38 Mm^{-1} at 2.4 km height to 1.3 Mm^{-1} at 2.75 km height.

(each accumulated over 4 s) were averaged. Afterwards, the forward iterative algorithm was applied to both data signal sets separately.

Figure 7.11 presents the derived cloud microphysical properties. A clear difference in the cloud properties for updraft and downdraft periods is especially visible in the cloud droplet extinction coefficient in the lowermost height level of the cloud layer. This finding results from a higher CDNC at cloud base during updrafts of about a factor of three. That increased CDNC can be attributed to new droplet formation. Lower cloud droplet effective radii in the ascending air, in particular in the second height level, are consistent with this hypothesis. A further reason for the larger cloud droplets in downdraft regions may be the downward transport of cloud parcels from the well-developed upper cloud part, which contains larger particles.

7.3.2 Entrainment

Another cloud probing with MARTHA and WiLi is shown in Figs. 7.12 and 7.13. The FOVs employed for the dual-FOV measurement were 0.5 and 2.0 mrad. Again an ice-free cloud was analyzed. Major variations of the cloud base height and holes in the measured cloud field occurred. Furthermore, some parts of the analyzed cloud at 2.38 km height were obscured by clouds below. The corresponding time periods were not considered for the data analysis. In Fig. 7.13 (top) these periods are indicated by black columns. In the time periods used for

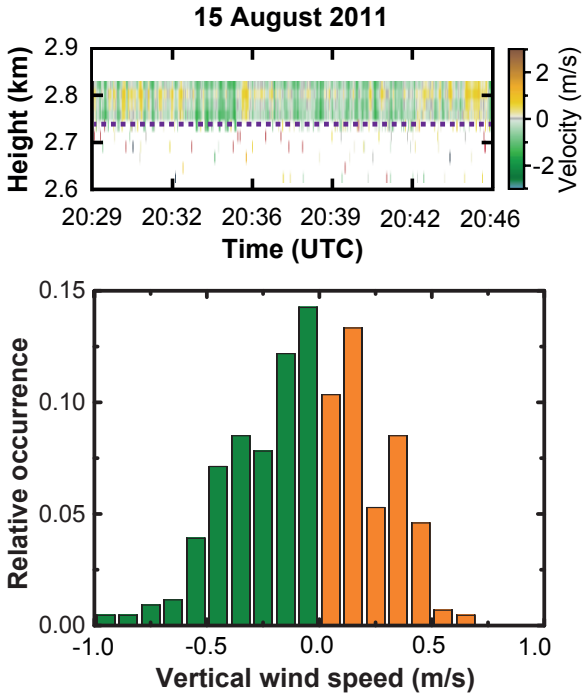

Figure 7.10: Top: vertical wind velocity at cloud base measured with WiLi during the time period indicated by pink lines in Fig. 7.8. Bottom: relative occurrence of measured vertical wind velocities (downdrafts in green, updrafts in orange) at cloud base, measured on 15 August 2011, 20:29–20:46 UTC. The cloud base height, derived from the signal profiles from the outer FOV (cf. Fig. 7.9), is indicated by a purple dotted line.

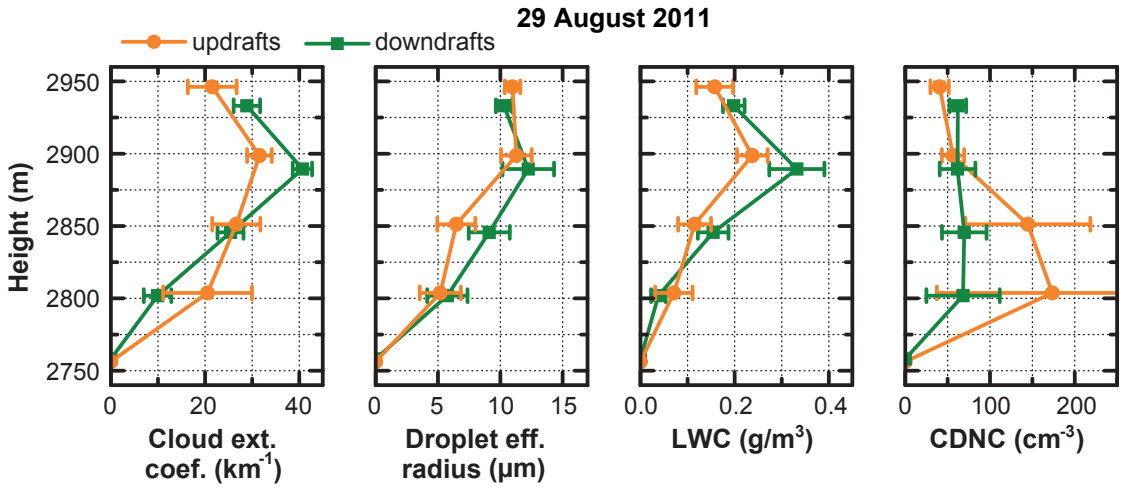

Figure 7.11: Cloud microphysical properties retrieved from the dual-FOV Raman lidar observations during updraft (orange) and downdraft (green) periods on 15 August 2011, 20:29–20:46 UTC.

the cloud analysis, the cloud base height was determined to 2.4 km from the Raman signal measured in the outer FOV (cf. Fig. 7.14). 74 4 s-profiles measured during updraft periods and 100 downdraft profiles were used for the data analysis.

The observed up- and downdrafts were comparably weak, as shown by Fig. 7.13 (bottom). Most vertical wind speeds (70%) were in the range from −0.2 m/s to 0.2 m/s, which is a much larger fraction than in the measurement of 15 August 2011 (50%), presented in the previous section. Especially updrafts show low absolute vertical velocities with only 5% of the measured wind velocities exceeding 20 cm/s. These condition may be favorable for other effects to become dominant, e.g., downward mixing of dry air from above the shallow cloud layer.

The profiles of the backscatter and extinction coefficients below the cloud are presented in Fig. 7.14. The lidar ratio is 45 sr. The extinction coefficient ranged from 45 to 110 Mm^{-1} in the altitude from 1.5 to 2.2 km.

The cloud microphysical properties, presented in Fig. 7.15, differ considerably from the findings of the previous case study. Lower effective radii and lower LWC values were observed around cloud center during the downdraft periods on 29 August. Entrainment of dry air from above, which leads to evaporation, is a feasible explanation for this finding. The comparably low updraft velocities may have been insufficient for strong new drop formation which would then decrease the effective radius.

To corroborate the hypothesis of dry-air entrainment, the adiabatic LWC profile was calculated. The microwave radiometer HATPRO allows the determination of the temperature profile. The accuracy of this retrieval is about 1.5 K in an altiude range around 2.4 km height [*Löhnert and Maier*, 2012]. A temperature of -0.2 ± 1.5°C was obtained at cloud base. For comparison, the simulated GDAS temperature at cloud base height was 0°C for

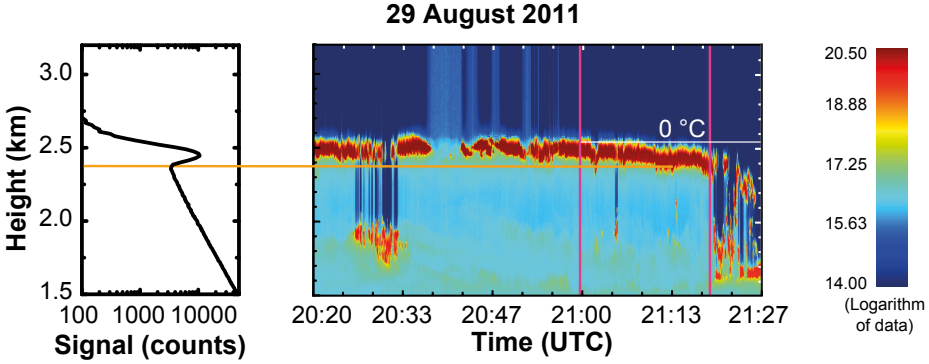

Figure 7.12: Time-height cross section of the range-corrected lidar signal from MARTHA at 532 nm, inner FOV. The time period used for the cloud study is indicated by pink lines. The cloud-top temperature, derived from the GDAS temperature profile for grid point Leipzig on 29 August 2011, 21:00 UTC, is inscribed in white color. The left panel shows the signal profile from the outer FOV at 607 nm measured during the time period used for the cloud analysis. The cloud base height, derived from this profile, is highlighted with an orange line.

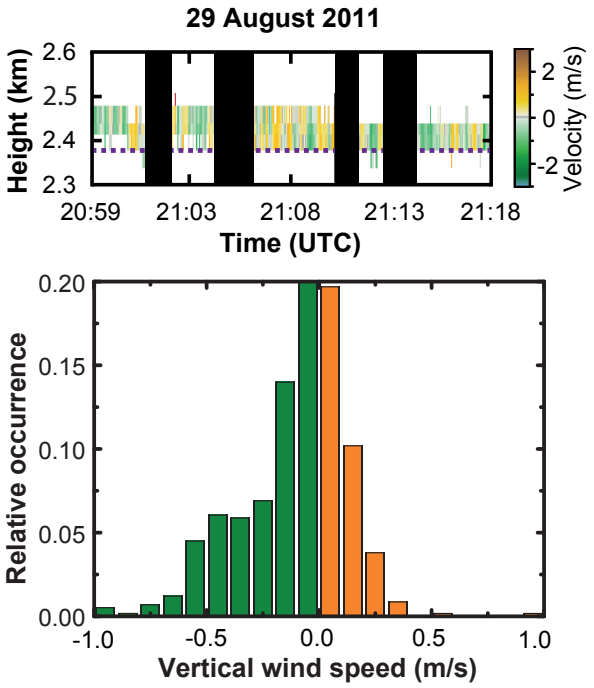

Figure 7.13: Top: vertical wind velocity at cloud base measured with WiLi during the time period indicated by pink lines in Fig. 7.12. Bottom: relative occurrence of measured wind velocities (downdrafts in green, updrafts in orange) at cloud base, measured on 29 August 2011, 20:59–21:18 UTC. The cloud base height, derived from the signal profiles from the outer FOV (cf. Fig. 7.14), is indicated by a purple dotted line.

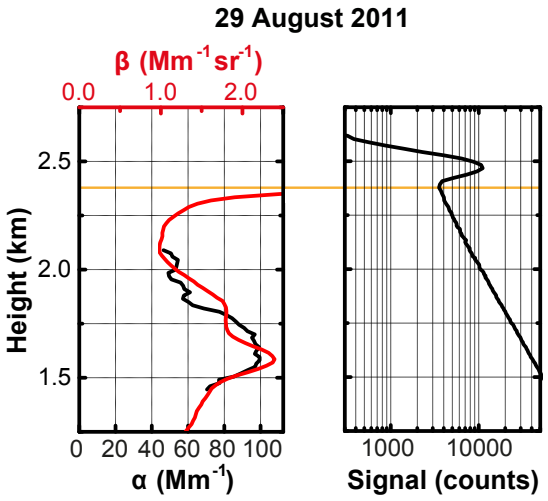

Figure 7.14: Left: profiles of the aerosol particle extinction α (black) and backscatter coefficient β (red) measured on 29 August 2011, 19:32–20:14 UTC. The backscatter coefficients are almost equal to the extinction coefficients when multiplied with a lidar ratio of 45 sr. Right: signal from the outer FOV at 607 nm, measured in the time period used for the cloud analysis. The cloud base height was derived from this signal and is highlighted in orange. The higher humidity below cloud base leads to a strong increase of the backscatter coefficient.

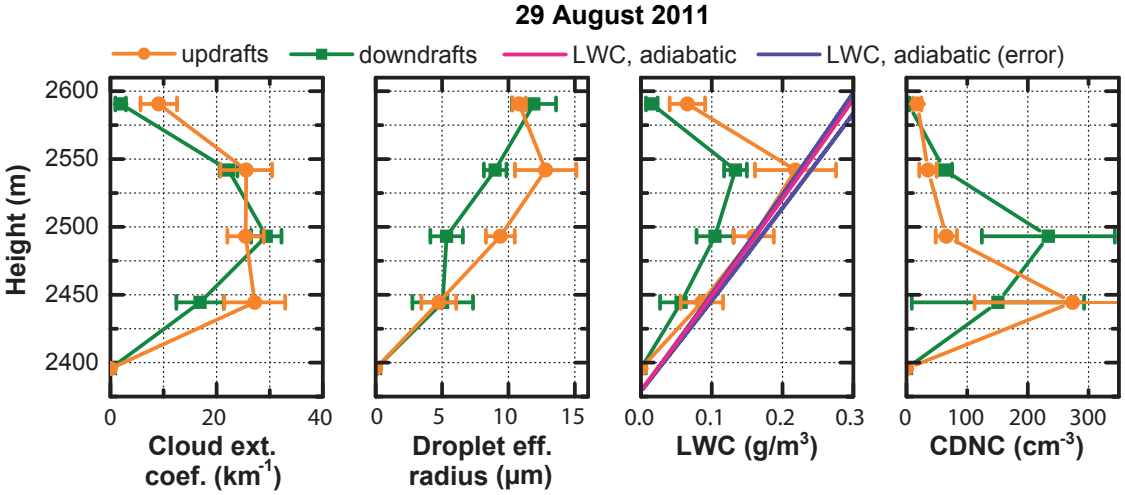

Figure 7.15: Cloud microphysical properties retrieved from the dual-FOV Raman lidar observations during updraft (orange) and downdraft (green) periods on 29 August 2011, 20:59–21:18 UTC. The calculated profile of the adiabatic LWC is shown in pink with purple lines indicating its error margin, which results from the uncertainty of the temperature at cloud base (±1.5 K).

grid point Leipzig at 21:00 UTC on 29 August 2011. The computed profile of the adiabatic LWC presented in Fig. 7.15 suggests an adiabatic increase for the updraft times, which is reasonable when droplet growth through condensation dominates. For the downdraft times, the subadiabatic LWC profile is consistent with entrainment of dry air from above.

7.3.3 Aerosol-cloud interactions under consideration of vertical wind speed

The importance of the vertical wind speed for studies of the microphysical processes of aerosol-cloud interactions was explained in Subsection 2.2.2. Here, the combined measurements of the dual-FOV Raman lidar and Doppler wind lidar presented in the two previous sections are utilized for a case study about aerosol-cloud interactions and the role of the vertical wind speed. The approach of this case study resembles the concept of the case study given in Section 7.1. Cloud properties, derived with the dual-FOV lidar technique, are compared for measurements with different aerosol extinction coefficients below the cloud, obtained from the Raman lidar measurement. To quantify the observations, ACI_{N} values, which were introduced in Subsection 2.2.3, are calculated. However, it has to be mentioned that for a quantitiative analysis of aerosol-cloud interactions, for which the ACI concept was actually developed, two measurement cases are by far not sufficient. Not only measurement uncertainties make an accurate determination of aerosol-cloud relationships impossible but especially the wide range of further influences on cloud properties (cf. Subsection 2.2.1). Hence, this case study is merely meant as an illustration of the capability of combined dual-FOV and Doppler lidar measurements as well as an introduction to the ACI approach, for the facilitation of the understanding of the following chapter.

For the analysis, cloud microphysical properties obtained for updraft periods are contrasted to those during the respective complete cloud periods. Furthermore, both the corresponding cloud properties at the cloud bases as well as their averages over the clouds' vertical extents are compared. Hence, four scenarios are distinguished in this case study: (a) ACI_{N} calculation with cloud properties at the lowest height level and by considering updraft periods only, (b) same as scenario (a) but including all (updraft and downdraft) periods in the ACI_{N} computation, (c) ACI_{N} calculation with vertical mean cloud properties considering updraft periods only, and (d) same as scenario (c) but including all (updraft and downdraft) periods in the calculation. Figure 7.16 shows the aerosol extinction coefficients below the clouds. Furthermore, the CDNCs in the lowest height levels of the clouds, derived for the complete analysis time period as well as during updraft periods only, are presented.

Similarly to the procedure applied in Section 7.1 the aerosol particle extinction coefficents were averaged in a layer with a 300-m distance to the cloud base. However, in this case study the extent of this layer is only 200 m in contrast to the 700 m used in Section 7.1. Both profiles show 800 m below cloud base a behavior which is different to the trend above. Hence, a smaller height range is supposed to be more representative for the aerosol conditions directly below the clouds. The measurements performed on 15 and 29 August 2011 yield an average aerosol particle extinction coefficient of 22 and 53 Mm^{-1}, respectively.

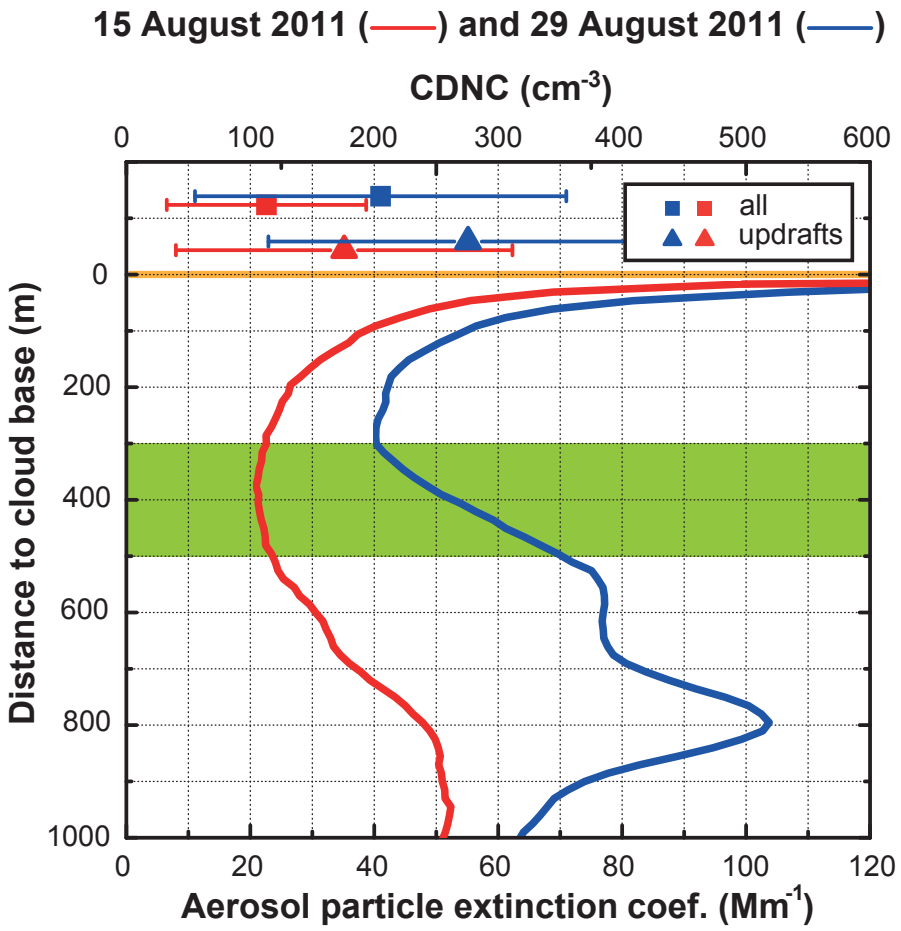

Figure 7.16: Aerosol and cloud properties used for the derivation of ACI_N values. The aerosol particle extinction coefficients for the measurements on 15 and 29 August 2011, which are the same as in Subsection 7.3.1 and 7.3.2, are shown below the clouds with solid lines in red and blue, respectively. The height range of 300 to 500 m below cloud base, where the extinction coefficients were averaged for the ACI_N calculation, is highlighted in green color. The CDNCs in the lowest cloud layer are shown with corresponding colors for updraft periods (triangles) as well as for the entire cloud probings (squares).

The LWPs of the probed clouds are about 30 and 10 g/m^2 on 15 August and 29 August, respectively. Due to this strong difference, only the utilization of the CDNC instead of the cloud droplet effective radius to derive ACI_{N} is reasonable for scenarios (c) and (d) for which integrated cloud properties are compared. For reasons of comparability, this is done for all scenarios.

The derived ACI_{N} values for scenarios (a) to (d) are presented in Table 7.1. Although it was emphasized that this case study is a mere illustration of the measurement technique and analysis approach, reasonable results were obtained. At the cloud base, where aerosol particles are mixed into the cloud, stronger aerosol-cloud relationships were derived. The corresponding ACI_{r} values of 0.18 ± 0.13 and 0.24 ± 0.17 (cf. Eq. (2.6)) match to most of the results from airborne in-situ and ground-based remote-sensing studies. However, the weaker coupling of aerosol and cloud properties at cloud base during updraft periods contradicts the understanding of aerosol-cloud interactions and is attributed to other cloud-influencing factors.

Table 7.1: ACI_{N} values of the presented case study. Cloud properties are considered at the cloud base as well as over the complete vertical cloud extent during updraft periods only as well as during the complete cloud probing.

	Updraft Periods	Complete Cloud
Cloud Base	0.55 ± 0.38	0.71 ± 0.52
Vertical Mean	0.32 ± 0.17	-0.07 ± 0.04

To assess aerosol-cloud interactions with the focus on cloud microphysical properties (objective A), scenario (a) provides optimum conditions. The ACI_{N} values of the other three scenarios (b)–(d) differ significantly (30% to 100%) from the value derived for scenario (a). This finding illustrates that downdrafts, turbulent mixing, and entrainment processes may reduce any clear aerosol effect on cloud microphysical properties on the way up through the cloud layer, which is in agreement with the work of *Kim et al.* [2008].

The findings from this case study support a central conclusion drawn from the case study presented in Section 7.1: for investigations of aerosol-cloud interactions, profile information of the measured cloud properties are of high relevance, particularly due to the importance of cloud properties derived directly at cloud base. A further major conclusion from this case study is the high relevance of the vertical wind speed for cloud microphysical properties in general and aerosol-cloud interactions in particular. Combined measurements with the dual-FOV Raman lidar and the Doppler wind lidar are capable of assessing the effects of vertical air motion on clouds.

Chapter 8

Statistical analysis of aerosol-cloud interactions

In Subsection 2.2.7 and Section 6.3 the suitability of ground-based remote-sensing techniques in general and the dual-FOV Raman lidar technique in particular to investigate aerosol-cloud relationships was outlined. Furthermore, case studies presented in Chapter 7 were used to illustrate the capabilities of the dual-FOV Raman lidar technique. Subsequently, this chapter provides a statistical analysis of observed aerosol-cloud relationships.

29 dual-FOV Raman lidar cloud measurements are considered. These measurements were performed between September 2010 and August 2012. All investigated clouds were layered, thin clouds, which are most suitable for studies of aerosol-cloud interactions (cf. Subsection 2.2.2).

The first section of this chapter describes the applied procedures for data analysis. Section 8.2 gives an overview of the derived aerosol and cloud properties. The statistical results regarding aerosol-cloud interactions are presented in Section 8.3. The chapter closes with a discussion of the obtained results in Section 8.4.

8.1 Procedure of data analysis

The aerosol load below the cloud is characterized by means of the profile of the aerosol particle extinction coefficient, which was derived with the procedure described in Subsection 7.1. In case the lidar ratio could not be derived below the probed cloud due to the effect of the overlap function, the profiles measured in cloud-free periods were utilized for the calculation.

The retrieval of cloud microphysical properties from dual-FOV Raman lidar measurements is explained in detail in Chapter 5. The cloud microphysical properties were averaged in defined height ranges. Three height ranges were used, which extend from 0 to 30 m, 30 to 70 m, and 70 to 120 m above cloud base. Thus, aerosol-cloud relationships can be investigated in several cloud penetration depths (height ranges above cloud base). The choice of the height ranges was already explained in Subsection 6.2.4, with the most important point that influences of variations of the cloud base height are restricted to the lowermost height

range. As the height ranges employed in that Subsection are identical, it gives the mean relative errors of the derived cloud quantities.

The approach of ACI values for the quantification of aerosol-cloud relationships was explained in Subsection 2.2.3. The approach was introduced for a case study presented in Subsection 7.3.3. Here, for each aerosol height range and cloud penetration depth ACI values were calculated from the analyzed dual-FOV Raman lidar measurements according to Eq. (2.2) and (2.3). The logarithms of the cloud droplet effective radii and CDNC as well as the logarithm of the layer mean aerosol extinction coefficient below the cloud were calculated. The derivative of the corresponding linear regression of these data gives $-ACI_{\mathrm{r}}$ and ACI_{N}, respectively.

8.2 Overview of retrieved aerosol and cloud properties

8.2.1 Aerosol properties

A histogram of the mean extinction coefficients for the height range from 300 to 1000 m below cloud base is presented in Fig. 8.1. Table 8.1 lists the minimum, maximum, average, and standard deviation of the derived extinction coefficients. The average of 52 Mm^{-1} matches well with the findings from *Mattis et al.* [2004], who presented the results of lidar data analyses for measurements at Leipzig between 2000 and 2003. The authors obtained a mean extinction coefficient of about 50 Mm^{-1} for the height range from 500 to 4000 m which corresponds to the height range for the aerosol analyses in this work (cf. Fig. 8.3 and Table 8.3 for obtained cloud base heights). The comparatively large range of extinction coefficients derived in this work, which extend from about 10 Mm^{-1} to almost a factor of three of the average value obtained over Leipzig, is convenient for investigations of aerosol-cloud interactions.

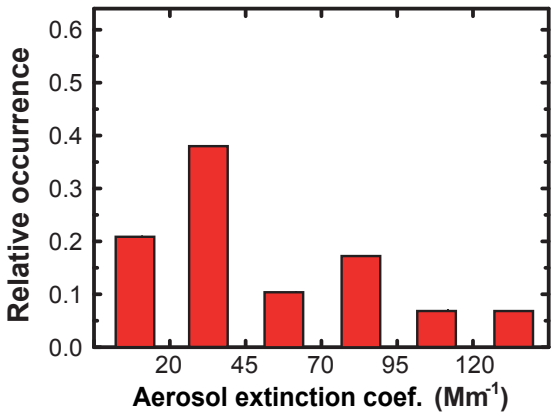

Figure 8.1: Relative occurrence of aerosol particle extinction coefficients for the height range from 300 to 1000 m below cloud base.

Table 8.1: Statistics of derived aerosol particle extinction coefficients below cloud base.

Minimum	$7\,\mathrm{Mm}^{-1}$
Maximum	$130\,\mathrm{Mm}^{-1}$
Average	$52\,\mathrm{Mm}^{-1}$
Standard deviation	$34\,\mathrm{Mm}^{-1}$

8.2.2 Cloud properties

Figures 8.2 and 8.3 give an overview of the properties of all considered cloud layers. The figures show histograms of the mean cloud extinction coefficients (Fig. 8.2(a)), droplet effective radii (Fig. 8.2(b)), LWCs (Fig. 8.2(c)), and CDNCs (Fig. 8.2(d)) for the cloud layers of 0 to 30 m, 30 to 70 m, and 70 to 120 m above cloud base. Furthermore, the cloud base heights determined with the dual-FOV lidar measurement are shown in Fig. 8.3(a). The histogram of the cloud vertical extents is presented in Fig. 8.3(b). In cases of additional cloud radar measurements (21 out of 29 cases), the cloud top height was derived with the radar. In the remaining cases, the cloud top height was estimated from the lidar signal measured at 532 nm in the inner FOV. Fig. 8.3(c) displays a histogram of the LWPs. With 26 out of 29 cases, the majority of the performed cloud probings were supported with MWR measurements, which were utilized to derive the LWP. In the remaining cases, the LWP was estimated from the dual-FOV Raman lidar measurements with support of the derived cloud vertical extent. The cloud optical thickness, shown in Fig. 8.3(d), was estimated with the dual-FOV Raman lidar technique under consideration of the derived cloud vertical extent. In Tables 8.2 and 8.3 the minima, maxima, averages, and standard deviations of the mentioned quantities are listed.

The probed clouds were rather thin, which shows a comparison with *Miles et al.* [2000]. The authors compiled properties of continental stratocumuli derived in various measurement campaigns by using airborne in-situ measurements. The clouds which occurred in similar altitudes as the clouds probed in this work had a vertical extent of about 200 to 500 m. A comparison of the other derived cloud properties showed that the obtained values generally match with the results given by *Miles et al.* [2000]. Most clouds in the corresponding altitude range had LWCs of 0.1 to $0.2\,\mathrm{g/m}^3$ and effective cloud droplet radii of 5 to 10 µm. The CDNCs given by *Miles et al.* [2000] tend to be slightly higher with values between 100 and $300\,\mathrm{cm}^{-3}$. However, these values allow only for a rough comparison because most works presented by *Miles et al.* [2000] do not state the cloud penetration depth at which the values were obtained.

8.3 Statistical analysis of aerosol-cloud interactions

This section presents the results of the various statistical analyses about aerosol-cloud relationships performed in this work. Subsection 8.3.1 investigates the correlation between the aerosol extinction coefficient and the CDNC. A similar analysis utilizing the cloud droplet

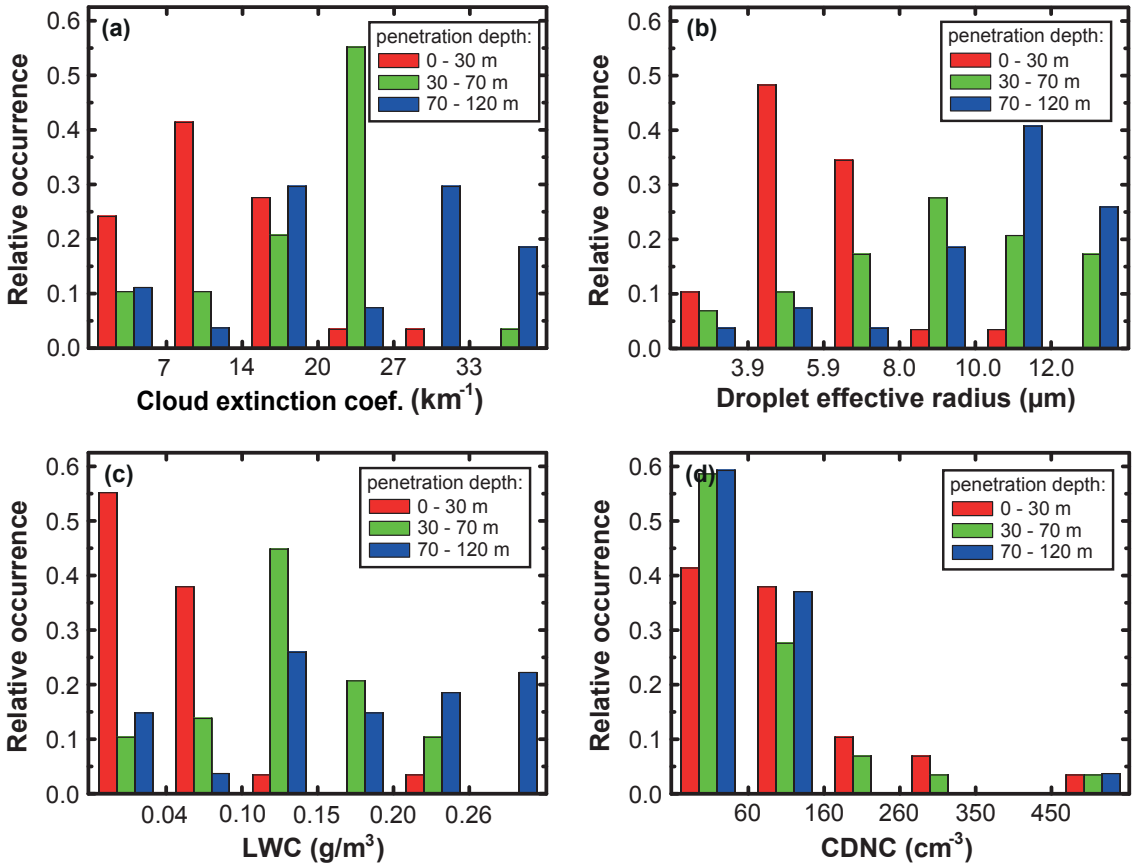

Figure 8.2: Relative occurrence of obtained (a) cloud extinction coefficients, (b) effective droplet radii, (c) LWCs, and (d) CDNCs for penetration depths of 0 to 30 m, 30 to 70 m, and 70 to 120 m.

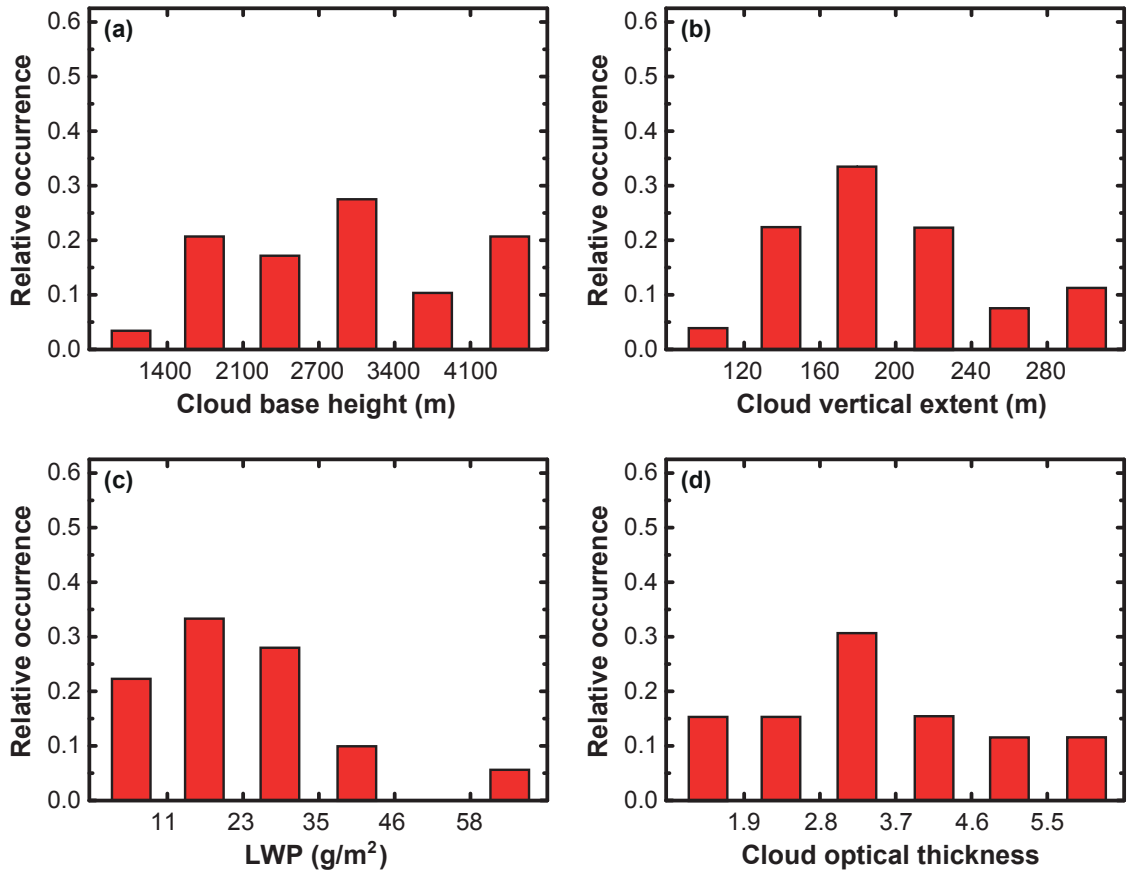

Figure 8.3: Relative occurrence of (a) cloud base heights, (b) cloud vertical extents, (c) LWPs, and (d) cloud optical depths of probed clouds.

Table 8.2: Statistics of derived cloud extinction coefficients, droplet effective radii, LWCs, and CDNCs.

Penetration Depth		0–30 m	30–70 m	70–120 m
Cloud Extinction Coefficient	Minimum (km^{-1})	2.6	3.9	5.1
	Maximum (km^{-1})	28.3	36.3	44.4
	Average (km^{-1})	11.5	19.4	25.5
	Standard deviation (km^{-1})	5.7	7.0	11.4
Droplet Effective Radius	Minimum (µm)	2.7	3.0	2.9
	Maximum (µm)	11.0	14.5	13.8
	Average (µm)	5.8	9.0	10
	Standard deviation (µm)	1.9	3.0	2.6
LWC	Minimum (g/m^3)	0.010	0.012	0.020
	Maximum (g/m^3)	0.213	0.243	0.391
	Average (g/m^3)	0.049	0.124	0.188
	Standard deviation (g/m^3)	0.041	0.063	0.102
CDNC	Minimum (cm^{-3})	10	12	13
	Maximum (cm^{-3})	460	545	496
	Average (cm^{-3})	112	92	72
	Standard deviation (cm^{-3})	102	110	88

Table 8.3: Statistics of derived cloud base heights, cloud vertical extents, LWPs, and cloud optical thicknesses.

Cloud property	Cloud Base Height (m)	Cloud Vertical Extent (m)	LWP (g/m^2)	Cloud Optical Thickness
Minimum	1100	95	5.4	1.5
Maximum	4400	300	64	5.9
Average	2900	190	19	3.6
Standard deviation	910	50	14	1.3

effective radius to quantify the cloud response to a change in aerosol load is performed in Subsection 8.3.2. The dependence of aerosol-cloud relationships on the cloud penetration depth is analyzed in Subsection 8.3.3. The role of the choice of the height range for the aerosol analysis is assessed in Subsection 8.3.4. All of the mentioned studies use cloud properties which were derived without consideration of the vertical wind speed. The influence of the vertical air motion on aerosol-cloud interactions is investigated in Subsection 8.3.5. In Subsection 8.3.6 the obtained results are utilized to estimate the magnitude of the Twomey effect over central Europe.

8.3.1 dependence of CDNC on aerosol extinction coefficient

Figure 8.4 shows derived CDNCs versus aerosol extinction coefficients from 26 dual-FOV Raman lidar measurements. The height range for the aerosol analysis stretches from 300 to 1000 m below cloud base. The CDNC was obtained in a penetration depth from 30 to 70 m.

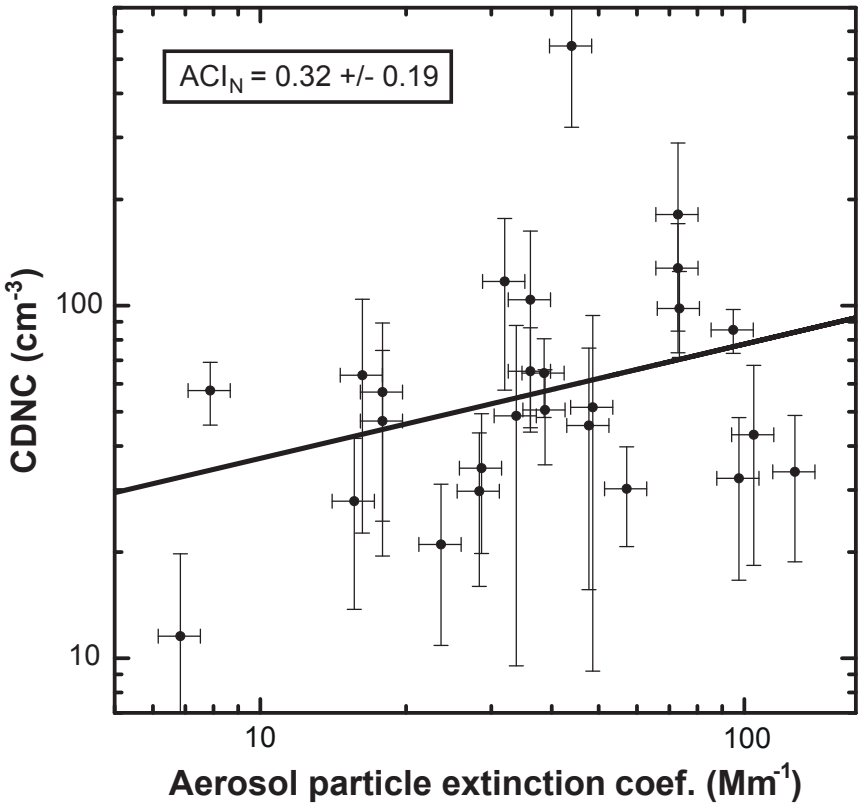

Figure 8.4: CDNC (30 to 70 m above cloud base) versus aerosol particle extinction coefficient (mean value for the 300 to 1000 m layer below cloud base) for 26 dual-FOV Raman lidar probings. Information of up- and downdraft periods is not considered. The linear regression of the data yields $ACI_{\mathrm{N}} = 0.32 \pm 0.19$.

The large variability in the shown data reflects the influence of a multitude of processes on the cloud microphysical properties as discussed in Subsection 2.2.1 and Section 7.3. Nevertheless, a trend in the displayed data is visible. On average, higher CDNCs are found for larger aerosol extinction coefficients. This tendency is expressed in an ACI_{N} value of 0.32 ± 0.19. The relative error is rather high with about 60%. The coefficient of determination obtained from the linear regression for the calculation of ACI_{N} is low with 0.10.

8.3.2 dependence of cloud droplet size on aerosol extinction coefficient

Figure 8.5 shows the results from 26 dual-FOV Raman lidar probings regarding the correlation between cloud droplet effective radius and aerosol particle extinction coefficient. The

height ranges where these quantities were derived are the same as for Fig. 8.4. The measurements were sorted according the obtained LWC (cf. Subsection 2.2.3). Throughout the statistical analyses presented in this section, the LWC grouping was done in such a way that the ranges of the LWC classes correspond to the ranges of the average errors of the obtained LWCs. For the analysis presented in this subsection, two LWC classes are sufficient to cover the dataset. For the classes with the lower and higher LWC, ACI_{r} values of 0.10 ± 0.17 and -0.01 ± 0.09, respectively, were obtained. The average of these values yields the resulting $ACI_{\mathrm{r}} = 0.04 \pm 0.09$. The coefficients of determination from the linear regression of the ACI calculation are 0.03 and 0.00 for the dataset with the lower and higher LWC, respectively. Considering the error ranges of ACI_{N} and ACI_{r}, Eq. (2.6) is fulfilled, stating that ACI_{r} is a third of ACI_{N}.

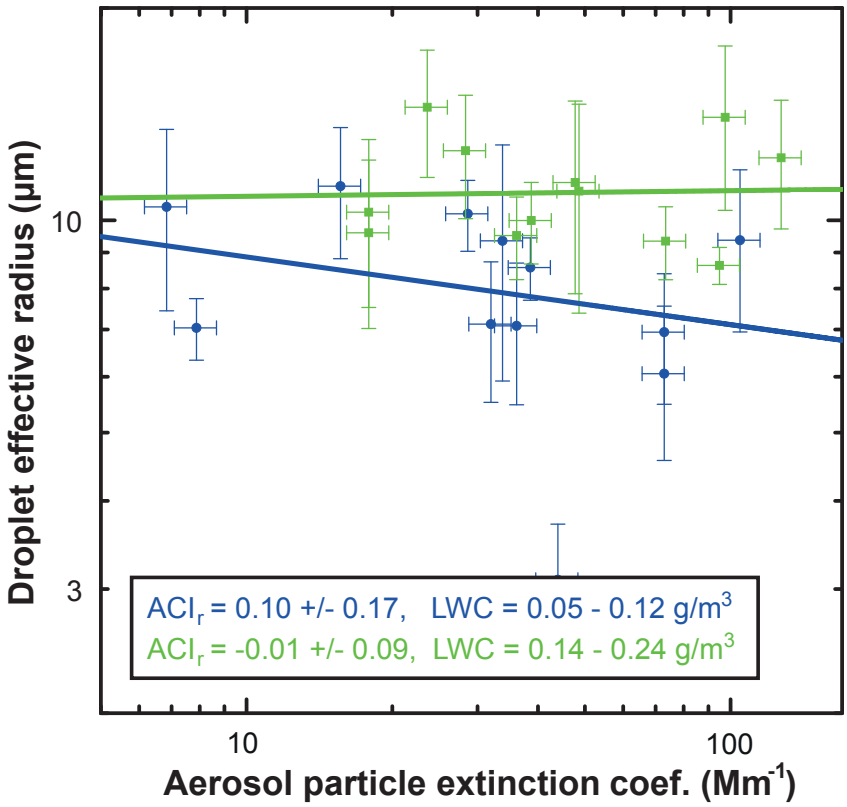

Figure 8.5: Cloud droplet effective radius (30 to 70 m above cloud base) versus aerosol particle extinction coefficient (mean value for the 300 to 1000 m layer below cloud base) without consideration of the vertical wind velocity. The ACI_{r} values of 0.10 ± 0.17 and -0.01 ± 0.09 for the lower and higher LWCs, respectively, yield a mean ACI_{r} value of 0.04 ± 0.09.

8.3.3 dependence of aerosol-cloud interactions on cloud penetration depth

In Subsection 2.2.2 it was explained that aerosol-cloud interactions are strongest at cloud base and diminish with increasing penetration depth due to the effects of other cloud processes. The magnitude of the decrease of aerosol-cloud correlation is important for the investigation of the Twomey effect for which integral cloud properties are required (cf. Subsection 2.2.2). Hence, this subsection deals with the height dependence of the acquired ACI values. An additional motivation for this work is the evaluation of the dual-FOV Raman lidar technique. It is checked whether aerosol-cloud interactions may be observed in the lowest 30 m of the probed clouds as well, despite of possible influences from variations of the cloud base height.

Figure 8.6 presents the datasets for the calculation of the corresponding ACI values for the cloud penetration depths of 0 to 30 m and 70 to 120 m. As aerosol proxy, again the mean extinction coefficient for the layer from 300 to 1000 m below cloud base is taken. The dependence of ACI on penetration depth is summarized in Fig. 8.7. The coefficients of determination from the derivation of ACI_{N} are compared in Fig. 8.8. The coefficients of determination for the ACI_{r} retrievals are not shown, because the number of required LWC groups differs between the penetration depths (cf. Fig. 8.6), which may bias the comparison of the coefficients.

As expected, ACI_{N} as well as ACI_{r} show a decrease from the penetration depth of 30 to 70 m to 70 to 120 m. This decrease is particularly strong in the case of ACI_{N}. The coefficients of determination from the linear regression for the ACI_{N} retrieval show a strong decrease from the penetration depth of 30 to 70 m to 70 to 120 m, too. The CDNC in the height range of 70 to 120 m above cloud base is not correlated at all with the aerosol extinction coefficient below cloud base. These findings show that the magnitude of aerosol-cloud interactions depends on penetration depth and diminishes with increasing distance to cloud base.

The behavior of ACI_{N} and ACI_{r} differs in the lowest 30 m of the investigated clouds. While ACI_{N} is slightly larger for the 30 to 70 m layer, ACI_{r} is even lower than in the 70 to 120 m layer. In Subsection 8.4 it is argued that more emphasis is to be placed on ACI_{N} than on ACI_{r}. These findings illustrate that, in principle, the dual-FOV Raman lidar technique is capable of investigating aerosol-cloud interactions in the lowest 30 m of clouds as well, although the derived results are subject to larger uncertainties.

8.3.4 Dependence of aerosol-cloud interactions on choice of height range for aerosol analysis

In Section 7.1 and Subsection 7.3.3, where case studies about aerosol-cloud relationships are presented, the aerosol particle extinction coefficients were averaged in different height ranges because of differences in the homogeneity of the investigated aerosol layers. This subsection examines the impact of the choice of the height range for the aerosol analysis on the derived ACI values. Therefore, ACI values calculated for three different aerosol analysis height ranges are compared in Figs. 8.9 and 8.10. Besides the standard height range of 300 to 1000 m below cloud base, used in Section 7.1 and Subsection 8.3.1 to 8.3.3, smaller height

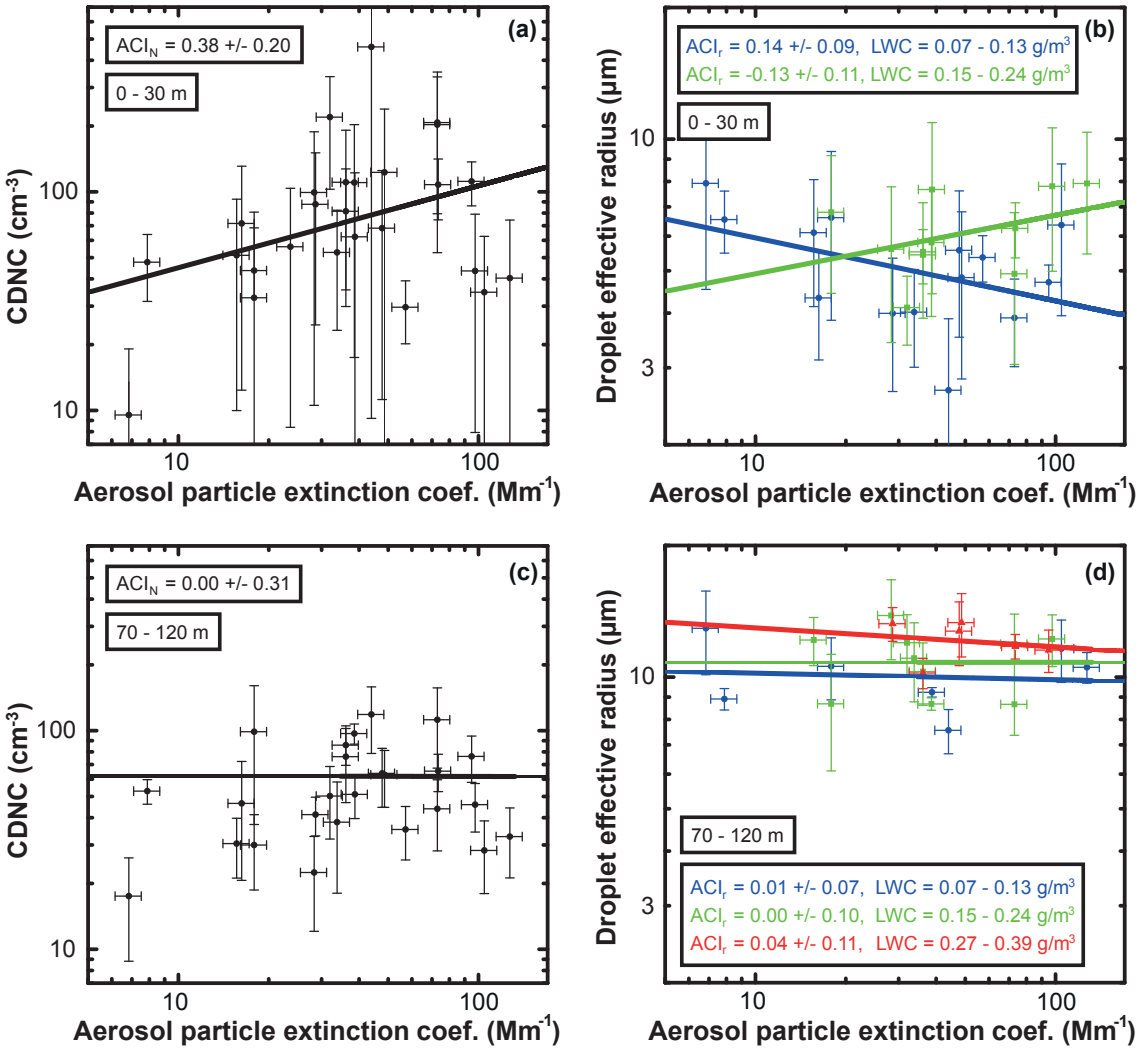

Figure 8.6: CDNC and cloud droplet effective radius versus aerosol particle extinction coefficient (mean value for the 300 to 1000 m layer below cloud base) without consideration of the vertical wind velocity. The cloud properties are shown for the penetration depths of 0 to 30 m (a, b) and 70 to 120 m (c, d). The obtained ACI values are given in the corresponding plots.

ranges of 200 m extent were used to examine whether these layers are more representative for the aerosol load in the cloud. With a distance of 300 and 400 m, respectively, to cloud base, these layers consider approximately the upper third of the standard height range (300 to 1000 m). The upper height limit was varied between 300 and 400 m to check for potentially remaining effects of aerosol growth due to increased humidity in this height.

The ACI values, the corresponding coefficients of determination, and subsequently their dependencies on penetration depth are similar for all selected aerosol layers, when keeping the large error bars in mind. The highest coefficients of correlation are obtained for the aerosol layer 300 to 1000 m below cloud base, especially for the lowest 70 m of the clouds,

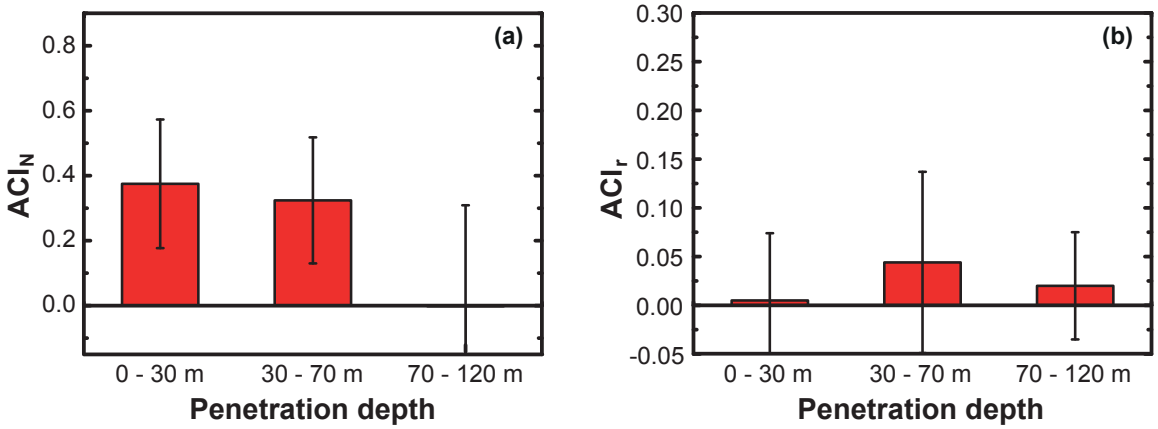

Figure 8.7: (a) ACI_{N} values and (b) ACI_{r} values in dependence of cloud penetration depth without consideration of the vertical wind speed. The aerosol extinction coefficients were derived in the 300 to 1000 m layer below cloud base.

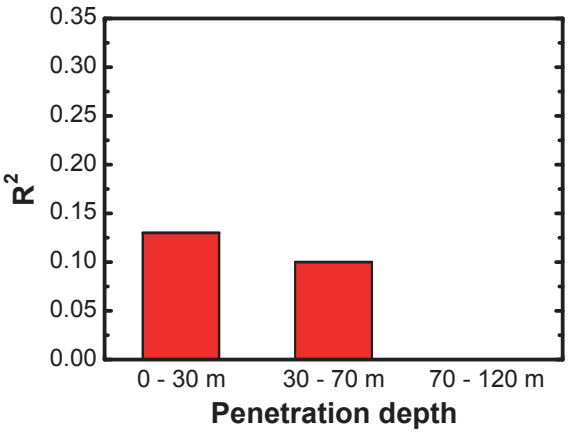

Figure 8.8: Coefficients of determination R^2 from linear regression for the ACI_{N} retrieval of the results displayed in Fig. 8.7. With increasing cloud penetration depth, the correlation between aerosol extinction and CDNC decreases and is zero for the 70 to 120 m cloud layer.

which are most relevant for aerosol-cloud interactions (cf. Subsection 8.3.3). It appears that the 300 to 1000 m aerosol layer below cloud base is more representative for the aerosol load in the cloud. The large vertical extent of 700 m, compared to the 200 m thickness of the other two layers, leads to a better signal-to-noise ratio and diminishes the influence of aerosol structures occurring on smaller vertical scales, which are not correlated with the APNC within the cloud. The analyses employing the aerosol domain of 400 to 600 m below cloud base do not yield higher coefficients of correlation than the corresponding domain 100 m closer to cloud base. Hence, the distance of 300 m between the considered aerosol layer and cloud base seems to be appropriate to avoid effects of the increased humidity below cloud on

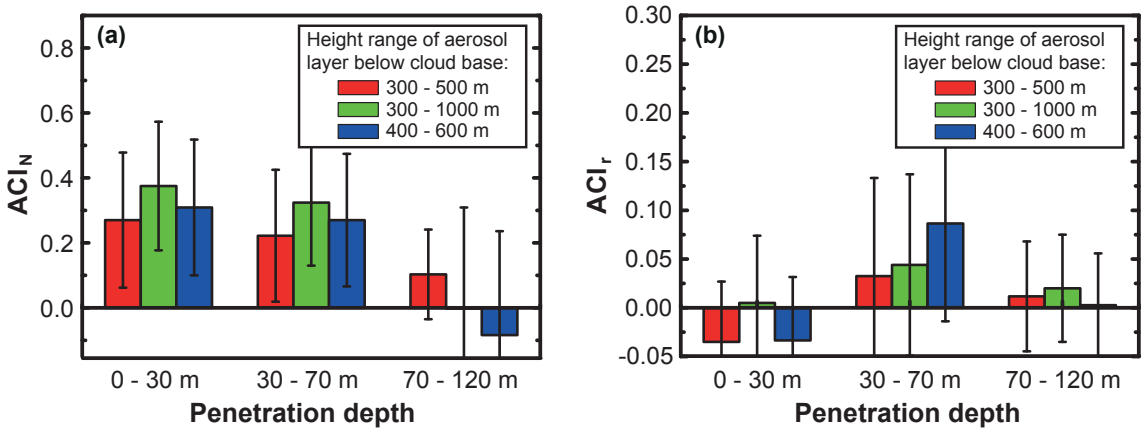

Figure 8.9: (a) ACI_{N} and (b) ACI_{r} for different aerosol-layer height ranges below cloud base used for averaging the aerosol extinction coefficient. The vertical wind speed was not considered in the analyses. The corresponding ACI values as well as their height dependence are similar.

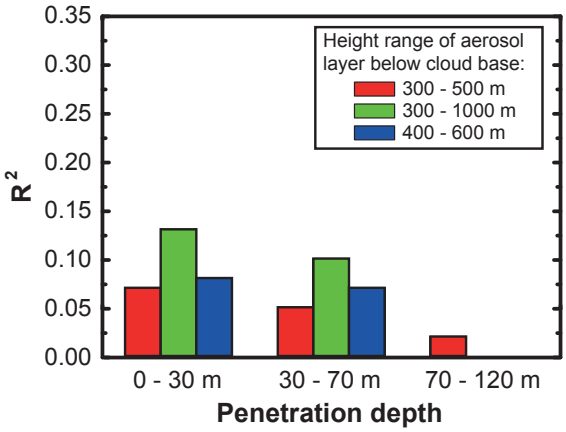

Figure 8.10: Coefficients of determination from linear regression for the ACI_{N} retrieval of the results displayed in Fig. 8.9. The corresponding coefficients as well as their height dependence are similar. The highest correlation between subcloud aerosol extinction and CDNC is obtained when aerosol extinction values for the 300 to 1000 m layer are used.

the statistics. In conclusion, the choice of the aerosol domain of 300 to 1000 m below cloud base is most suitable for studies of aerosol-cloud interactions.

8.3.5 Influence of the vertical wind velocity on aerosol-cloud interactions

Several examples showing the strong influence of the vertical air motion on cloud properties in general and on aerosol-cloud interactions in particular were given in Section 7.3. This subsection investigates the magnitude of aerosol-cloud relationships in dependence of the vertical wind speed on a statistical basis. 13 cases of combined dual-FOV Raman lidar and Doppler wind lidar observations were used for the calculation of ACI values for cloud

updraft regions. The approach explained in Section 7.3 was pursued. The results are shown in Fig. 8.11 and 8.12. However, reasonable ACI values for cloud mean properties (i.e., considering up- and downdraft periods) could not be derived from this dataset because of its reduced extent. Hence, for the comparison of the updraft-dominated cloud regimes with cloud mean properties, the ACI values presented in the previous subsections are used.

Without exception, all ACI values are larger when cloud periods are considered during which the wind lidar indicated a positive vertical wind velocity. This finding points to an enhancement of arosol-cloud interactions due to the increased flow of CCN into clouds during updraft periods. The largest differences between ACI_{N} values occur in the penetration depths of 30 to 70 m and 70 to 120 m.

In the cloud layer from 30 to 70 m above cloud base, the ACI_{N} value for updraft regions is 0.77 ± 0.36 and thus a factor of two larger than the corresponding ACI_{N} value derived without consideration of the vertical wind velocity. The good correlation between the aerosol proxy and CDNC during updraft periods is corroborated by Fig. 8.12. The corresponding coefficient of determination reaches almost a value of 0.3, which is about a factor of three larger than the value derived without consideration of the vertical wind velocity.

For the updraft periods, ACI_{N} is lower in the lowest 30 m above cloud base compared to the values for the 30 to 70 m cloud layer. This finding seems to be in contradiction with the argumentation given in Subsection 2.2.2 and the findings presented in Subsection 8.3.3, which state that aerosol-cloud interactions are most pronounced at cloud base. Furthermore, the corresponding coefficient of determination is lower for the lowest 30 m of the cloud than for the 30 to 70 m layer. Obviously, the results in the lowest 30 m of the clouds are affected by retrieval inaccuracies at the cloud base due to variations of the cloud base height as discussed in Subsections 6.2.1 and 6.2.4. From the trend that ACI_{N} decreases with increasing cloud

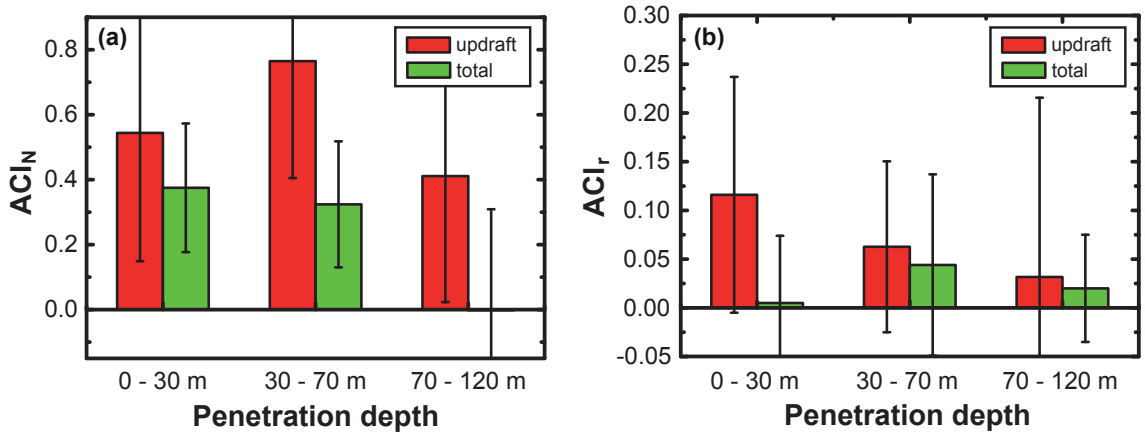

Figure 8.11: (a) ACI_{N} and (b) ACI_{r} considering updraft periods only (red, 13 cases) and ignoring vertical wind information in the ACI retrieval (green, 26 cases). For the aerosol analysis the layer from 300 to 1000 m below cloud base is used.

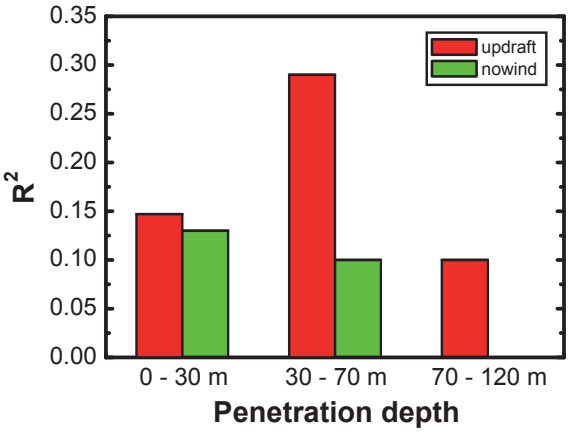

Figure 8.12: Coefficients of determination from linear regression for the ACI_{N} retrieval with (red) and without consideration of the vertical wind speed (green). For all investigated penetration depths, aerosol extinction below cloud and CDNC are more correlated when considering updraft periods only.

penetration depth and the ACI_{N} from the 30 to 70 m cloud layer, $ACI_{\mathrm{N}} = 0.80 \pm 0.40$ can be estimated for cloud updraft regions in the lowermost 70 m above cloud base.

Comparably high ACI values were obtained for updraft regions in the 70 to 120 m cloud layer. This finding may indicate that updrafts are well-organized air parcels that are less affected by entrainment and turbulent mixing, which blur the effects of aerosol-cloud interactions.

It is remarkable that the relative errors of the ACI values derived for cloud updraft regions and cloud mean properties are similar, despite of the significantly larger dataset for the analyses of cloud mean properties. In the lowest 70 m of the clouds, the relative errors of the ACI_{r} values for updrafts and cloud mean properties are 0.60 and 0.57, respectively. The explanation for this finding is the stronger correlation of aerosol and cloud properties in cloud updraft regions (cf. Fig. 8.12).

8.3.6 Twomey effect

In this subsection an attempt is made to estimate the impact of aerosol-cloud interaction on the resulting change in cloud albedo, i.e., the Twomey effect. In Subsection 2.2.4 two approaches were introduced to assess the change of cloud albedo with changing aerosol load. The approach utilizing Eq. (2.12) relies on accurately retrieved cloud optical depths. However, dual-FOV Raman lidar observations assess cloud properties merely up to an optical penetration depth of about 3 (cf. Subsection 5.2.4). To avoid a possible bias by omitting thicker clouds or by considering erroneous optical depth estimates for thicker clouds, another approach is followed.

Equation (2.11) is applied and the ACI_{N} values derived in Section 8.3.3, without consideration of the vertical wind speed (cf. Subsection 2.2.2), are used. As no aerosol-cloud interactions were observed in the penetration depth of 70 to 120 m, we assume that only the lowest 70 m of a cloud are influenced by aerosol-cloud interactions. In this height range an ACI_{N} of 0.35 ± 0.19 was derived (cf. Subsection 8.3.3).

Furthermore, it is assumed that the contribution of a cloud parcel to the cloud albedo is independent of its position relative to cloud top and cloud base. As comparably thin clouds with an average optical thickness of 3.6 are considered here (cf. Table 8.3), this assumption is reasonable [*Lacis and Hansen*, 1974; *Bohren*, 1987; *King*, 1987]. Thus, the overall mean (i.e., total) $ACI_{\mathrm{N}}^{\mathrm{tot}}$ derived from ACI_{N} for the lowermost 70 m of the clouds and the cloud vertical extent can be applied for the estimation of the Twomey effect. In this calculation, the average cloud vertical extent of 190 m (cf. Subsection 8.2.2) is applied. With the use of the average cloud vertical extent (instead of the individual cloud geometrical thicknesses), possible effects of the aerosol on the cloud vertical extent, which influence the cloud albedo as well [*Pincus and Baker*, 1994], are avoided. The derived overall mean $ACI_{\mathrm{N}}^{\mathrm{tot}}$ is 0.13 ± 0.07 (for $ACI_{\mathrm{N}} = 0.35 \pm 0.19$ in 0 to 70 m penetration depth and $ACI_{\mathrm{N}} = 0.00 \pm 0.00$ in 70 to 190 m).

To solve Eq. (2.11), the relative cloud susceptibility over central Germany derived from *Oreopoulos and Platnick* [2008] is used. It is scaled with the average LWC of the cloud height range where aerosol-cloud interactions take place (lowermost 70 m) as described by *Oreopoulos and Platnick* [2008] (cf. Subsection 2.2.4). This average LWC is $0.085 \pm 0.083\,\mathrm{g/m^3}$, which leads to a relative susceptibility of the probed clouds of 0.17 ± 0.17.

Together with the derived $ACI_{\mathrm{N}}^{\mathrm{tot}}$, this yields an estimate of the magnitude of the Twomey effect on layered, thin water clouds over Leipzig, Germany of $CAE = 0.023 \pm 0.026$. This result is used to calculate the Twomey-effect-related radiative forcing for an increase of the APNC by 30%, which is assumed to be the anthropogenic fraction on the global aerosol load, following *Sekiguchi et al.* [2003] and references therein. This radiative forcing is determined to $(-2.8 \pm 3.2)\,\mathrm{W/m^2}$ with an assumed daily mean incoming solar radiation of $400\,\mathrm{W/m^2}$ [*Petty*, 2006]. However, this radiative forcing corresponds to a situation with complete cloud coverage. To estimate the corresponding annual mean radiative forcing over Germany, the annual mean amount of clouds which are susceptible to the Twomey effect is required. These clouds are presumed to be ice-free clouds as ice-containing clouds are influenced by a number of other cloud processes which diminish the impact of the Twomey effect. Here, for a simple, rough estmimation, these clouds are assumed to be low clouds, i.e., clouds occurring below 700 hPa, which corresponds to an altitude of about 3000 m. With an annual mean cloud fraction of about 50% of low clouds over Leipzig [*Xu and Cheng*, 2013], the annual mean radiative forcing due to the Twomey effect caused by anthropogenic aerosol is estimated to $(-1.4 \pm 1.6)\,\mathrm{W/m^2}$ over central Germany. Table 8.4 summarizes the values used for the approach to derive this estimation.

Table 8.4: Obtained and assumed values for the estimation of the anthropogenic radiative forcing due to the Twomey effect over central Germany. Besides $ACI_{\mathrm{N}}^{\mathrm{tot}}$, S_{R}, and CAE, the assumed fraction of anthropogenic aerosol on the global total aerosol load, the annual mean cover of clouds susceptible to the Twomey effect over Leipzig, and the resulting anthropogenic radiative forcing are given.

$ACI_{\mathrm{N}}^{\mathrm{tot}}$	0.13 ± 0.07
S_{R}	0.17 ± 0.17
CAE	0.023 ± 0.026
Anthropogenic aerosol fraction	0.3
Cloud fraction	0.5
Anthropogenic radiative forcing	$(-1.4 \pm 1.6)\,\mathrm{W/m^2}$

8.4 Discussion and conclusions

For the statistical investigation of aerosol-cloud interactions, thin layered clouds were probed over Leipzig, Germany. Their microphysical properties were examined regarding correlations with the aerosol particle extinction coefficient, representing the aerosol load below the cloud. 29 cloud probings were analyzed in total, among this 13 cases with parallel measurements of the vertical wind speed. 26 measurements were analyzed without consideration of the vertical wind speed. The results of the corresponding analyses are summarized and discussed here.

The height range which is most suitable for analyses of aerosol properties for the characterization of the aerosol load within the cloud proved to be the layer from 300 to 1000 m below cloud base. For the quantification of aerosol-cloud relationships the ACI_{N} value had advantages over ACI_{r} despite the higher accuracy of the retrieved cloud droplet size compared to the CDNC (cf. Subsection 6.2.4). The basic advantage comes with the fact that the measurements do not need to be grouped according to LWC. The resulting larger datasets are important for investigations of such complex issues. Some analyses employing ACI_{r} showed opposite behaviors for different LWC classes, i.e., a decrease of droplet size with increasing aerosol load for one class and and an increase for another (e.g., Fig. 8.6). This behavior of ACI_{r} contradicts the impact of aerosol-cloud interactions related to the Twomey effect. The explanation for this finding is that the corresponding datasets are too small for the performed investigations. An alternative explanation relating this findung to other aerosol-cloud interactions which cause this effect is discarded because the setting is considerably influenced from aerosol-cloud interactions related to the Twomey effect. This strong influence is deduced from the comparably high ACI_{N} values (e.g., Fig. 8.6(a) and (b)). Nevertheless, most studies presented in the previous subsections revealed similar behaviors of ACI_{N} and ACI_{r}. The importance of the extent of the dataset was also highlighted in Subsection 8.3.5, where a dataset with only 13 measurements could not be employed for analyses as in the previous subsections.

Significantly stronger aerosol-cloud interactions were found in updraft regions of clouds, which highlights the importance of the vertical wind velocity for aerosol-cloud interactions. The corresponding ACI values derived close to cloud base characterize the microphysical processes of aerosol-cloud interactions and thus follow objective A, explained in Subsection 2.2.2. $ACI_{\mathrm{N}} = 0.80 \pm 0.40$ was derived in the lowest 70 m of clouds probed during updraft time periods. This result corresponds to $ACI_{\mathrm{r}} = 0.27 \pm 0.13$ (cf. Eq. (2.6)), which is compared in the following with results of corresponding airborne in-situ measurements (cf. Table 2.1). Most values match well, i.e., the values obtained by *Martin et al.* [1994], *Gultepe et al.* [1996], *O'Dowd et al.* [1999], *Ramanathan et al.* [2001], *Twohy et al.* [2005], *Zheng et al.* [2011], and *Painemal and Zuidema* [2013]. However, most studies tend to slighty lower values. Furthermore, it has to be mentioned that the cited studies predominantly used probings of marine stratocumuli. ACI values may be higher over oceans than over land, although this issue is currently not well understood. *Lu et al.* [2008] derived $ACI_{\mathrm{r}} = 0.14$ for continental airmasses, whereas an investigation employing the same aircraft with a similar instrumentation yielded $ACI_{\mathrm{r}} = 0.19$ for measurements of marine stratocumuli [*Lu et al.*, 2007]. In summary, the derived ACI_{r} is in good agreement with the investigations cited in Table 2.1.

For the first time, the dependence of aerosol-cloud relationships on cloud penetration depth was investigated. In cloud updraft regions, aerosol-cloud interactions were observed throughout the whole probed height range, whereas aerosol-cloud interactions are restricted to the lowermost 70 m of the clouds in the analyses without consideration of the vertical air motion.

With the height dependence of aerosol-cloud relationships, a cloud vertical mean ACI_{N} of 0.13 ± 0.07 was derived, which leads to $ACI_{\mathrm{r}} = 0.043 \pm 0.023$. This result is assigned to objective B (cf. Subsection 2.2.2) because the cloud vertical mean properties determine the cloud albedo for the observed thin clouds [*Lacis and Hansen*, 1974; *Bohren*, 1987; *King*, 1987] and thus their radiative effect. The result is compared with findings from satellite investigations, which pursue the same objective. The majority of the values given in Table 2.1 matches to the derived result. However, a trend to slightly stronger aerosol-cloud relationships becomes clear. One reason for this difference might be that the majority of the cited satellite investigations consider solely marine clouds, which show an increased Twomey effect [*Quaas et al.*, 2008; *Bellouin et al.*, 2013].

The derived ACI values related to objective A and B differ by almost one order of magnitude. This difference emphasizes the relevance of a clear objective for the conduction of investigations of aerosol-cloud interactions and the importance of the appropriate comprehension of the obtained results.

The magnitude of the Twomey effect on thin, layered clouds over Leipzig, Germany, was estimated to $CAE = 0.023 \pm 0.026$. This result is reasonable as *Painemal and Zuidema* [2013] derived a CAE value of about 0.04 to 0.095 for marine stratocumuli over the Southeast Pacific, where ACI values [*Quaas et al.*, 2008; *Bellouin et al.*, 2013] as well as cloud relative susceptibilities [*Oreopoulos and Platnick*, 2008] are larger than over Europe.

With the derived results, the anthropogenic radiative forcing over central Germany due to the Twomey effect was estimated to approximately $(-1.4 \pm 1.6)\,\mathrm{W/m^2}$. This value matches with the results of the IPCC report 2007, where a radiative forcing of $-0.7\,\mathrm{W/m^2}$ within the error range of $[-0.3,\ -1.8]\,\mathrm{W/m^2}$ was derived [*Forster et al.*, 2007]. However, it should be added that more recent studies tend to derive weaker radiative forcings (e.g., $-0.2 \pm 0.1\,\mathrm{W/m^2}$ [*Quaas et al.*, 2008] and $-0.6 \pm 0.4\,\mathrm{W/m^2}$ [*Bellouin et al.*, 2013]), which fit still reasonably well to the derived result, considering the various assumptions and simplifications in the applied approach.

Chapter 9

Summary

For the first time, the novel dual-FOV Raman lidar technique was implemented and used for investigations of aerosol-cloud interactions in ice-free clouds. With this ground-based remote-sensing method, profiles of several cloud properties can be determined. The dual-FOV technique was installed in the Raman lidar MARTHA, which is operated at TROPOS in Leipzig. Thus, together with the capabilities of conventional multiwavelength Raman lidar methods for high-quality analyses of aerosol properties, MARTHA became a unique instrument for quantitative investigations of aerosol-cloud interactions.

Dual-FOV lidar measurements rely on the simultaneous detection of backscattered light with two FOVs to assess the angular distribution of the forward scattering by cloud droplets. The isotropic molecular Raman backscattering simplifies the data analysis significantly. On the contrary, the small scattering cross sections of Raman scattering events restrict the application of this technique to night time.

With dual-FOV cloud probings, profiles of the extinction coefficient, droplet effective radius, LWC, and CDNC of water clouds can be derived by means of a forward iterative algorithm. An error analyses of the retrieval was presented in the scope of this work. The mentioned cloud properties can be derived up to a geometrical and optical penetration depth of about 150 m and 3, respectively. The temporal resolution of the corresponding measurements is about 3 minutes. The relative errors of the retrieved extinction coefficient and effective radius are about 20% to 25%. The uncertainty of the derived LWC is approximately 30%, whereas the relative error of the CDNC is comparably high with about 60%.

The cloud base height can be determined with dual-FOV lidar measurements with high accuracy. Ambiguities which are caused by aerosol growth due to increased humidity severely affect conventional lidar retrievals of the cloud base height. Here, the higher accuracy of the dual-FOV lidar approach has been demonstrated with simulations and measurements.

Within the scope of this work, aerosol-cloud interactions were investigated with dual-FOV Raman lidar measurements. For this purpose, 29 dual-FOV Raman lidar probings of layered, thin clouds were analyzed regarding aerosol and cloud properties. The cloud probings were performed between September 2010 and August 2012.

Several case studies were discussed. The importance to assess profile information of cloud microphysical properties for investigations of aerosol-cloud interactions was highlighted. Furthermore, it was found by means of additional Doppler wind lidar measurements that the vertical wind velocity has a large influence on cloud properties and thus aerosol-cloud interactions as well.

The statistical analyses of the performed dual-FOV Raman lidar probings showed a trend of cloud droplet size and CDNC with respect to the aerosol load below cloud base. In accordance with aerosol-cloud interactions related to the Twomey effect, the cloud droplet effective radius decreased and CDNC increased with increasing aerosol particle extinction coefficient below cloud base. Moderate coefficients of determination of 0.1 to 0.3 were obtained.

For the first time, the dependence of aerosol-cloud relationships on cloud penetration depth was investigated. The correlation between aerosol and cloud properties was found to be restricted to the lowermost 70 m of the probed clouds. ACI_{N} values (quantifiying aerosol-cloud relationships with regard to CDNC) of 0.38 ± 0.20 and 0.32 ± 0.19 were derived for the height ranges of 0 to 30 m and 30 to 70 m above cloud base, respectively. Furthermore, the effect of the vertical wind velocity on aerosol-cloud relationships was assessed. Throughout the complete analyzed height range within the clouds (0 to 120 m above cloud base), stronger aerosol-cloud relationships were obtained for updraft regions than for cloud regions where up- and downdrafts prevail. For a cloud penetration depth between 30 and 70 m, $ACI_{\mathrm{N}} = 0.77 \pm 0.36$ was obtained, which is about a factor of two larger than the ACI_{N} for cloud mean properties.

From the results of these analyses, conclusions were drawn in regard to two different objectives for the investigation of aerosol-cloud interactions (cf. Subsection 2.2.2). For objective A, the investigation of the microphysical processes of aerosol-cloud interactions, $ACI_{\mathrm{N}} = 0.80 \pm 0.40$ was obtained for cloud updraft regions in the lowermost 70 m of the clouds. This result is in agreement with the findings of airborne in-situ studies (cf. Table 2.1), which follow objective A as well. In pursuit of objective B, the quantification of aerosol-cloud interactions with respect to the clouds' radiative effect, $ACI_{\mathrm{N}} = 0.13 \pm 0.07$ was derived. For this calculation, cloud properties were averaged over the cloud vertical extent and vertical wind velocities were not considered. The results match to the findings of studies employing satellite measurements (cf. Table 2.1), which follow objective B. For the first time, results related to both objective A and B were derived with the same measurement technique. The large difference between the corresponding ACI_{N} values illustrates the high importance to distinguish between these objectives.

Finally, the derived results were used for an estimate of the anthropogenic radiative forcing over central Germany due to the Twomey effect. The result of $(-1.4 \pm 1.6)\,\mathrm{W/m^2}$ matches with the results of the IPCC report 2007 [*Forster et al.*, 2007].

In conclusion, a new measurement technique was introduced, which proved to be very suitable for investigations of aerosol-cloud interactions. The performed studies yielded new insights into aerosol-cloud interactions, which are highly required for an adequate understanding of the earth's climate system.

Bibliography

Ångström, A. (1964), The parameters of atmospheric turbidity, *Tellus*, *16*, doi:10.1111/j.2153-3490.1964.tb00144.x.

Ackerman, A. S., O. B. Toon, D. E. Stevens, A. J. Heymsfield, V. Ramanathan, and E. J. Welton (2000), Reduction of tropical cloudiness by soot, *Science*, *288*, doi:10.1126/science.288.5468.1042.

Ackerman, A. S., M. P. Kirkpatrick, D. E. Stevens, and O. B. Toon (2004), The impact of humidity above stratiform clouds on indirect aerosol climate forcing, *Nature*, *432*, doi:10.1038/nature03174.

Albrecht, B. (1989), Aerosols, cloud microphysics, and fractional cloudiness, *Science*, *245*, doi:10.1126/science.245.4923.1227.

Ansmann, A., and D. Müller (2005), Lidar and atmospheric aerosol particles, in *Lidar – Range-Resolved Optical Remote Sensing of the Atmosphere*, edited by C. Weitkamp, pp. 105–141, Springer, Berlin/Heidelberg.

Ansmann, A., M. Riebesell, and C. Weitkamp (1990), Measurement of atmospheric aerosol extinction profiles with a Raman lidar, *Opt. Lett.*, *15*, doi:10.1364/OL.15.000746.

Ansmann, A., U. Wandinger, M. Riebesell, C. Weitkamp, and W. Michaelis (1992a), Independent measurement of extinction and backscatter profiles in cirrus clouds by using a combined Raman elastic-backscatter lidar, *Appl. Opt.*, *31*, doi:10.1364/AO.31.007113.

Ansmann, A., M. Tesche, P. Seifert, S. Groß, V. Freudenthaler, A. Apituley, K. M. Wilson, I. Serikov, H. Linne, B. Heinold, A. Hiebsch, F. Schnell, J. Schmidt, I. Mattis, U. Wandinger, and M. Wiegner (2011), Ash and fine-mode particle mass profiles from EARLINET–AERONET observations over central Europe after the eruptions of the Eyjafjallajökull volcano in 2010, *J. Geophys. Res.*, *116*, doi:10.1029/2010JD015567.

Antuna, J., E. Landulfo, B. Clemesha, F. Zaratti, E. Quel, A. Bastidas, R. Estevan, and B. Barja (2012), Lidar community in Latin America: A decade of challenges and successes, in *Proceedings of the 26th International Laser Radar Conference*, Porto Heli, Greece.

Arshinov, Y., S. Bobrovnikov, I. Serikov, A. Ansmann, U. Wandinger, D. Althausen, I. Mattis, and D. Müller (2005), Daytime operation of a pure rotational Raman lidar by use of a Fabry-Perot interferometer, *Appl. Opt.*, *44*, doi:10.1364/AO.44.003593.

Asmi, E., E. Freney, M. Hervo, D. Picard, C. Rose, A. Colomb, and K. Sellegri (2012), Aerosol cloud activation in summer and winter at Puy-de-Dome high altitude site in France, *Atmos. Chem. Phys.*, *12*, doi:10.5194/acp-12-11589-2012.

Bellouin, N., J. Quaas, J. J. Morcrette, and O. Boucher (2013), Estimates of aerosol radiative forcing from the MACC re-analysis, *Atmos. Chem. Phys.*, *13*, doi:10.5194/acp-13-2045-2013.

Betz, G., N. Brachatzek, S. Cacean, K. Güssow, J. Heintzenberg, S. Hiller, C. Hoose, G. Kleppner, T. Leisner, A. Oschlies, U. Platt, A. Proelss, O. Renn, W. Rickels, S. Schäfer, and M. Zürn (2011), *Gezielte Eingriffe in das Klima? Eine Bestandsaufnahme der Debatte zu Climate Engineering*, Kiel Earth Institute.

Bissonnette, L. R. (1996), Multiple-scattering lidar equation, *Appl. Opt.*, *35*, doi:10.1364/AO.35.006449.

Bissonnette, L. R., and D. L. Hutt (1995), Multiply scattered aerosol lidar returns: Inversion method and comparison with in situ measurements, *Appl. Opt.*, *34*, 6959–6975.

Bissonnette, L. R., G. Roy, L. Poutier, S. G. Cober, and G. A. Isaac (2002), Multiple-scattering lidar retrieval method: Tests on Monte Carlo simulations and comparisons with in situ measurements, *Appl. Opt.*, *41*, 6307–6324.

Bissonnette, L. R., G. Roy, and N. Roy (2005), Multiple-scattering-based lidar retrieval: Method and results of cloud probings, *Appl. Opt.*, *44*, doi:http://dx.doi.org/10.1364/AO.44.005565.

Böckmann, C., U. Wandinger, A. Ansmann, J. Bösenberg, V. Amiridis, A. Boselli, A. Delaval, F. De Tomasi, M. Frioud, I. Grigorov, A. Hagard, M. Horvat, M. Iarlori, L. Komguem, S. Kreipl, G. Larchevque, V. Matthias, A. Papayannis, G. Pappalardo, F. Rocadenbosch, J. Rodrigues, J. Schneider, V. Shcherbakov, and M. Wiegner (2004), Aerosol lidar intercomparison in the framework of the EARLINET project. 2. Aerosol backscatter algorithms, *Appl. Opt.*, *43*, doi:10.1364/AO.43.000977.

Bohren, C. F. (1987), Multiple scattering of light and some of its observable consequences, *Am. J. Phys.*, *55*, doi:http://dx.doi.org/10.1119/1.15109.

Bösenberg et al. (2003), EARLINET: A European Aerosol Research Lidar Network to Establish an Aerosol Climatology, in *MPI Rep. 348*, Max-Planck-Inst. für Meteorol., Hamburg, Germany.

Brandau, C. L., H. W. J. Russchenberg, and W. H. Knap (2010), Evaluation of ground-based remotely sensed liquid water cloud properties using shortwave radiation measurements, *Atmos. Res.*, *96*, doi:10.1016/j.atmosres.2010.01.009, 15th International Conference on Clouds and Precipitation, Cancun, Mexico.

Brenguier, J. L., H. Pawlowska, and L. Schüller (2003), Cloud microphysical and radiative properties for parameterization and satellite monitoring of the indirect effect of aerosol on climate, *J. Geophys. Res.*, *108*, doi:10.1029/2002JD002682.

Bréon, F., D. Tanré, and S. Generoso (2002), Aerosol effect on cloud droplet size monitored from satellite, *Science*, *295*, doi:10.1126/science.1066434.

Bucholtz, A. (1995), Rayleigh-scattering calculations for the terrestrial atmosphere, *Appl. Opt.*, *34*, doi:10.1364/AO.34.002765.

Bühl, J., R. Engelmann, and A. Ansmann (2012), Removing the laser-chirp influence from coherent Doppler lidar datasets by two-dimensional deconvolution, *J. Atmos. Oceanic Technol.*, *29*, 1042–1051.

Bulgin, C. E., P. I. Palmer, G. E. Thomas, C. P. G. Arnold, E. Campmany, E. Carboni, R. G. Grainger, C. Poulsen, R. Siddans, and B. N. Lawrence (2008), Regional and seasonal variations of the Twomey indirect effect as observed by the ATSR-2 satellite instrument, *Geophys. Res. Lett.*, *35*, doi:10.1029/2007GL031394.

Cahalan, R., M. McGill, J. Kolasinski, T. Varnai, and K. Yetzer (2005), THOR - Cloud thickness from offbeam lidar returns, *J. Atmos. Oceanic Technol.*, *22*, doi:10.1175/JTECH1740.1.

Chameides, W., C. Luo, R. Saylor, D. Streets, Y. Huang, M. Bergin, and F. Giorgi (2002), Correlation between model-calculated anthropogenic aerosols and satellite-derived cloud optical depths: Indication of indirect effect?, *J. Geophys. Res.*, *107*, doi:10.1029/2000JD000208.

Cimini, D., and E. R. Westwater (2010), Principles of radiometric remote sensing of the Troposphere, in *Integrated ground-based observing systems*, edited by D. Cimini, F. S. Marzano, and G. Visconti, pp. 3–32, Springer, Berlin/Heidelberg.

Cohard, J. M., and J. P. Pinty (2000), A comprehensive two-moment warm microphysical bulk scheme. I: Description and tests, *Q. J. Roy. Meteorol. Soc.*, *126*, doi:10.1256/smsqj.56613.

Collis, R. T. H., and P. B. Russel (1976), Lidar measurement of particles and gases by elastic backscattering and differential absorption, in *Laser Monitoring of the Atmosphere*, edited by E. D. Hinkley, pp. 71–151, Springer, Berlin/Heidelberg.

Costantino, L., and F. M. Bréon (2013), Aerosol indirect effect on warm clouds over South-East Atlantic, from co-located MODIS and CALIPSO observations, *Atmos. Chem. Phys.*, *13*, doi:10.5194/acp-13-69-2013.

Crewell, S., and U. Löhnert (2003), Accuracy of cloud liquid water path from ground-based microwave radiometry 2. Sensor accuracy and synergy, *Radio Sci.*, *38*, doi:10.1029/2002RS002634.

Deirmendjian, D. (1969), *Electromagnetic Scattering on Spherical Polydispersions*, Elsevier, New York, 290 S.

DeMott, P. J., A. J. Prenni, X. Liu, S. M. Kreidenweis, M. D. Petters, C. H. Twohy, M. S. Richardson, T. Eidhammer, and D. C. Rogers (2010), Predicting global atmospheric ice nuclei distributions and their impacts on climate, *Proceedings of the National Academy of Sciences of the United States of America*, *107*, doi:10.1073/pnas.0910818107.

Ditas, F., R. A. Shaw, H. Siebert, M. Simmel, B. Wehner, and A. Wiedensohler (2012), Aerosols-cloud microphysics-thermodynamics-turbulence: Evaluating supersaturation in a marine stratocumulus cloud, *Atmos. Chem. Phys.*, *12*, doi:10.5194/acp-12-2459-2012.

Donovan, D., J. Whiteway, and A. Carswell (1993), Correction for nonlinear photon-counting effects in lidar systems, *Appl. Opt.*, *32*, 6742–6753.

Draxler, R. R., and G. D. Rolph (2013), HYSPLIT (HYbrid Single-Particle Lagrangian Integrated Trajectory) model access via NOAA ARL READY Website (http://ready.arl.noaa.gov/HYSPLIT.php), NOAA Air Resources Laboratory, Silver Spring, MD.

Dusek, U., G. Frank, L. Hildebrandt, J. Curtius, J. Schneider, S. Walter, D. Chand, F. Drewnick, S. Hings, D. Jung, S. Borrmann, and M. Andreae (2006), Size matters more than chemistry for cloud-nucleating ability of aerosol particles, *Science*, *312*, doi:10.1126/science.1125261.

Ebell, K., S. Crewell, U. Löhnert, D. D. Turner, and E. J. O'Connor (2011), Cloud statistics and cloud radiative effect for a low-mountain site, *Q. J. Roy. Meteor. Soc.*, *137*, doi:10.1002/qj.748.

Eidhammer, T., P. J. DeMott, A. J. Prenni, M. D. Petters, C. H. Twohy, D. C. Rogers, J. Stith, A. Heymsfield, Z. Wang, K. A. Pratt, K. A. Prather, S. M. Murphy, J. H. Seinfeld, R. Subramanian, and S. M. Kreidenweis (2010), Ice initiation by aerosol particles: Measured and predicted ice nuclei concentrations versus measured ice crystal concentrations in an orographic wave cloud, *J. Atmos. Sci.*, *67*, doi:10.1175/2010JAS3266.1.

Engelmann, R., U. Wandinger, A. Ansmann, D. Mueller, E. Zeromskis, D. Althausen, and B. Wehner (2008), Lidar observations of the vertical aerosol flux in the planetary boundary

layer, *J. Atmos. Oceanic Technol.*, *25*, doi:10.1175/2007JTECHA967.1, 7th International Symposium on Tropospheric Profiling, Boulder, USA, 2006.

Ervens, B., G. Feingold, and S. Kreidenweis (2005), Influence of water-soluble organic carbon on cloud drop number concentration, *J. Geophys. Res.*, *110*, doi:10.1029/2004JD005634.

Feingold, G., L. Remer, J. Ramaprasad, and Y. Kaufman (2001), Analysis of smoke impact on clouds in Brazilian biomass burning regions: An extension of Twomey's approach, *J. Geophys. Res.*, *106*, doi:10.1029/2001JD000732.

Feingold, G., L. E. Wynn, D. E. Veron, and M. Previdi (2003), First measurements of the Twomey indirect effect using ground-based remote sensors, *Geophys. Res. Lett.*, *30*, doi: 10.1029/2002GL016633.

Fernald, F. G. (1984), Analysis of atmospheric lidar observations - some comments, *Appl. Opt.*, *23*(5), doi:10.1364/AO.23.000652.

Field, P. R., A. J. Heymsfield, B. J. Shipway, P. J. DeMott, K. A. Pratt, D. C. Rogers, J. Stith, and K. A. Prather (2011), Ice in Clouds Experiment-Layer Clouds. Part II: Testing characteristics of heterogeneous ice formation in lee wave clouds, *J. Atmos. Sci.*, *69*, doi:10.1175/JAS-D-11-026.1.

Forster, P., V. Ramaswamy, P. Artaxo, T. Berntsen, R. Betts, D. Fahey, J. Haywood, J. Lean, D. Lowe, G. Myhre, J. Nganga, R. Prinn, G. Raga, M. Schulz, and R. V. Dorland (2007), Changes in atmospheric constituents and in radiative forcing, in *Climate Change 2007 - The Physical Science Basis. Contribution of Working Group I to the Fourth Assessment Report of the Intergovernmental Panel on Climate Change*, edited by S. Solomon, D. Qin, M. Manning, Z. Chen, M. Marquis, K. Averyt, M.Tignor, and H. Miller, pp. 129–234, Cambridge University Press, Cambridge/New York.

Freudenthaler, V. (2004), Effects of spatially inhomogeneous photomultiplier sensitivity on lidar signals and remedies, in *Proceedings of the 22nd International Laser Radar Conference*, Matera, Italy, 12-16 July 2008.

Freudenthaler, V. (2008), The Telecover Test: A quality assurance tool for the optical part of a Lidar system, in *Proceedings of the 24th International Laser Radar Conference*, Boulder, USA, 23-27 June 2008.

Fridlind, A. M., A. S. Ackerman, G. McFarquhar, G. Zhang, M. R. Poellot, P. J. DeMott, A. J. Prenni, and A. J. Heymsfield (2007), Ice properties of single-layer stratocumulus during the Mixed-Phase Arctic Cloud Experiment: 2. Model results, *J. Geophys. Res.*, *112*, doi:10.1029/2007JD008646.

Frisch, S., M. Shupe, I. Djalalova, G. Feingold, and M. Poellot (2002), The retrieval of stratus cloud droplet effective radius with cloud radars, *J. Atmos. Oceanic Tech.*, *19*,

doi:10.1175/1520-0426(2002)019⟨0835:TROSCD⟩2.0.CO;2, 5th International Symposium on Tropospheric Profiling, Adelaide, Australia.

Garrett, T., C. Zhao, X. Dong, G. Mace, and P. Hobbs (2004), Effects of varying aerosol regimes on low-level Arctic stratus, *Geophys. Res. Lett.*, *31*, doi:10.1029/2004GL019928.

Gasso, S., D. Hegg, D. Covert, D. Collins, K. Noone, E. Ostrom, B. Schmid, P. Russell, J. Livingston, P. Durkee, and H. Jonsson (2000), Influence of humidity on the aerosol scattering coefficient and its effect on the upwelling radiance during ACE-2, *Tellus*, *52*, doi:10.1034/j.1600-0889.2000.00055.x.

Gaussiat, N., R. J. Hogan, and A. J. Illingworth (2007), Accurate liquid water path retrieval from low-cost microwave radiometers using additional information from a lidar ceilometer and operational forecast models, *J. Atmos. Oceanic Technol.*, *24*, doi:http://dx.doi.org/10.1175/JTECH2053.1.

Gultepe, I., G. Isaac, W. Leaitch, and C. Banic (1996), Parameterizations of marine stratus microphysics based on in situ observations: Implications for GCMs, *J. Climate*, *9*, doi:10.1175/1520-0442(1996)009⟨0345:POMSMB⟩2.0.CO;2.

Guo, H., J. E. Penner, M. Herzog, and S. Xie (2007), Investigation of the first and second aerosol indirect effects using data from the May 2003 Intensive Operational Period at the Southern Great Plains, *J. Geophys. Res.*, *112*, doi:10.1029/2006JD007173.

Han, Q. Y., W. B. Rossow, J. Zeng, and R. Welch (2002), Three different behaviors of liquid water path of water clouds in aerosol-cloud interactions, *J. Atmos. Sci.*, *59*, doi:10.1175/1520-0469(2002)059⟨0726:TDBOLW⟩2.0.CO;2.

Hänel, G. (1976), The properties of atmospheric aerosol particles as functions of the relative humidity at thermodynamic equilibrium with the surrounding moist air, pp. 74–188, Academic Press, New York/London.

Hegerl, G. C., F. W. Zwiers, P. Braconnot, N. Gillett, Y. Luo, J. A. M. Orsini, N. Nicholls, J. E. Penner, and P. A. Stott (2007), Understanding and Attributing Climate Change, in *Climate Change 2007 - The Physical Science Basis. Contribution of Working Group I to the Fourth Assessment Report of the Intergovernmental Panel on Climate Change*, edited by S. Solomon, D. Qin, M. Manning, Z. Chen, M. Marquis, K. Averyt, M.Tignor, and H. Miller, pp. 663–745, Cambridge University Press, Cambridge/New York.

Heintzenberg, J., and B. J. Charlson (2009), *Clouds in the perturbed climate system: Their relationship to energy balance, atmospheric dynamics, and precipitation*, MIT Press.

Holben, B., T. Eck, I. Slutsker, D. Tanré, J. Buis, A. Setzer, E. Vermote, J. Reagan, Y. Kaufman, T. Nakajima, F. Lavenu, I. Jankowiak, and A. Smirnov (1998), AERONET - A federated instrument network and data archive for aerosol characterization, *Remote Sens. Environ.*, *66*, doi:10.1016/S0034-4257(98)00031-5.

Holben, B. N., D. Tanré, A. Smirnov, T. F. Eck, I. Slutsker, N. Abuhassan, W. W. Newcomb, J. S. Schafer, B. Chatenet, F. Lavenu, Y. J. Kaufman, J. V. Castle, A. Setzer, B. Markham, D. Clark, R. Frouin, R. Halthore, A. Karneli, N. T. O'Neill, C. Pietras, R. T. Pinker, K. Voss, and G. Zibordi (2001), An emerging ground-based aerosol climatology: Aerosol optical depth from AERONET, *J. Geophys. Res.*, *106*, doi:10.1029/2001JD900014.

Hu, Y., Z. Liu, D. Winker, M. Vaughan, V. Noel, L. Bissonnette, G. Roy, and M. McGill (2006), Simple relation between lidar multiple scattering and depolarization for water clouds, *Opt. Lett.*, *31*, doi:10.1364/OL.31.001809.

Illingworth, A. J., R. J. Hogan, E. J. O'Connor, D. Bouniol, M. E. Brooks, J. Delanoe, D. P. Donovan, J. D. Eastment, N. Gaussiat, J. W. F. Goddard, M. Haeffelin, H. K. Baltink, O. A. Krasnov, J. Pelon, J.-M. Piriou, A. Protat, H. W. J. Russchenberg, A. Seifert, A. M. Tompkins, G.-J. van Zadelhoff, F. Vinit, U. Willen, D. R. Wilson, and C. L. Wrench (2007), Cloudnet - Continuous evaluation of cloud profiles in seven operational models using ground-based observations, *Bull. Am. Meteorol. Soc.*, *88*, doi:10.1175/BAMS-88-6-883.

IPCC (2007), Summary for Policymakers, in *Climate change 2007: Impacts, adaptation and vulnerability. Contribution of Working Group II to the Fourth Assessment Report of the Intergovernmental Panel on Climate Change*, M. L. Parry, O. F. Canziani, J. P. Palutikof, P. J. van der Linden and C. E. Hanson, Cambridge University Press, Cambridge.

Kanamitsu, M. (1989), Description of the NMC Global Data Assimilation and Forecast System, *Weather and Forecasting*, *4*, doi:http://dx.doi.org/10.1175/1520-0434(1989)004⟨0335:DOTNGD⟩2.0.CO;2.

Kanitz, T., P. Seifert, A. Ansmann, R. Engelmann, D. Althausen, C. Casiccia, and E. G. Rohwer (2011), Contrasting the impact of aerosols at northern and southern midlatitudes on heterogeneous ice formation, *Geophys. Res. Lett.*, *38*, doi:10.1029/2011GL048532.

Katz, J. I. (2010), Stratospheric albedo modification, *Energy Environ. Sci.*, *3*, doi:10.1039/c002441d.

Kaufman, Y., I. Koren, L. Remer, D. Rosenfeld, and Y. Rudich (2005), The effect of smoke, dust, and pollution aerosol on shallow cloud development over the Atlantic Ocean, *Proceedings of the National Academy of Sciences of the United States of America*, *102*, doi:10.1073/pnas.0505191102.

Kaufman, Y. J., and R. S. Fraser (1997), The effect of smoke particles on clouds and climate forcing, *Science*, *277*, doi:10.1126/science.277.5332.1636.

Khairoutdinov, M., and Y. Kogan (2000), A new cloud physics parameterization in a large-eddy simulation model of marine stratocumulus, *Mon. Weather Rev.*, *128*, doi:10.1175/1520-0493(2000)128⟨0229:ANCPPI⟩2.0.CO;2.

Kim, B., M. A. Miller, S. E. Schwartz, Y. Liu, and Q. Min (2008), The role of adiabaticity in the aerosol first indirect effect, *J. Geophys. Res.*, *113*, doi:10.1029/2007JD008961.

Kim, B.-G., S. E. Schwartz, M. A. Miller, and Q. Min (2003), Effective radius of cloud droplets by ground-based remote sensing: Relationship to aerosol, *J. Geophys. Res.*, *108*, doi:10.1029/2003JD003721.

King, M. D. (1987), Determination of the scaled optical thickness of clouds from reflected solar radiation measurements, *J. Atmos. Sci.*, *44*, doi:http://dx.doi.org/10.1175/1520-0469(1987)044⟨1734:DOTSOT⟩2.0.CO;2.

Kleinman, L. I., P. H. Daum, Y. N. Lee, E. R. Lewis, A. J. Sedlacek, G. I. Senum, S. R. Springston, III, J. Wang, J. Hubbe, J. Jayne, Q. Min, S. S. Yum, and G. Allen (2012), Aerosol concentration and size distribution measured below, in, and above cloud from the DOE G-1 during VOCALS-REx, *Atmos. Chem. Phys.*, *12*, doi:10.5194/acp-12-207-2012.

Klett, J. (1981), Stable analytical inversion solution for processing lidar returns, *Appl. Opt.*, *20*, doi:10.1364/AO.20.000211.

Kolgotin, A., and D. Müller (2008), Theory of inversion with two-dimensional regularization: Profiles of microphysical particle properties derived from multiwavelength lidar measurements, *Appl. Opt.*, *47*, doi:10.1364/AO.47.004472.

Lacis, A. A., and J. E. Hansen (1974), Parameterization for absorption of solar radiation in the earth's atmosphere, *J. Atmos. Sci.*, *31*, doi:10.1175/1520-0469(1974)031⟨0118:APFTAO⟩2.0.CO;2.

Latham, J., K. Bower, T. Choularton, H. Coe, P. Connolly, G. Cooper, T. Craft, J. Foster, A. Gadian, L. Galbraith, H. Iacovides, D. Johnston, B. Launder, B. Leslie, J. Meyer, A. Neukermans, B. Ormond, B. Parkes, P. Rasch, J. Rush, S. Salter, T. Stevenson, H. Wang, Q. Wang, and R. Wood (2012), Marine cloud brightening, *Phil. Trans. R. Soc. A*, *370*, doi:10.1098/rsta.2012.0086.

Leaitch, W., C. Banic, G. Isaac, M. Couture, P. Liu, I. Gultepe, S. Li, L. Kleinman, P. Daum, and J. MacPherson (1996), Physical and chemical observations in marine stratus during the 1993 North Atlantic Regional Experiment: Factors controlling cloud droplet number concentrations, *J. Geophys. Res.*, *101*, doi:10.1029/96JD01228.

Lebsock, M. D., G. L. Stephens, and C. Kummerow (2008), Multisensor satellite observations of aerosol effects on warm clouds, *J. Geophys. Res.*, *113*, doi:10.1029/2008JD009876.

Liu, Y., and P. Daum (2002), Anthropogenic aerosols – Indirect warming effect from dispersion forcing, *Nature*, *419*, doi:10.1038/419580a.

Liu, Y. G., and P. H. Daum (2004), Parameterization of the autoconversion process. Part I: Analytical formulation of the Kessler-type parameterizations, *J. Atmos. Sci.*, *61*, doi:10.1175/1520-0469(2004)061⟨1539:POTAPI⟩2.0.CO;2.

Lohmann, U., J. Quaas, S. Kinne, and J. Feichter (2007), Different approaches for constraining global climate models of the anthropogenic indirect aerosol effect, *Bull. Am. Meteorol. Soc.*, *88*, doi:10.1175/BAMS-88-2-243, Specialty Conference on the Indirect Effect of Aerosols on Climate, Manchester, England.

Löhnert, U., and O. Maier (2012), Operational profiling of temperature using ground-based microwave radiometry at Payerne: Prospects and challenges, *Atmos. Meas. Tech.*, *5*, doi:10.5194/amt-5-1121-2012.

Löhnert, U., S. Crewell, and C. Simmer (2004), An integrated approach toward retrieving physically consistent profiles of temperature, humidity, and cloud liquid water, *J. Appl. Meteorol.*, *43*, doi:10.1175/1520-0450(2004)043⟨1295:AIATRP⟩2.0.CO;2.

Love, S. P., A. B. Davis, C. Ho, and C. A. Rohde (2001), Remote sensing of cloud thickness and liquid water content with Wide-Angle Imaging Lidar, *Atm. Res.*, *59*, doi:10.1016/S0169-8095(01)00121-1, 13th International Conference on Clouds and Precipitation, Reno, USA.

Lu, M. L., and J. H. Seinfeld (2005), Study of the aerosol indirect effect by large-eddy simulation of marine stratocumulus, *J. Atmos. Sci.*, *62*, doi:10.1175/JAS3584.1.

Lu, M. L., and J. H. Seinfeld (2006), Effect of aerosol number concentration on cloud droplet dispersion: A large-eddy simulation study and implications for aerosol indirect forcing, *J. Geophys. Res.*, *111*, doi:10.1029/2005JD006419.

Lu, M.-L., G. Feingold, H. H. Jonsson, P. Y. Chuang, H. Gates, R. C. Flagan, and J. H. Seinfeld (2008), Aerosol-cloud relationships in continental shallow cumulus, *J. Geophys. Res.*, *113*, doi:10.1029/2007JD009354.

Lu, M.-L., W. C. Conant, H. H. Jonsson, V. Varutbangkul, R. C. Flagan, and J. H. Seinfeld (2007), The Marine Stratus/Stratocumulus Experiment (MASE): Aerosol-cloud relationships in marine stratocumulus, *J. Geophys. Res.*, *112*, doi:10.1029/2006JD007985.

Malinka, A. V., and J. Schmidt (2010), Overlap function of a lidar with a field stop shifted from the focal plane, in *Proceedings of the 25nd International Laser Radar Conference (ILRC)*, St. Petersburg, Russia, 5-9 July 2010.

Malinka, A. V., and E. P. Zege (2003), Analytical modeling of Raman lidar return, including multiple scattering, *Appl. Opt.*, *42*, doi:http://dx.doi.org/10.1364/AO.42.001075.

Malinka, A. V., and E. P. Zege (2007), Possibilities of warm cloud microstructure profiling with multiple-field-of-view Raman lidar, *Appl. Opt.*, *46*, doi:http://dx.doi.org/10.1364/AO.46.008419.

Martin, G. M., D. W. Johnson, and A. Spice (1994), The measurement and parameterization of effective radius of droplets in warm stratocumulus clouds, *J. Atmos. Sci.*, *51*, doi:10.1175/1520-0469(1994)051⟨1823:TMAPOE⟩2.0.CO;2.

Martucci, G., and C. D. O'Dowd (2011), Ground-based retrieval of continental and marine warm cloud microphysics, *Atmos. Meas. Tech.*, *4*, doi:10.5194/amt-4-2749-2011.

Matthais, V., V. Freudenthaler, A. Amodeo, I. Balin, D. Balis, J. Bösenberg, A. Chaikovsky, G. Chourdakis, A. Comeron, A. Delaval, F. De Tomasi, R. Eixmann, A. Hagard, L. Komguem, S. Kreipl, R. Matthey, V. Rizi, J. Rodrigues, U. Wandinger, and X. Wang (2004), Aerosol lidar intercomparison in the framework of the EARLINET project. 1. Instruments, *Appl. Opt.*, *43*, doi:10.1364/AO.43.000961.

Mattis, I., A. Ansmann, D. Althausen, V. Jaenisch, U. Wandinger, D. Müller, Y. F. Arshinov, S. M. Bobrovnikov, and I. B. Serikov (2002), Relative-humidity profiling in the troposphere with a Raman lidar, *Appl. Opt.*, *41*, doi:http://dx.doi.org/10.1364/AO.41.006451.

Mattis, I., A. Ansmann, D. Müller, U. Wandinger, and D. Althausen (2004), Multiyear aerosol observations with dual-wavelength Raman lidar in the framework of EARLINET, *J. Geophys. Res.*, *109*, doi:10.1029/2004jd004600.

Mauger, G. S., and J. R. Norris (2007), Meteorological bias in satellite estimates of aerosol-cloud relationships, *Geophys. Res. Lett.*, *34*, doi:10.1029/2007GL029952.

McComiskey, A., and G. Feingold (2008), Quantifying error in the radiative forcing of the first aerosol indirect effect, *Geophys. Res. Lett.*, *35*, doi:10.1029/2007GL032667.

McComiskey, A., and G. Feingold (2012), The scale problem in quantifying aerosol indirect effects, *Atmos. Chem. Phys.*, *12*, doi:10.5194/acp-12-1031-2012.

McComiskey, A., G. Feingold, A. S. Frisch, D. D. Turner, M. A. Miller, J. C. Chiu, Q. Min, and J. A. Ogren (2009), An assessment of aerosol-cloud interactions in marine stratus clouds based on surface remote sensing, *J. Geophys. Res.*, *114*, doi:10.1029/2008JD011006.

McFarquhar, G., and A. Heymsfield (2001), Parameterizations of INDOEX microphysical measurements and calculations of cloud susceptibility: Applications for climate studies, *J. Geophys. Res.*, *106*, doi:10.1029/2000JD900777.

Metek GmbH (2013), Description of MIRA-36 cloud radar: http://metekgmbh.dyndns.org/mira36x.html.

Miles, N., J. Verlinde, and E. Clothiaux (2000), Cloud droplet size distributions in low-level stratiform clouds, *J. Atmos. Sci.*, *57*, 295–311.

Montopoli, M., and F. S. Marzano (2010), Meteorological radar systems, in *Integrated ground-based observing systems*, edited by D. Cimini, F. S. Marzano, and G. Visconti, pp. 33–57, Springer, Berlin/Heidelberg.

Müller, D., A. Kolgotin, I. Mattis, A. Petzold, and A. Stohl (2011), Vertical profiles of microphysical particle properties derived from inversion with two-dimensional regularization of multiwavelength Raman lidar data: Experiment, *Appl. Opt.*, *50*, doi: 10.1364/AO.50.002069.

Müller, D., U. Wandinger, and A. Ansmann (1999a), Microphysical particle parameters from extinction and backscatter lidar data by inversion with regularization: Simulation, *Appl. Opt.*, *38*, doi:10.1364/AO.38.002358.

Müller, D., U. Wandinger, and A. Ansmann (1999b), Microphysical particle parameters from extinction and backscatter lidar data by inversion with regularization: Theory, *Appl. Opt.*, *38*, doi:10.1364/AO.38.002346.

Müller, D., A. Ansmann, I. Mattis, M. Tesche, U. Wandinger, D. Althausen, and G. Pisani (2007), Aerosol-type-dependent lidar ratios observed with Raman lidar, *J. Geophys. Res.*, *112*, doi:10.1029/2006JD008292.

Murayama, T., N. Sugimoto, I. Uno, K. Kinoshita, K. Aoki, N. Hagiwara, Z. Liu, I. Matsui, T. Sakai, T. Shibata, K. Arao, B. Sohn, J. Won, S. Yoon, T. Li, J. Zhou, H. Hu, M. Abo, K. Iokibe, R. Koga, and Y. Iwasaka (2001), Ground-based network observation of Asian dust events of April 1998 in east Asia, *J. Geophys. Res.*, *106*, doi:10.1029/2000JD900554.

Nakajima, T., A. Higurashi, K. Kawamoto, and J. Penner (2001), A possible correlation between satellite-derived cloud and aerosol microphysical parameters, *Geophys. Res. Lett.*, *28*, doi:10.1029/2000GL012186.

O'Dowd, C., J. Lowe, M. Smith, and A. Kaye (1999), The relative importance of non-sea-salt sulphate and sea-salt aerosol to the marine cloud condensation nuclei population: An improved multi-component aerosol-cloud droplet parametrization, *Q. J. Roy. Meteorol. Soc.*, *125*, doi:10.1256/smsqj.55609.

Oreopoulos, L., and S. Platnick (2008), Radiative susceptibility of cloudy atmospheres to droplet number perturbations: 2. Global analysis from MODIS, *J. Geophys. Res.*, *113*, doi:10.1029/2007JD009655.

Painemal, D., and P. Zuidema (2013), The first aerosol indirect effect quantified through airborne remote sensing during VOCALS-REx, *Atmos. Chem. Phys.*, *13*, doi:10.5194/acp-13-917-2013.

Pal, S. R., and A. I. Carswell (1973), Polarization properties of lidar backscattering from clouds, *Appl. Opt.*, *12*, doi:10.1364/AO.12.001530.

Pal, S. R., and A. I. Carswell (1976), Multiple scattering in atmospheric clouds: Lidar observations, *Appl. Opt.*, *15*, doi:http://dx.doi.org/10.1364/AO.15.001990.

Pappalardo, G., A. Amodeo, M. Pandolfi, U. Wandinger, A. Ansmann, J. Bösenberg, V. Matthias, V. Amirdis, F. De Tomasi, M. Frioud, M. Iarlori, L. Komguem, A. Papayannis, F. Rocadenbosch, and X. Wang (2004), Aerosol lidar intercomparison in the framework of the EARLINET project. 3. Raman lidar algorithm for aerosol extinction, backscatter, and lidar ratio, *Appl. Opt.*, *43*, doi:10.1364/AO.43.005370.

Pappalardo, G., J. Bösenberg, A. Amodeo, A. Ansmann, A. Apituley, L. Alados Arboledas, D. Balis, C. Böckmann, A. Chaikovsky, A. Comeron, G. D'Amico, V. Freudenthaler, I. Grigorov, G. Hansen, H. Linné, S. Kinne, I. Mattis, L. Mona, D. Mueller, V. Mitev, D. Nicolae, A. Papayannis, M. R. Perrone, A. Pietruczuk, M. Pujadas, J.-P. Putaud, F. Ravetta, V. Rizi, V. Simeonov, N. Spinelli, T. Trickl, U. Wandinger, and M. Wiegner (2009), EARLINET: The European Aerosol Research Lidar Network for the Aerosol Climatology on Continental Scale, in *Current Problems in Atmospheric Radiation (IRS 2008): Proceedings of the International Radiation Symposium*, *AIP Conference Proceedings*, vol. 1100, edited by Nakajima, T. and Yamasoe, M. A., pp. 189–192, International Radiation Symposium (IRC/IAMAS), Foz do Iguacu, BRAZIL, AUG 03-08, 2008.

Partanen, A.-I., H. Kokkola, S. Romakkaniemi, V.-M. Kerminen, K. E. J. Lehtinen, T. Bergman, A. Arola, and H. Korhonen (2012), Direct and indirect effects of sea spray geoengineering and the role of injected particle size, *J. Geophys. Res.*, *117*, doi: 10.1029/2011JD016428.

Petty, G. W. (2006), *A first course in atmospheric radiation*, Sundog Publishing, Madison, Wisconsin.

Pincus, R., and M. B. Baker (1994), Effect of precipitation on the albedo susceptibility of clouds in the marine boundary-layer, *Nature*, *372*, doi:10.1038/372250a0.

Platnick, S., and L. Oreopoulos (2008), Radiative susceptibility of cloudy atmospheres to droplet number perturbations: 1. Theoretical analysis and examples from MODIS, *J. Geophys. Res.*, *113*, doi:10.1029/2007JD009654.

Platnick, S., and S. Twomey (1994), Determining the susceptibility of cloud albedo to changes in droplet consentration with the advanced very high-resolution radiometer, *J. Appl. Meteorol.*, *33*, doi:10.1175/1520-0450(1994)033⟨0334:DTSOCA⟩2.0.CO;2.

Quaas, J., O. Boucher, N. Bellouin, and S. Kinne (2008), Satellite-based estimate of the direct and indirect aerosol climate forcing, *J. Geophys. Res.*, *113*, doi:10.1029/2007JD008962.

Quaas, J., O. Boucher, and F. Breon (2004), Aerosol indirect effects in POLDER satellite data and the Laboratoire de Meteorologie Dynamique-Zoom (LMDZ) general circulation model, *J. Geophys. Res*, *109*, doi:10.1029/2003JD004317.

Quaas, J., O. Boucher, and U. Lohmann (2006), Constraining the total aerosol indirect effect in the LMDZ and ECHAM4 GCMs using MODIS satellite data, *Atmos. Chem. Phys.*, *6*, doi:10.5194/acp-6-947-2006.

Radiometer Physics GmbH (2013), Description of RPGs microwave radiometers: http://www.radiometer-physics.de/rpg/html/Products_Radiometers.html.

Radke, L. F., J. A. Coakley, and M. D. King (1989), Direct and remote-sensing observations of the effects of ships on clouds, *Science*, *246*, doi:10.1126/science.246.4934.1146.

Raga, G., and P. Jonas (1993), On the link between cloud-top radiative properties and sub-cloud aerosol concentrations, *Q. J. Roy. Meteor. Soc.*, *119*, doi:10.1002/qj.49711951410.

Ramanathan, V., P. Crutzen, J. Kiehl, and D. Rosenfeld (2001), Atmosphere - Aerosols, climate, and the hydrological cycle, *Science*, *294*, doi:10.1126/science.1064034.

Randriamiarisoa, H., P. Chazette, P. Couvert, J. Sanak, and G. Mégie (2006), Relative humidity impact on aerosol parameters in a Paris suburban area, *Atmos. Chem. Phys.*, *6*, doi:10.5194/acp-6-1389-2006.

Reichardt, J., U. Wandinger, V. Klein, I. Mattis, B. Hilber, and R. Begbie (2012), RAMSES: The German Meteorological Service autonomous Raman lidar for water vapor, temperature, aerosol, and cloud measurements, *Appl. Opt.*, *51*, doi:http://dx.doi.org/10.1364/AO.51.008111.

Rose, T., S. Crewell, U. Löhnert, and C. Simmer (2005), A network suitable microwave radiometer for operational monitoring of the cloudy atmosphere, *Atmos. Res.*, *75*, doi:10.1016/j.atmosres.2004.12.005.

Roy, G., and X. Cao (2010), Inversion of water cloud lidar signals based on accumulated depolarization ratio, *Appl. Opt.*, *49*, doi:10.1364/AO.49.001630.

Roy, G., L. Bissonnette, C. Bastille, and G. Vallée (1999), Retrieval of droplet-size density distribution from multiple-field-of-view cross-polarized lidar signals: Theory and experimental validation, *Appl. Opt.*, *38*, doi:10.1364/AO.38.005202.

Sasano, Y., E. V. Browell, and S. Ismail (1985), Error caused by using a constant extinction backscattering ratio in the lidar solution, *Appl. Opt.*, *24*, doi:http://dx.doi.org/10.1364/AO.24.003929.

Sassen, K., and R. L. Petrilla (1986), Lidar depolarization from multiple scattering in marine stratus clouds, *Appl. Opt.*, *25*, doi:10.1364/AO.25.001450.

Schmidt, J. (2009), Aufbau und Test von Mehrfachstreukanälen zur Messung der Wolkentröpfchengröße mit einem Ramanlidar, Master's thesis, Friedrich Schiller University Jena.

Schmidt, J., A. Ansmann, J. Bühl, H. Baars, U. Wandinger, and A. Malinka (2014), Dual-field-of-view Raman lidar measurements of aerosol-cloud-dynamics interaction: Case studies, submitted to J. Geophys. Res.

Schmidt, J., U. Wandinger, and A. Malinka (2013), Dual-field-of-view Raman lidar measurments for the retrieval of cloud microphysical properties, *Appl. Opt*, *52*, doi:http://dx.doi.org/10.1364/AO.52.002235.

Schwartz, S. E., Harshvardhan, and C. M. Benkovitz (2002), Influence of anthropogenic aerosol on cloud optical depth and albedo shown by satellite measurements and chemical transport modeling, *Proceedings of the National Academy of Sciences of the United States of America*, *99*, doi:10.1073/pnas.261712099.

Seifert, P., R. Engelmann, U. Wandinger, A. Ansmann, D. Althausen, B. Heese, J. Bühl, J. Schmidt, and A. Macke (2012), LACROS - Leipzig Aerosol and Cloud Remote Observations System, in *Proceedings of 16th International Conference on Clouds and Precipitation (ICCP)*, Leipzig, Germany, 30 July-3 August 2012.

Seifert, P., A. Ansmann, D. Müller, U. Wandinger, D. Althausen, A. J. Heymsfield, S. T. Massie, and C. Schmitt (2007), Cirrus optical properties observed with lidar, radiosonde, and satellite over the tropical Indian Ocean during the aerosol-polluted northeast and clean maritime southwest monsoon, *J. Geophys. Res.*, *112*, doi:10.1029/2006JD008352.

Sekiguchi, M., T. Nakajima, K. Suzuki, K. Kawamoto, A. Higurashi, D. Rosenfeld, I. Sano, and S. Mukai (2003), A study of the direct and indirect effects of aerosols using global satellite data sets of aerosol and cloud parameters, *J. Geophys. Res.*, *108*, doi:10.1029/2002JD003359.

Siebert, H., H. Franke, K. Lehmann, R. Maser, E. W. Saw, D. Schell, R. A. Shaw, and M. Wendisch (2006), Probing finescale dynamics and microphysics of clouds with helicopter-borne measurements, *Bull. Am. Meteorol. Soc.*, *87*, doi:10.1175/BAMS-87-12-1727.

Skupin, A. (2013), Optische und mikrophysikalische Charakterisierung von urbanem Aerosol bei (hoher) Umgebungsfeuchte, Dissertation, Universität Leipzig.

Stevens, B., W. R. Cotton, G. Feingold, and C. H. Moeng (1998), Large-eddy simulations of strongly precipitating, shallow, stratocumulus-topped boundary layers, *J. Atmos. Sci.*, *55*, doi:10.1175/1520-0469(1998)055⟨3616:LESOSP⟩2.0.CO;2.

Storelvmo, T., J. E. Kristjansson, H. Muri, M. Pfeffer, D. Barahona, and A. Nenes (2013), Cirrus cloud seeding has potential to cool climate, *Geophys. Res. Lett.*, *40*, doi:10.1029/2012GL054201.

Terai, C. R., R. Wood, D. C. Leon, and P. Zuidema (2012), Does precipitation susceptibility vary with increasing cloud thickness in marine stratocumulus?, *Atmos. Chem. Phys.*, *12*, doi:10.5194/acp-12-4567-2012.

TROPOS - LACROS (2013), Quicklook archive of performed dual-FOV Raman lidar measurements in Leipzig, Germany, http://polly.tropos.de/martha/quicklook-ms.php.

Twohy, C., M. Petters, J. Snider, B. Stevens, W. Tahnk, M. Wetzel, L. Russell, and F. Burnet (2005), Evaluation of the aerosol indirect effect in marine stratocumulus clouds: Droplet

number, size, liquid water path, and radiative impact, *J. Geophys. Res.*, *110*, doi:10.1029/2004JD005116.

Twohy, C. H., J. R. Anderson, D. W. Toohey, M. Andrejczuk, A. Adams, M. Lytle, R. C. George, R. Wood, P. Saide, S. Spak, P. Zuidema, and D. Leon (2013), Impacts of aerosol particles on the microphysical and radiative properties of stratocumulus clouds over the southeast Pacific Ocean, *Atmos. Chem. Phys.*, *13*, doi:10.5194/acp-13-2541-2013.

Twomey, S. (1974), Pollution and the planetary albedo, *Atmos. Environ.*, *8*, doi:http://dx.doi.org/10.1016/0004-6981(74)90004-3.

Twomey, S. (1977), Influence of pollution on shortwave albedo of clouds, *J. Atmos. Sci.*, *34*, doi:http://dx.doi.org/10.1175/1520-0469(1977)034⟨1149:TIOPOT⟩2.0.CO;2.

Veselovskii, I., M. Korenskii, V. Griaznov, D. N. Whiteman, M. McGill, G. Roy, and L. Bissonnette (2006), Information content of data measured with a multiple-field-of-view lidar, *Appl. Opt.*, *45*, doi:http://dx.doi.org/10.1364/AO.45.006839.

Veselovskii, I., A. Kolgotin, V. Griaznov, D. Müller, K. Franke, and D. N. Whiteman (2004), Inversion of multiwavelength Raman lidar data for retrieval of bimodal aerosol size distribution, *Appl. Opt.*, *43*, doi:10.1364/AO.43.001180.

Vidal, J. (2011), Geo-engineering: Green versus greed in the race to cool the planet, The Observer (10 July), available from: http://www.guardian.co.uk/environment/2011/jul/10/geo-engineering-weather-manipulation.

Wandinger, U. (1994), Theoretische und experimentelle Studien zur Messung stratosphärischen Aerosols sowie zum Einfluss der Mehrfachstreuung auf Wolkenmessungen mit einem Polarisations-Raman-Lidar, Dissertation, Universität Hamburg.

Wandinger, U. (1998), Multiple-scattering influence on extinction- and backscatter-coefficient measurements with Raman and high-spectral-resolution lidars, *Appl. Opt.*, *37*, doi:http://dx.doi.org/10.1364/AO.37.000417.

Wandinger, U. (2005), Introduction to lidar, in *Lidar – Range-Resolved Optical Remote Sensing of the Atmosphere*, edited by C. Weitkamp, pp. 1–18, Springer, Berlin/Heidelberg.

Wandinger, U., and A. Ansmann (2002), Experimental determination of the lidar overlap profile with Raman lidar, *Appl. Opt.*, *41*, doi:http://dx.doi.org/10.1364/AO.41.000511.

Wandinger, U., I. Mattis, M. Tesche, A. Ansmann, J. Bösenberg, A. Chaikovski, V. Freudenthaler, L. Komguem, H. Linné, V. Matthias, J. Pelon, L. Sauvage, P. Sobolewski, G. Vaughan, and M. Wiegner (2004), Air mass modification over Europe: EARLINET aerosol observations from Wales to Belarus, *J. Geophys. Res.*, *109*, doi:10.1029/2004JD005142.

Welton, E. J., J. R. Campbell, J. D. Spinhirne, and V. S. Scott (2001), Global monitoring of clouds and aerosols using a network of micro-pulse lidar systems, in *Lidar remote sensing for industry and environment monitoring*, edited by Singh, U. N. and Itabe, T. and Sugimoto, N., Proceedings of the Society of Photo-Optical Instrumentation Engineers (SPIE), doi:10.1117/12.417040, Sendai, Japan, 9-12 October 2000.

Westwater, E., Y. Han, M. Shupe, and S. Matrosov (2001), Analysis of integrated cloud liquid and precipitable water vapor retrievals from microwave radiometers during the Surface Heat Budget of the Arctic Ocean project, *J. Geophys. Res.*, *106*, doi:10.1029/2000JD000055.

Wilson, R. N. (2001), *Reflecting Telescope Optics II*, Springer.

Xu, K.-M., and A. Cheng (2013), Evaluating low-cloud simulation from an upgraded multiscale modeling framework model. Part I: Sensitivity to spatial resolution and climatology, *J. Climate*, *26*, doi:10.1175/JCLI-D-12-00200.1.

Xue, H. W., and G. Feingold (2006), Large-eddy simulations of trade wind cumuli: Investigation of aerosol indirect effects, *J. Atmos. Sci.*, *63*, doi:10.1175/JAS3706.1.

Zheng, X., B. Albrecht, H. H. Jonsson, D. Khelif, G. Feingold, P. Minnis, K. Ayers, P. Chuang, S. Donaher, D. Rossiter, V. Ghate, J. Ruiz-Plancarte, and S. Sun-Mack (2011), Observations of the boundary layer, cloud, and aerosol variability in the southeast Pacific near-coastal marine stratocumulus during VOCALS-REx, *Atmos. Chem. Phys.*, *11*, doi:10.5194/acp-11-9943-2011.

List of Abbreviations

ADNet	Asian Dust Network
AERONET	Aerosol Robotic Network
APNC	Aerosol Particle Number Concentration
CALIPSO	Cloud–Aerosol Lidar and Infrared Pathfinder Satellite Observations
CCN	Cloud Condensation Nuclei
CDNC	Cloud Droplet Number Concentration
CERES	Clouds and the Earth's Radiant Energy System
EARLINET	European Aerosol Research Lidar Network
GDAS	Global Data Assimilation System
FOV	Field of View
FWHM	Full Width at Half Maximum
HYSPLIT	Hybrid Single–Particle Lagrangian Integrated Trajectory model
IPCC	International Panel on Climate Change
LACROS	Leipzig Aerosol and Cloud Remote Observations System
LALINET	Latin-American Lidar Network
Laser	Light Amplification by Stimulated Emission of Radiation
Lidar	Light Detection and Ranging
LWC	Liquid Water Content
LWP	Liquid Water Path
MARTHA	Multiwaveength Atmospheric Raman lidar for Temperature, Humidity, and Aerosol profiling
MODIS	MODerate Resolution Imaging Spectroradiometer
MPLNET	Micro Pulse Lidar Network
MWR	Microwave Radiometer
NCEP	National Center for Environmental Prediction
PMT	Photomultiplier Tube
Radar	Radio Detection and Ranging
SAEMS	Spectral Aerosol Extinction Monitoring System
TROPOS	Leibniz Institute for Tropospheric Research
UTC	Universal Time Coordinated
VOCALS-REx	VAMOS Ocean-Cloud-Atmosphere-Land Study Regional Experimemt
WiLi	Wind Lidar

Acknowledgements

It would not have been possible to finish this dissertation without the support of several people. Here, I want to express my gratitude towards them for helping me to turn the last years into a good and successful time for me.

First of all, I would like to thank my supervisor Ulla Wandinger. She introduced the idea of dual-FOV Raman lidar measurements to me. Her suggestions and advices provided me a deeper understanding of the topic and guided me in the pursuit of this work. Finally, her proofreading made it possible for me to comply with English grammar rules and to find an appropriate form for this work.

I am also grateful for the proofreading of Albert Ansmann. Besides its benefits for this thesis itself, it helped me to acquiring a deeper understanding of the scientific matter. Furthermore, Albert's knowledge and broad understanding of atmospheric processes as well as his resolution to find his way through new fields of atmospheric science were not only important for the success of this work but also inspiring to me.

Besides Ulla and Albert, the whole lidar team gave me valuable support for the pursuit of this work. To name only some of them, Patric Seifert provided help with the software utilized for the lidar data analysis and also took part in the proofreading. Johannes Bühl shared with me the lot of numerous night time measurements and was always ready to run his lidar to support my measurements. Ronny Engelmann gave me advice and support for several hardware issues and upgrades of "my" lidar, in which also Andre Klepel and Dirk Wölbing were involved. Dirk also supported this project with a number of night time measurements. Holger Baars helped with a couple of aerosol inversions. I will not forget Thomas Kanitz who was my roomate at several conferences and workshops, which made them more enjoyable.

Also other members of the TROPOS supported this work. Particularly Florian Ditas is to be mentioned here, because the interesting discussions with him were important for my understanding of cloud processes and helped me with the interpretation of the measured data. Discussions with Martin Simmel were very helpful as well.

The exchange of knowledge with Aleksey Malinka helped me not only due to his profound mathematical and analytical background but also because I appreciate his methods of approach and the corresponding perspectives on scientific questions.

For the success of such an ambitios project a pleasant and caring social environment is probably most important. I am very thankful for the numerous encounters with people who became meaningful to me. Particularly people who shared with me many years but also

those who spent only a couple of moments with me helped me to recover and grow, provided new strength and inspiration, remembered me of all the other magnificient apsects of life, widendend my horizons, and thus enabled me to pursue my dissertation and not getting knocked out by it.